Numerical and experimental study of a packed bed plasma reactor for environmental applications

Proefschrift voorgelegd tot het behalen van de graad van doctor in
de wetenschappen aan de Universiteit Antwerpen te verdedigen door

Koen Van Laer

Promotor
Prof. Dr. Annemie Bogaerts

Faculteit Wetenschappen
Departement Chemie
Antwerpen 2017

Universiteit
Antwerpen

Universiteit Antwerpen
Faculteit Wetenschappen
Departement Chemie

Numerical and experimental study of a packed bed plasma reactor for environmental applications

Proefschrift voorgelegd tot het behalen
van de graad van doctor in de wetenschappen
aan de Universiteit Antwerpen
te verdedigen door

Koen Van Laer

Promotor: Prof. Dr. Annemie Bogaerts

Antwerpen, 2017

Table of Contents

Acknowledgements

After years of blood sweat and tears, but to be honest mostly sweat, I managed to deliver the piece of work in your hands, my PhD thesis. But, as with all big projects, I couldn't have done it without the help of quite a few people.

First of all, my biggest gratitude goes out to my promotor Annemie Bogaerts. From day one she was ready to help me with any difficulties I came across during the five year period I was under her supervision. We had countless discussions, endured countless meetings and exchanged countless emails. I must say, your enthusiasm and energy is unrivalled. Hats off to you!

Secondly, I must also thank Stanimir Kolev, who singlehandedly provided my work with a highly needed boost after the first two years of difficulty. He was not only helpful during his time in our research group, but even when he was back in Bulgaria, I could always count on his expertise. Simply put: when in trouble, ask Stan!

Next on the list is Luc Van't dack. When it comes to computers, printers or workstations, Luc is the man for the job. He kept everything in good working condition, so I could do my job without having to worry about anything technical. And next to that, he is also just a very pleasant man to talk to.

During my time at Plasmant, I sat at one of four desks in office B2.31. Over the course of 5 years, I saw a lot of people come and go. However, there was always one constant, the presence (ahum!) of my colleague Stefan Tinck. Always in for a laugh or a funny comment, and from time to time even a serious conversation, you provided sunshine to our office, Stefan, kudos to you.

The rest of the Plasmant crew gets a big thank you too, for the interesting conversations in the hallway, the company at conferences abroad, the nice atmosphere at our workplace. Every one of you has a hand in that, so thank you.

Next to these work related thank you notes, I would also like to make use of this opportunity to thank a few of my closest friends and family.

First of all, I would like to thank my parents. You guys, always let me choose my own path. You provided me with the necessary guidance and support, but never forced me in any direction. Thank you for giving me this freedom.

Next up are my sisters, Jo and Sanne. Be-it our ‘business lunches’, visits at home or nights on the town, you’ve been my best friends my whole life. Thanks again, mam and dad, for filling my life with these two aces.

Most of you will know that at weeknights and during the weekends, I tend to have a very busy life. Reasons for this are the numerous friendships I have built up over the years from being a member of Chiro, SPW, Imitato, Moules Parquées, Platten Tuub, … or just from going for a drink in the weekend. I cherish all these friendships enormously, and would like to thank you all for the welcome distractions you provide.

And finally I would like to thank my girlfriend, Valerie, for being the source of constant joy in my everyday life.

Thank you all!

Koen

Chapter 1

Introduction

1.1 Climate Change

Backed by 97% of the scientific community with a climate expertise, climate change is happening, and is caused by human activity.[1] It can be defined as the long-term change in the Earth's overall temperature with massive and permanent ramifications, which include surging oceans, stronger storms, extreme heat and crippling drought. These conditions will have a devastating influence on our planet and its inhabitants. Therefore we must act now, to mitigate the foreseen devastation and turn around this otherwise inevitable evolution.

1.1.1 A Numbers Game

Throughout its long history, Earth has warmed and cooled time and again. Due to subtle shifts in its orbit, changes in the atmosphere or surface and varying energy release by the Sun, the climate on planet Earth changed. But in the last century another force has started to change the Earth's climate: human activity. Over the last 100 years, the world's combined land and ocean surface temperature has increased around 1°C.[2] Global temperature is bound to fluctuate over time. However, when looking at the average temperature per decade (figure 1-1(left)) it is clear that in the last thirty years the Earth got significantly warmer. The cause for this is found in the increased greenhouse gas (GHG) levels. After the 1950s the average amount of GHGs in the atmosphere took a strong leap forward (figure 1-1(right)) due to human activity. Both economic growth and growth in population are responsible. However, while the contribution of the increasing world population stays steady between years, the contribution of the growing economy rose.[3] The levels of greenhouse gases in the atmosphere are now higher than they ever were in at least the last three million years.[4] Besides, it is not only the historic height of the GHG levels that is disturbing, but even more so the speed at which the levels are rising. Yes, there have been times in the past (millions of years ago) that, for instance, the CO_2 level has been higher, as well as times when the global temperature has been higher, but there has never been a time that both of them increased this quickly. A difference of 1°C over a 100 years may not seem like a lot, but the influence on the environment is not to be underestimated. If human activity is the cause, then human activity should also be the solution!

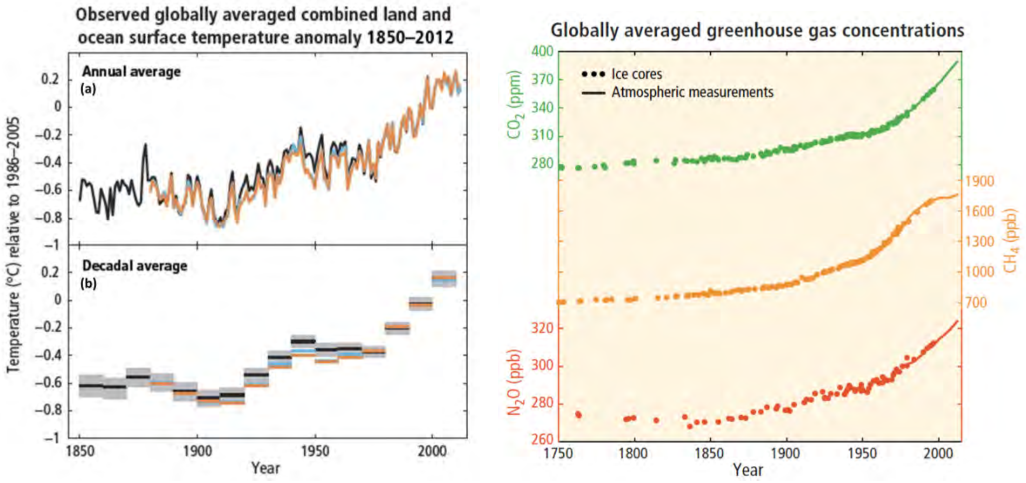

Figure 1-1 Globally averaged combined land and ocean surface temperature between 1850 and 2012 (left) and globally averaged greenhouse gas concentrations between 1750 and 2012 (right). Adopted from [2].

1.1.2 The Greenhouse Effect

Greenhouse gases are gases that can trap heat in the atmosphere, hereby causing global warming. Without this greenhouse effect, the Earth's average temperature would be a very chilly –18°C. However, with too much of them, the surface would be blazing hot, more comparable to the temperature of Venus, which is around 462°C due to its very dense solar trapping atmosphere.

The Sun constantly bombards the Earth with enormous amounts of radiation. The distribution of the emitted radiation in the wave spectrum is a function of the temperature of the emitter. Since the

Sun’s surface temperature is around 6000 K, its peak radiation is situated in the visible and near-visible part of the spectrum. About 43% is visible light. 7 to 8% is ultra violet light, which is more energetic due to its shorter wavelength. The remaining 49 – 50% is spread over the wavelengths longer than those of visible light in the near and far infrared region. About 30% of the incident radiation is immediately reflected back into space by bright surfaces such as clouds, snow, ice and sand.[5] The remaining 70% is absorbed by the land, the oceans and the atmosphere. To maintain radiative balance, the Earth also emits radiation. However, since the Earth’s base temperature, deducted from a perfect emitter (blackbody) with the same size and distance from the Sun, is 255K (-18°C), it emits radiation mainly in the long-wave (infrared) region.[6] Greenhouse gases are relatively inefficient in absorbing solar radiation, letting a lot of it pass through from space to Earth. The long-wave radiation emitted from Earth’s surface, on the other hand, is at an ideal energy level for them to absorb and reradiate in all directions, through a course of excitation and relaxation. A part of this radiation is directed back towards the surface, increasing its temperature, and thus causing global warming.

There are five major greenhouse gas categories, namely water vapour (H_2O), carbon dioxide (CO_2), methane (CH_4), nitrous oxide (N_2O) and fluorinated gases. The contribution of these gases to the greenhouse effect depends on the wavelength at which they absorb radiation, the concentration of the gas, the strength of absorption per molecule together with its lifetime in the atmosphere, and whether or not other gases absorb strongly at the same wavelengths. The two most abundant molecules in the atmosphere, nitrogen (N_2) and oxygen (O_2), are diatomic symmetric gases without a permanent dipole moment, which means that they are limited to electronic state transitions, which involve higher energies, and thus shorter wavelengths. Triatomic molecules like H_2O and CO_2 on the other hand can undergo smaller vibrational and rotational energy transitions, corresponding to the infrared wavelengths exerted by Earth's surface. Both water vapour and CO_2 absorb long-wave radiation over a range of frequencies. Because of their relatively high concentration, complete absorption (saturation) occurs at many of their spectral lines. The contribution of other gases absorbing at similar spectral lines will be limited, unless they have comparable concentrations. However, there is a region in the spectrum where absorption by H_2O and CO_2 is weak, known as the "atmospheric window". The previously mentioned gases, CH_4, N_2O and fluorinated gases ($CFCl_3$ and CF_2Cl_2 in particular), have strong absorption lines in or near this region and therefore also significantly contribute to the greenhouse effect, despite their lower concentrations.[6]

Water vapour is Earth's largest contributor to the greenhouse effect. It accounts for about 60% of the warming effect. However, water vapour does not control the Earth's temperature, but is instead controlled by it. The temperature of the surrounding atmosphere limits the maximum amount of water vapour it can contain. If the temperature changes, the water vapour can either condense to form liquid water, or the surrounding liquid water can evaporate and increase the level of water vapour.[7] The contribution of water vapour to the greenhouse effect will, however, at this stage always balance out.

The greenhouse effect that has kept the Earth's temperature at a level where life as we know it had the ability to thrive, is controlled by non-condensable gases of which carbon dioxide (CO_2) is by far the strongest contributor (figure 1-2). Since the beginning of the industrial revolution, the concentration of CO_2 in the atmosphere has gone up from 280 ppm to 406 ppm, almost entirely attributed to the continuously increasing usage of fossil resources by human activity.[8] Although CO_2 is of great importance in the ecosystem, being a carbon feedstock for plants through photosynthesis, the 40% increase over the last few 100 years will have devastating effects on the environment. Because CO_2 has the ability to stay in the atmosphere for hundreds of years, it will take centuries to reverse the current build-up.

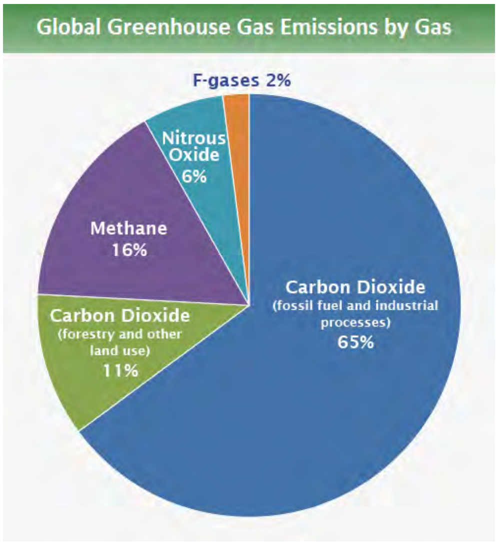

Figure 1-2 Contribution of the different greenhouse gases to the global number of GHG emissions in the year 2010. Adopted from [10]

To compare different GHGs with each other, the “Global Warming Potential” (GWP) is introduced. It indicates the amount of warming a gas causes over a given period of time (normally 100 years), compared to equal amounts of CO_2.[9] Table 1-1 gives an overview of the concentration in the atmosphere, average lifetime and GWP of the most important GHGs.

With a contribution of 16% to the total amount of GHG emissions, methane (CH_4) is the second most important GHG. Its concentration in the atmosphere is only a fraction of the concentration of CO_2, but its GWP is significantly higher. It is released in the atmosphere during the production and transport of coal, natural gas and oil, during agricultural practices and by livestock, and as a product of the decay of organic waste in landfills.[10]

Table 1-1 Overview of the atmospheric concentration, lifetime and GWP of the most important greenhouse gases.[11, 12]

	Concentration	**Lifetime**	**GWP** (100 years)
Carbon Dioxide	406 ppm	100 - 300 years	1
Methane	1834 ppb	12.4 years	28-36
Nitrous Oxide	328 ppb	121 years	265-298
Fluorinated gases	3 - 500 ppt	weeks - 1000s years	782 - 23500

Nitrous oxide (N_2O) accounts for about 6% of the global GHG emissions. N_2O is naturally present in the atmosphere as part of the nitrogen cycle and has a variety of natural sources. However, human activity such as agriculture, fossil fuel combustion, wastewater management and industrial processes have been increasing the atmospheric N_2O concentration since the industrial revolution. The concentration of N_2O in the atmosphere is only a thousand of the concentration of CO_2, but the impact of N_2O on warming the atmosphere is about 300 times the impact of an equal amount of CO_2.

Fluorinated gases have no natural sources and thus have only entered the atmosphere due to human activity. They are emitted through a variety of industrial processes such as aluminium and semiconductor manufacturing. The concentrations of fluorinated gases are rather low, but because many of these gases have very high GWPs and long lifetimes, these low concentrations can already have a significant impact on global warming. They are also known to deplete the stratospheric ozone layer.

1.1.3 Global Policy on Climate Change

In 1992, in the aftermath of the Rio Earth Summit, countries joined an international treaty, the "United Nations Framework Convention on Climate Change" (UNFCCC), as a framework for international cooperation to combat climate change by limiting average global temperature increases and coping with impacts that were, by then, inevitable.[13] The UNFCCC recognized that there was a problem already back in 1992, when there was less scientific evidence than there is now. However, they stated that member states should always act in the interest of human safety even in the face of scientific uncertainty. Nowadays the UNFCCC has almost global coverage with 197 participating countries. The ultimate objective of the Convention is to stabilize GHG concentrations at a level that would prevent "dangerous anthropogenic interference with the climate system". To define this interference the UNFCCC relies on the reports of the "Intergovernmental Panel on Climate Change" (IPCC). The IPCC is the leading international body for the assessment of climate change, with 195 member countries. Thousands of scientists all over the world contribute to the work of the IPCC. The fact that governments also participate in the review process, gives the produced reports a rigorous and balanced scientific nature, ideal to correctly inform decision makers worldwide.

With the Kyoto Protocol adopted in 1997, the UNFCCC booked its first big results towards the mitigation of GHG emissions. The Kyoto Protocol set emission limits for GHGs. Recognizing that developed countries are principally responsible for the current high levels of GHGs in the atmosphere, the protocol sets heavier targets on developed nations under the principle of "common but differentiated responsibilities". The first commitment period ran from 2008 – 2012 and set a combined goal to reduce the emissions of the developed countries by 5% of the levels of 1990. 37 countries and the European Community committed to this goal, but the United States of America was the biggest absentee. In the second commitment period, from 2013 – 2020, the goal is set to reduce the emissions further with 18% against 1990 levels. To reach their goal, countries can not only reduce their own emissions nationally, but can also make use of a few tools like "International Emissions Trading" (IET), "Clean Development

Mechanism" (CDM) and "Joint Implementation" (JI) to counter their national overproduction.

In 2015 another major milestone in the fight against climate change took place. At the Paris Climate Conference (COP21), 195 countries adopted the first-ever universal, legally binding global climate deal. The agreement sets out a global action plan to put the world on track to avoid dangerous climate change by limiting global warming to well below 2°C. The agreement forms a bridge between today's policies and the goal of climate-neutrality before the end of the century.

1.1.4 Changing the Energy Demand

To meet the goals of the Paris Agreement that will enter into force in 2020, global reliability on fossil fuels must be reduced. Since about two-thirds of the GHG emissions are linked to energy production, it is of great importance that governments, industry but also everyday people increase their investment in alternative energy sources such as wind, water and solar power. The International Energy Agency (IEA) made a projection in 2016 that, if all nations abide by the Paris Agreement, in 2040, 37% of power generation will come from renewables compared to 23% today. Furthermore, there will be 150 million electric cars instead of only 1.3 million. The demand for cleaner natural gas will grow with 50% overtaking coal in the global energy mix. The oil consumption will have increased to 103.5 million barrels per day, compared to 92.5 in 2015, and the carbon emissions in the energy sector will still grow annually with 0.5%. This leaves the energy sector CO_2 emissions not on track for a 2°C scenario. To achieve the 2°C target, the IAE states that by 2100 the energy sector should be carbon-neutral. The initial goals of the Paris Agreement cannot and may not be the definitive approach to tackle the problem. As stated in the Paris Agreement itself, the goals must be reviewed every 5 years and renewed to a higher ambition. Only this way we can keep temperature rise under 2°C.

Results of investment in renewable energies and energy efficiency as a whole have been creeping up in our everyday lives (in the EU). Domestic energy providers now offer formulas where one can power his home with 100% renewable energy. More and more solar panels have found their way onto our roofs. Home isolation has been a hot topic at every building exhibition. More and more electric cars are seen on the road. Electricity generating windmills are no longer uncommon in our daily view. This is a promising evolution. However, not all is well. It is dreadful to see that in this day and age a huge global playmaker like the United States still hands out the necessary permits for the build of a pipeline that ensures the use of the very polluting and inefficient oil sands in Canada as source of fossil fuels for the coming decades. Instead of going for the easiest but most harmful approach, they should be investing and innovating like so many others. A big problem in the USA is the belief in the involvement of mankind. Although the scientific community is clear about climate change, there are still people, even in powerful governing positions, who do not believe man-made climate change is real. It is therefore of key importance to keep spreading the knowledge, to inform people about the significance of climate change, and the dire need for action!

1.2 Gaseous Pollutants

Besides the release of greenhouse gases with their long-term impact on the environment, human activity also releases other hazardous chemicals into the atmosphere: acid gases such as NO_2 and SO_2 which, when brought in contact with water vapour, form acid rain, toxic gases such as mercury and a group of volatile organic compounds, which can have all these attributes and more.

1.2.1 Volatile Organic Compounds

Along with carbon, VOCs contain elements such as hydrogen, oxygen, fluorine, chlorine, bromine, sulphur or nitrogen.[14] Emissions of VOCs originate from burning fuels such as gasoline, wood, coal or natural gas. In the industry VOCs can also be emitted from breathing and loading losses from storage tanks, venting of process vessels and leaks from piping and equipment, wastewater streams and heat exchange systems.[15] Release on a more domestic level is also possible since VOCs are also found in solvents, paints and glues, of which the phenol formaldehyde resins in fibreboards are a clear example. Furthermore, the exhaust gas from diesel cars also contains a high level of VOCs.

There are great differences between the dangers of the different chemicals that classify as VOC. Some compounds like benzene and formaldehyde have a direct carcinogenic effect. The concentration is of course very important. Indoors, the VOC concentration can easily build up to a level that the VOC becomes a direct health hazard. Outdoors the compounds can disperse, lowering direct health risks. However, outdoors some VOCs can in combination with NOx and sunlight lead to the formation of photochemical smog, which is hazardous for human health but can also contribute to climate change. Because of these bad attributes, control of VOC emissions forms a major concern of the industries' commitment towards the environment.

Chapter 2

Plasma Technology for Environmental Applications

2.1 What is Plasma?

Plasma, also referred to as the fourth state of matter, is defined as an ionised gas, which means that it consists of charged species such as electrons and ions, as well as neutral atoms and molecules. Furthermore, plasma also contains radicals and excited particles. These last ones are the source of an important property of a plasma, namely that it can emit light. Al these species can collide and react with each other, making plasma a highly energetic but complex environment.

Plasmas can be divided into two broad categories: natural and man-made. More than 99% of visible matter in the universe is in the plasma state; this includes the Sun, most stars and a significant fraction of the interstellar medium.[16] In Earth's atmosphere, the low temperature and high pressures that are commonly present are not favourable for the formation of plasmas, except under unusual circumstances. The most common natural plasma phenomenon in our atmosphere is lightning. In a lightning discharge the atmospheric gas is ionised and heated to a very high temperature by the electrical currents that are present in the discharge. Because of the high recombination rate, the plasma only exists for a fraction of a second. The Aurora Borealis (near the north pole) and Australis (near the south pole) are also examples of natural plasmas occurring on planet Earth. An aurora is caused by the striking of energetic electrons and ions from the Sun into our atmosphere, 80 to 100 km above the Earth's surface.

Man-made plasmas can be divided into the high-temperature plasmas or fusion plasmas, and low temperature plasmas or gas discharges. Fusion plasmas are known from the nuclear fusion reactor, which is being heavily investigated as future alternative energy source. Gas discharges can either be thermal or non-thermal. The difference lies in the temperature of the neutral gas particles. In a thermal plasma all particles carry the same high temperature, i.e. they are in thermal equilibrium, while in a non-thermal plasma only the charged particles, and especially the electrons due to their small mass, are at elevated temperature, much higher than the temperature carried by the neutral particles. In this thesis we will focus on non-thermal plasma sources.

To initiate a plasma, energy must be added externally to a gas or gas mixture. Often this is done by applying a potential difference between two electrodes. However, there are also other ways to add energy to the system, for instance with microwaves. In the following section the different types of non-thermal plasmas most commonly used in research for environmental applications are discussed.

2.2 Types of Plasmas used mainly for Environmental Applications

2.1.1 Dielectric Barrier Discharge

The dielectric barrier discharge (DBD) was first introduced in 1857 by Werner Von Siemens for experimental research on the generation of ozone.[17] The typical attribute of a DBD reactor is that at least one of its electrodes is covered with a dielectric material. The presence of this dielectric material has two consequences. The first is that the reactor can be operated at elevated pressures, for instance atmospheric pressure, without arcing. Second, the reactor must be applied with an alternating potential, to keep the discharge alive. Indeed, the dielectric, being an insulator, cannot pass a dc current. Typical electrode configurations are illustrated in figure 2-1, with planar versus cylindrical being the biggest difference. This last reactor is ideal for industrial upscaling as demonstrated in commercially used ozone generators.[18]

Depending on the gas and operating parameters, the discharge characteristics inside a DBD reactor can change quite a bit.[19] For most gases the discharge will be filamentary. A large number of individual tiny breakdown channels, referred to as microdischarges, take place over the gap between the electrodes. At a dielectric surface the microdischarge channels spread into surface discharges covering a much larger region than the original channel diameter. The individual filaments can be characterised as weakly ionized plasmas with properties resembling those of transient high pressure glow discharges. They start when the breakdown field is reached locally and disappear when the field is reduced to such an extent that electron attachment and recombination dominate over ionization. Charges build up on the dielectric surfaces, causing the field at the location of the breakdown to collapse within a few ns, which terminates the current flow at this location. As long as the external voltage is rising, additional microdischarges are initiated at new locations because the presence of residual charges has lowered the electric field at positions where a microdischarge already took place.

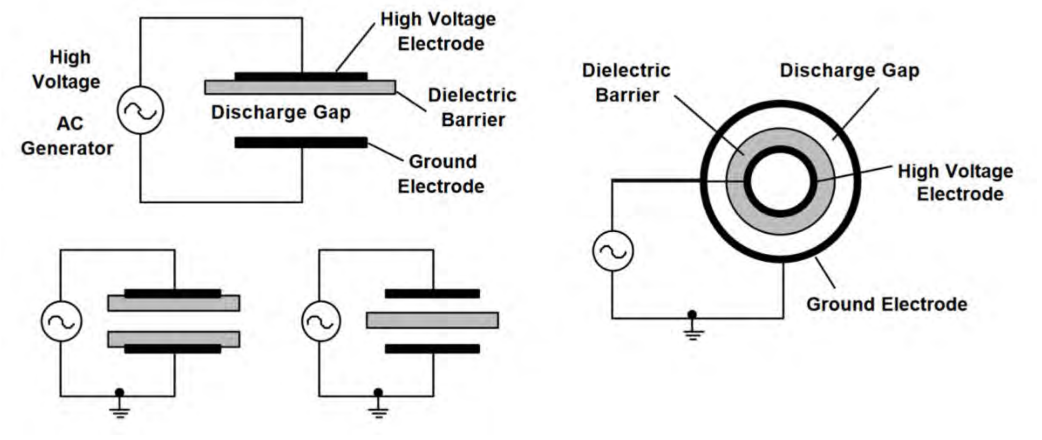

Figure 2-1 Common dielectric barrier discharge electrode configurations. Adopted from [18].

Second, homogeneous diffuse discharges can also be obtained in a DBD reactor.[20-22] Instead of a lot of small current peaks per half cycle of applied potential, only one (or a few) current peaks take place. The fact whether a homogeneous discharge can be created depends on the applied potential, the frequency, the distance between the electrodes, the type and thickness of the dielectric layer(s), the operating pressure and the discharge gas. Under atmospheric pressure, only a few gases such as helium, argon, nitrogen, and oxygen are able to reach this type of discharge. However, when the pressure is lowered, typically below 100 Pa, diffuse glow discharges can always be obtained. The dielectric layer can then even be removed because of the reduced risk of arcing. The resulting discharges are then referred to as RF glow discharges, with applications in the semiconductor industry. However, in this thesis we are focussing on atmospheric pressure DBD plasmas.

2.1.2 Gliding Arc Discharges

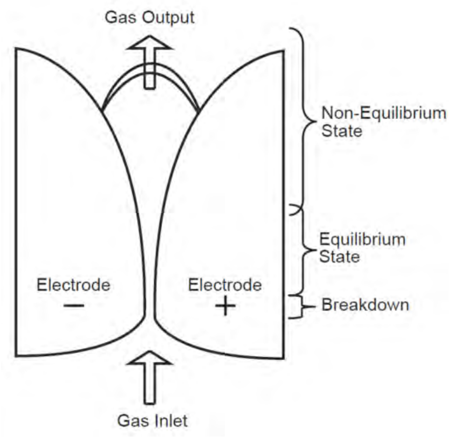

Figure 2-2 Schematic overview of the classical gliding arc discharge. Adopted from [23].

A classical gliding arc discharge, also called travelling or sliding arc discharge, is a non-stationary arc discharge between two diverging electrodes submerged in a gas flow (figure 2-2).[23] The arc initiates itself where the electrodes are closest together and is pushed by the gas flow towards the diverging electrode region. As a result, the arc length grows until the applied voltage becomes insufficient to sustain the extended arc, or until another arc is initiated at the shortest electrode distance.

The gliding arc can either be thermal or non-thermal depending on the input power and flow rate. It is also possible that the arc in the beginning is thermal, but during space-time evolution transitions into a non-thermal arc. In this case the discharge combines the benefits of both thermal equilibrium and non-thermal equilibrium discharges on the subject of dissipated power and efficiency.

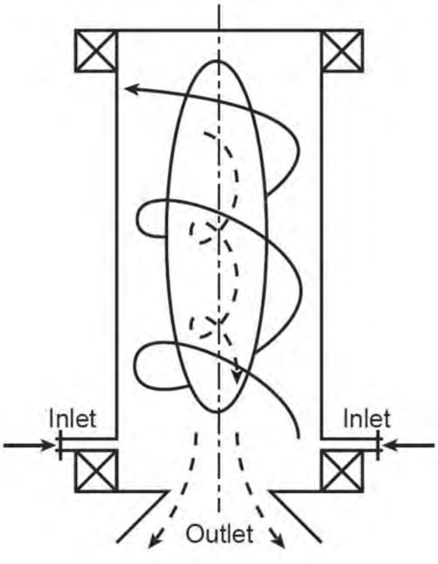

Figure 2-3 Scheme of the reverse-vortex flow gliding arc discharge. Adopted from [24].

A special configuration of a gliding arc discharge, namely the reverse-vortex flow configuration, has received a lot of attention for use in environmental applications (figure 2-3).[24] With vortex flow stabilization, the heat losses of the plasma are reduced which should boost the efficiency.[25] Furthermore, it also improves the electrode lifetime, the ionization efficiency and the gas conversion. In a reverse-vortex flow reactor, the flow is provided by a so called "swirl generator”. Usually it consists of four or more tangentially oriented inlets, which are placed at the same reactor end as the outlet. The tangentially applied gas stream initiates a vortex swirl flow around the edges of the reactor. After it hits the upper wall, a secondary inner vortex is formed within the outer flow, going the other way. The plasma is confined within the inner flow, providing nearly perfect heat insulation from the walls. The reverse-vortex flow also leads to better gas mixing with the active plasma arc, which further improves the gas conversion.

2.1.3 Microwave Discharge

In a microwave plasma reactor, the energy of centimetre range electromagnetic waves (i.e. microwaves) is transferred to the plasma. The electromagnetic energy can be coupled with the plasma in different ways. The most typical coupling is provided in waveguides, where a dielectric transparent tube for electromagnetic waves, usually quartz, crosses the rectangular waveguide. Plasma is ignited and maintained inside the dielectric tube (figure 2-4). To provide plasma stabilization, a gas flow can be tangentially supplied.[24] The dimensions of the waveguide are related to the microwave frequency. The reactor is built so that the plasma is ignited in the centre of the dielectric tube. When the reactor is operated at reduced pressures, the plasma has the ability to remain non-thermal, with electron temperatures around 1 eV. For environmental applications, especially the splitting of CO_2, this is ideal, because around this electron temperature the vibrational excitation of CO_2 is more pronounced. A higher pressure, say atmospheric pressure, usually leads to worse results. However, as atmospheric pressure is desirable for industrial implementation, research should be performed focussing on improving the results at this elevated pressure.

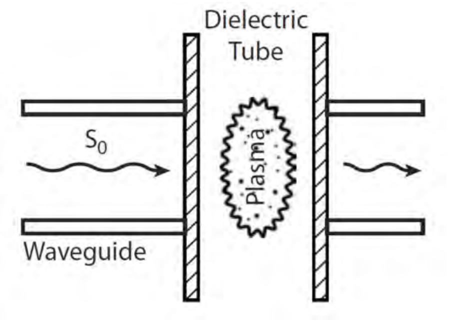

Figure 2-4 Schematic overview of a microwave reactor. Adopted from [24].

2.1.4 Packed Bed Plasma Reactor

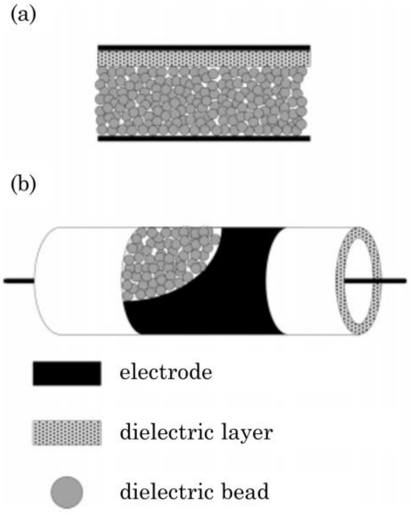

Figure 2-5 Schematic overview of a planar (a) and cylindrical (b) packed bed plasma reactor. Adopted from [26].

A packed bed discharge is a special form of dielectric barrier discharge, where the reactor is filled with a packing (figure 2-5). This packing can have any size or shape and can be made of any dielectric material. Most of the time, the beads are spherical. The idea behind introducing a packing in a DBD reactor is to enhance the electric field inside the reactor in order to increase the conversion rate and/or energy efficiency of the application at hand. Depending on the size, shape and dielectric constant of the material this enhancement can be as big as a factor 250.[26] Typical dielectric materials range from glass and quartz (ε ~ 5), alumina (ε ~ 9), zirconia (ε ~ 25), titania (ε ~ 100) to barium titanate (ε ~ 1000 – 20000). Barium titanate, as a ferroelectric material, shows a big range in dielectric constant. The exact value will depend on its crystal structure.

If the packing beads are made of or coated with a catalytically active material, the purpose changes to steering the plasma reactions towards a desired end product. This process is now called plasma catalysis.

2.3 Focus in this PhD Thesis

In this thesis the packed bed plasma reactor (PBPR) is thoroughly investigated. Using an experimental setup of a cylindrical DBD reactor packed with dielectric beads, the influence of bead size and operation parameters on the conversion and efficiency of the splitting of pure CO_2 is investigated. The biggest challenge in this thesis, however, was to understand the discharge characteristics of the plasma formed in a packed bed reactor. To tackle this, a computational investigation was performed using fluid modelling.

2.3.1 State of the Art

Experimentally, it has been demonstrated that the introduction of a packing in a DBD reactor can increase conversion rates and energy efficiencies of the application at hand. On the destruction of VOCs and methane reforming the number of available papers is plentiful.[27-37] However, on pure CO_2 splitting with a packed bed reactor, the amount of information is more limited. Yu et al. studied the decomposition of CO_2 in a packed bed DBD reactor using different packing materials, i.e., silica gel, quartz, α-Al_2O_3, γ-Al_2O_3 and

$CaTiO_3$.[38] The best results were found with a $CaTiO_3$ packing, boosting the conversion from 12.5% in an empty DBD reactor up to 20.5%. The energy efficiency at this stage was 4.8%, a factor 1.7 higher than without packing. Mei et al. obtained similar results, using glass beads and $BaTiO_3$ as packing materials at different input powers.[39] A 75% increase up to a maximum conversion of 28% was reached when introducing a packing of $BaTiO_3$ beads. In recent years, studies were performed to further increase the improved results of the PBPR. Butterworth et al. studied the influence of not only the bead material (Al_2O_3 and $BaTiO_3$) but also the bead size and gas composition (90/10 Ar/CO_2 to pure CO_2) on the splitting of CO_2.[40] Michielsen et al. also performed a study of bead size and bead material on the splitting of pure CO_2.[41] Lastly, Duan et al. investigated a microreactor with different bead sizes and bead materials.[42] The results of these studies did not always reveal the same trend. Butterworth et al. found best results with the smallest packing beads in case of the CO_2/Ar mixture. However, without the carrier gas, the benefits of smaller packing beads were drastically mitigated or even reversed. Michielsen et al. concluded that for pure CO_2 the largest beads with the highest dielectric constant performed the best. In the microreactor of Duan at al. the maximum conversion and efficiency was found with the smallest packing beads with highest dielectric constant. It is clear that there is no simple rule regarding the bead size that ensures the best results. Although a higher dielectric constant seems to be the best, the study of Michielsen et al. reveals that also other material parameters can play a role. Thus, more insight is clearly needed.

Compared to experimental conversion rates and efficiencies, which can easily be measured, the exact behaviour of the plasma in a packed bed reactor, such as its ignition and propagation through the packing material, is not well described yet. The presence of the packing in the reactor blocks the visual path for optical diagnostics. The fact that a packed bed reactor is much more defined by local effects is not helping either. A computational study can therefore be a very interesting approach to achieve a better understanding of the discharge behaviour, which can then help explain experimental observations and assist the experiments in further improving the performance.

The number of computational studies on a PBPR is again limited. Chang and Takaki et al. developed a simplified time averaged 1D numerical plasma model for N_2, based on solving Poisson's equation and transport equations.[43, 44] They found that all plasma parameters increase upon increasing applied potential and dielectric constant. Due to the 1D limitation, the void between the beads was simply assumed to be spherical. Kang et al. studied the first 20 ns of the propagation of the microdischarges formed in a 2D model of a DBD reactor with two stacked ferroelectric beads inside.[45] Russ et al. used a 2D fluid model to simulate the formation of microdischarges in a packed bed DBD reactor filled with dry exhaust gas (N_2/O_2 = 80/20 and 500 ppm NO).[46] The work was limited to a short one-directional discharge with a constant applied potential. Although not directly applied to a packed bed reactor, Babaeva et al. performed very relevant modelling work on the influence of dielectric spheres blocking a plasma streamer, using a 2D fluid model in humid air ($N_2/O_2/H_2O$ = 79.5/19.5/1).[47] More recently, Kruszelnicki et al. studied the propagation of negative electrical discharges in a PBPR with a combination of a 2D fluid model and a purpose-built experimental setup.[48] Surface ionization waves (SIWs) and positive restrikes were shown to be mainly responsible for reactive species production. Finally, Zhang et al. applied a 2D particle-in-cell / Monte Carlo collision (PIC/MCC) model to describe the filamentary discharge behaviour in a packed bed DBD reactor in air (N_2/O_2 = 80/20).[49]

2.3.2 Aim and Outline of the PhD Thesis

The aim of this PhD thesis is to get a better understanding of the plasma characteristics in a packed bed plasma reactor, in order to help explain the improved experimental results of a packed reactor versus a non-packed reactor in the context of CO_2 splitting. To get a better understanding of the experimental work, we performed experiments with an in-house cylindrical DBD reactor.[50] Based on the experimental reactor we built a simplified model to study the plasma behaviour in a PBPR. This model could then be adjusted to investigate the influence of bead size, dielectric constant and reactor size. A further modification lets us investigate the propagation of the plasma through the packing in more detail.

In the first part of **chapter 3** the experimental setup and used diagnostics are described. The second part describes the equations solved in the model, and the time-dependent solver used to generate the results.

In **chapter 4** the experimental results are reported and benchmarked against the best available results in literature.

C**hapter 5** describes the modelling approach, and how we had to think outside the box to build the best approximation to the real life reactor geometry. It also contains the description of the boundary conditions and used plasma chemistry.

In **Chapter 6** the influence of the reactor size is investigated together with the dielectric constant of the packing beads.

In **Chapter 7** we study the role of the size of the packing beads together with their dielectric constant.

Finally in C**hapter 8** we aim to get a better understanding of the propagation of plasma through a packing, by modelling the evolution of a streamer hitting packing beads in nanosecond time scale.

Chapter 3

Experimental and Modelling Description

3.1 Experimental Setup

The focus of this thesis does not lie on the experiments. However, to get familiar with the experimental setup of a packed bed DBD reactor, and the accompanying experimental diagnostics, experiments were performed on the splitting of pure CO_2 with the in-house cylindrical DBD reactor, packed with zirconia beads with varying diameter. Also the influence of the input power and gas flow rate were investigated.

3.1.1 Apparatus

The cylindrical DBD reactor consists of an inner electrode and a coaxial Al_2O_3 tube (figure 3-1). The inner electrode is a stainless-steel rod with a diameter of 8.0 mm and is grounded. The Al_2O_3 tube has an inner and outer diameter of 17.0 and 22.0 mm, respectively, and is covered by a nickel foil electrode connected to an AC high-voltage power supply (AFS). It has a length of 90 mm, which defines the length of the discharge region. The discharge gap, that is, the distance between inner electrode and Al_2O_3 tube, is fixed at 4.5 mm, which results in a discharge volume of 15.9 cm^3. The CO_2 gas flow rate is controlled by using a mass flow controller (EL-flow, Bronkhorst). The total current is recorded by using a Rogowski-type current monitor (Pearson 4100), and a high-voltage probe (Tektronix P6015A) is used to measure the applied voltage. To obtain the charge generated in the discharge, the voltage on the external capacitor is measured. All the electrical signals are sampled by using a four-channel digital oscilloscope (Picotech PicoScope). To determine the CO_2 conversion and energy efficiency, the CO_2 gas is detected after plasma treatment with a three-channel compact gas chromatograph (CGC) (Interscience), equipped with two thermal conductivity detectors (TCD) and a flame ionization detector (FID). The first TCD channel contains a Molecular Sieve 5A column for the segregation of the molecular gases O_2, N_2 and CO, while the second TCD channel is equipped with an Rt-QBOND column for the measurement of CO_2 and C1-C2 hydrocarbons. The FID is equipped with an Rtx-5 column for the measurements of C1-C10 containing compounds. Benchmark measurements, without plasma treatment, are also performed to know the CO_2 signal at the inlet.

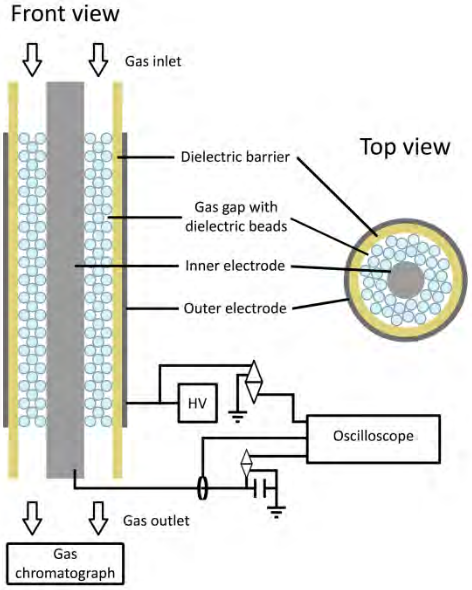

Figure 3-1 Schematic overview of the experimental setup.

3.1.2 Determination of CO_2 Conversion and Energy Efficiency

The CO_2 conversion X_{CO2} is calculated as:

$$X_{CO_2}(\%) = \frac{CO_{2,inlet} - CO_{2,outlet}}{CO_{2,inlet}} \times 100\%$$

In this formula the volume change when CO_2 is split into CO and O_2 is not taken into account. At 100% conversion, two CO_2 molecules are converted into three molecules, namely two CO and one O_2 molecule, effectively increasing the volume. Since the GC samples a constant volume at atmospheric pressure, it introduces a systematic overestimation. This issue was recently reported by Pinhão,[51] and is since then taken into account in the experiments performed within our group, but the results presented here were obtained before this time. Moreover, since the available literature on CO_2 splitting, to which we will compare our results, did not account for this expansion factor, we opted to not use it either.

In order to calculate the energy efficiency of the process, we first define the specific energy input (SEI) from the plasma power and the gas flow rate:

$$SEI\left(\frac{kJ}{L}\right) = \frac{P_{plasma}(kW)}{Flow\left(\frac{L}{min}\right)} * 60\left(\frac{s}{min}\right)$$

The plasma power itself is calculated from the instantaneous applied potential (V(t)) and the measured current (I(t)) over one period (T):

$$P_{plasma} = \frac{1}{T}\int_0^T V(t) * I(t)\ dt$$

And finally, the energy efficiency is defined as:

$$\eta(\%) = \frac{\Delta H_R\left(\frac{kJ}{mol}\right) * X_{CO_2}(\%)}{SEI\left(\frac{kJ}{L}\right) * molar\ volume\left(\frac{L}{mol}\right)}$$

The reaction enthalpy (ΔH_R) for CO_2 splitting equals 279.8 kJ mol^{-1} or 2.9 eV molec^{-1}.

3.2 Model description

3.2.1 Fluid Equations

Using COMSOL's built-in plasma module, a two-dimensional axisymmetric fluid model is developed with semi kinetic treatment of the electrons. The model is based on solving a set of coupled differential equations that express the conservation of mass, momentum and energy, for the different plasma species. The mass conservation equation is as follows:

$$\frac{\partial n_i}{\partial t} + \nabla \cdot \mathbf{\Gamma_{i,j}} = S_i$$

n_i stands for the density of the plasma species i, which can be an electron, ion, radical or neutral species. $\mathbf{\Gamma_{i,j}}$ is its flux, and S_i is the source term, which is the sum of the production and loss terms for this species, based on the chemical reaction set (see below):

$$S_i = \sum_r c_{i,r} R_{i,r}$$

$c_{i,r}$ is the stoichiometric coefficient of species i in reaction r, and $R_{i,r}$ the reaction rate. The conservation equation of momentum is not explicitly solved, but is replaced by an expression for the flux, based on the drift-diffusion approximation:

$$\mathbf{\Gamma_{i,j}} = \mu_{i,j} n_i \mathbf{E} - D_{i,j} \nabla n_i$$

The first term describes the electric drift, with $\mu_{i,j}$ the mobility and E the electric field, and will only be solved for the electrons and the ions. The second term stands for the diffusion, with D_i the diffusion coefficient. This term is solved for all species. The third conservation equation describes the electron energy:

$$\frac{\partial n_\varepsilon}{\partial t} + \nabla \cdot \mathbf{\Gamma}_{\boldsymbol{\varepsilon},\mathbf{j}} = S_\varepsilon$$

n_ε is the electron energy density (i.e., the product of electron density ne and mean electron energy ε), S_ε is the source term for the electron energy and $\Gamma_{\varepsilon,i}$ is the electron energy flux:

$$S_\varepsilon = -e\mathbf{\Gamma}_{\mathbf{e},\mathbf{j}} \cdot \mathbf{E} + \sum_r c_r \bar{\varepsilon}_r R_r$$

$$\mathbf{\Gamma}_{\boldsymbol{\varepsilon},\mathbf{j}} = \frac{5}{3}\mu_{e,j}\mathbf{E}n_\varepsilon - \frac{5}{3}D_{e,j}\nabla n_\varepsilon$$

The first term in the source term equation describes the Joule heating of the electrons by the electric field. The second term represents the change in electron energy due to chemical reactions, where $\varepsilon_{,r}$ is the energy lost or gained by one electron in reaction r. In the electron energy flux equation, $\mu_{e,j}$ and $D_{e,j}$ stand for the electron mobility and diffusion coefficient, respectively. From the electron energy and electron density, the electron temperature T_e can be calculated:

$$k_B T_e = \frac{2}{3}\bar{\varepsilon} = \frac{2}{3}\frac{n_\varepsilon}{n_e}$$

Finally, the Poisson equation will also be solved to self-consistently calculate the electric field distribution, using the densities of the different charged plasma species as input in the gas gap, and solving for zero space charge in the dielectric material:

$$\nabla \cdot (\varepsilon_0 \varepsilon_r \mathbf{E}) = -\nabla \cdot (\varepsilon_0 \varepsilon_r \nabla V) = \rho$$

ε_0 is the permittivity of vacuum, ε_r the relative permittivity of the material or the gas, V is the potential and ρ is the space charge density.

3.2.2 Solver Details

The time-dependent solver is an implicit differential-algebraic solver (IDA) and uses variable-step, variable-order backward differential formula (BDF) methods for its integration, with a maximum order of 2. At each step, the nonlinear system is linearized by a Newton iteration, into the $A \cdot x = b$ form. This linear system is then solved with PARDISO, which stands for parallel sparse direct solver.[52] It uses LU factorization on a matrix A to find the solution x. The time steps are chosen automatically by the BDF solver, based on the relative and absolute tolerances that control the solution error. For all variables we chose to set these errors at 0.001. On average, the time steps lie between 10^{-7} and 10^{-10} s. Further details on COMSOL Multiphysics can be found on their website.[53]

Chapter 4

Experimental Study of a ZrO_2 Packed Bed Plasma Reactor

This chapter is based on the publication: K. Van Laer and A. Bogaerts, "Improving the Conversion and Energy Efficiency of CO_2 splitting in a ZrO_2-packed DBD Reactor", *Energy Technology* **3** (2015) 1038-1044

4.1 Introduction

As mentioned in chapter 2, in the description of the state-of-the-art, it has been extensively demonstrated that the introduction of a packing can lead to higher conversions and energy efficiency for other applications, such as the destruction of VOCs.[27-37] However, on pure CO_2 splitting, the number of available papers are more limited, especially when it comes to mentioning the energy efficiency.[38-42]

In this chapter, we investigate the influence of introducing a packing in the DBD reactor on the conversion and energy efficiency of CO_2 splitting. By using a zirconia (ZrO_2) packing and varying the bead size, flow rate, and input power, we try to improve the best available results in literature, towards a higher conversion and energy efficiency.

4.2 Details on the Experimental Setup

Experiments are carried out for three different gas flow rates, i.e. 20, 50 and 100 mL min^{-1}, and three different applied powers, i.e. 60, 80 and 100 W, both with and without ZrO_2 packing, using the setup described in chapter 3. The experiments without packing serve as benchmark, to define the improvement in conversion and energy efficiency. The experiments with packing are performed with five different bead size ranges, i.e., diameters of 0.90-1.00, 1.00-1.18, 1.25-1.40, 1.60-1.80 and 2.00-2.24 mm, obtained by sieving a mixture of ZrO_2 beads (SiLiBeads). The dielectric constant of the ZrO_2 beads is in the range of 22-25.

To account for any possible adsorption of CO_2 on the packing material and to make sure that all residual air has left the reactor, we flush the reactor after opening for at least 20 min. with pure CO_2. During tests, after this time the base line was steady and no other gases than pure CO_2 were detected. In addition, we start the GC measurements only 20 min. after igniting the plasma, ensuring that the plasma reactor is in steady state when the gas is analysed.

4.3 Results and Discussion

In this section we will discuss the experimental results of the influence of the bead size, flow rate and applied power on CO_2 conversion and energy efficiency. We also investigated the effect of these parameters on the selectivities towards the formation of the end products, namely CO and O_2. However, as far as we could conclude from these experiments, the selectivities were always around 50% under all conditions, since the overall reaction of the splitting process is very simple: $CO_2 \rightarrow CO + \frac{1}{2} O_2$. Some traces of O_3 can in principle be formed, but the latter could not be detected with the used GC setup. In literature, O_3 formation is sometimes reported, but the values are at least an order of magnitude lower than the reported CO concentration.[54] In most cases, however, no O_3 formation is detected; the reaction simply gives rise to CO and O_2.[38, 42, 55] Furthermore, after the plasma treatment, no carbon deposition was found (based on visual inspection) on either the reactor walls or the packing beads.

4.3.1 Effect of Bead Size, Flow Rate and Applied Power

Figure 4-1 illustrates the CO_2 conversion (left) and energy efficiency (right) as a function of bead size, for three different gas flow rates and three different applied powers. The dotted lines represent the results of the unpacked reactor. It is clear that both the conversion and energy efficiency are strongly influenced by introducing a packing in the DBD reactor. At 60 and 80 W, a larger packing typically has a strong enhancing effect, while a smaller packing can actually lower the conversion and energy efficiency. The explanation for this phenomenon is probably that the residence time in the reactor filled with a smaller packing is too low to benefit from the enhancing effects of the presence of a packing. Indeed, smaller beads lead to a larger number of (enhancing) contact points, but also a lower residence time. Another explanation might be that there is only partial discharging in case of the smaller packing, which was not observable, due to the non-see-through nature of alumina, but it is described in literature.[40, 41] Moreover, in case of a smaller packing, with sizes at least four times smaller than the gap distance, the beneficial effects of the packing will have to spread over a larger number of contact points, which will make the enhancement at each contact point, and apparently also overall, lower than when fewer contact points are present. Therefore, in the following analysis we will mainly focus on the results from the larger bead sizes (1.60-1.80 and 2.00-2.24 mm diameter). Indeed, the highest obtainable conversions and energy efficiencies are reached with these two bead sizes.

Furthermore, it is clear from figure 4-1 that a lower flow rate will always have a higher conversion. This is logical, because it corresponds to a longer residence time in the plasma. On the other hand, it will lead to a lower energy efficiency, as follows directly from the formulas in previous chapter (section 3.1.2).

Increasing the applied power will increase the conversion, especially for the lower bead sizes, since the plasma power will also increase. This can be seen in table 4-1 which lists the plasma power corresponding to the three different applied powers, for each of the conditions. Depending on the bead size the resulting plasma power can vary, but it is clear that for each individual bead size, an increase in applied power corresponds to an increased plasma power.

Table 4-1 Obtained plasma power (in W) for each condition of flow rate, applied power and bead size.

Flow rate ($mL\ min^{-1}$)	$P_{applied}$ (W)	Bead size 0.90–1.00	 1.00–1.18	 1.25-1.40	 1.60-1.80	 2.00-2.24
20	60	16.7	12.8	14.9	24.6	23.5
20	80	28.7	34.2	30.2	43.3	37.2
20	100	48.8	61.9	39.1	61.1	66.1
50	60	17.0	11.1	11.8	21.1	21.5
50	80	28.1	36.6	27.5	42.3	37.1
50	100	46.2	59.3	38.1	63.1	65.3
100	60	15.6	19.1	13.1	21.7	17.0
100	80	25.8	37.2	29.5	41.2	35.9
100	100	46.1	62.1	36.5	61.2	64.5

When the applied power is above 80 W, the conversion for almost all bead sizes, especially the larger ones, decreases (figure 4-1). We believe that this may be attributed to a change in the discharge characteristics, possibly from a more surface type discharge at 80 W to a more filamentary discharge at 100 W, which has been explained in literature.[56] If this is indeed the case, then we may conclude that the type of discharge occurring at 80 W is more ideal for CO_2 splitting than at higher applied power. The energy efficiency, in turn, decreases with increasing applied power, which is again logical from the formulas in section 3.1.2.

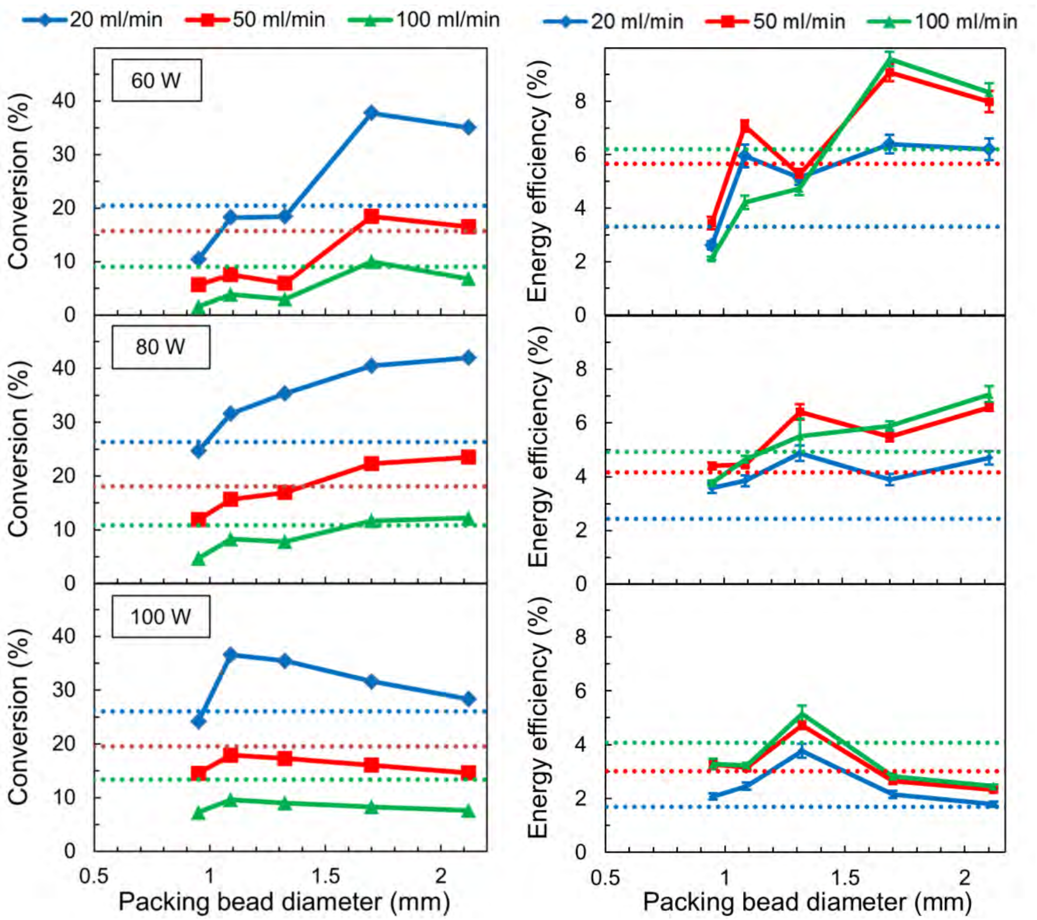

Figure 4-1 Measured CO_2 conversion and energy efficiency as a function of bead size for three different applied powers and three different gas flow rates. The dotted lines represent the results for the unpacked reactor. The error bars for the conversion are smaller than 0.5% and therefore not visible. The error bars for the energy efficiency are based on the error on the plasma power, flow rate and GC measurements. The symbols were reduced in size to increase visibility of the error.

4.3.2 Best Values Compared with Literature

The maximum conversion obtained in this study is 42.0%, and is reached with the largest bead size, at the lowest flow rate (20 mL min^{-1}) and with 80 W of applied power. The energy efficiency at this condition equals 4.7%. Compared to an empty reactor the conversion is a factor 1.6 better, and the energy efficiency has almost doubled (i.e., factor 1.9 increase). The maximum energy efficiency obtained is 9.6%, and this is reached with the highest flow rate (100 mL min^{-1}) and the lowest applied power (60 W) and bead sizes of 1.6-1.8 mm diameter, but it corresponds to a conversion of only 10.0%. In this case, the improvement factors over an empty reactor are 1.5 and 1.1, respectively. The most promising results are obtained for a packing with bead sizes between 1.60-1.80 mm diameter, with an applied power of 60 W and a flow rate of 20 mL min^{-1}. The conversion at this point reaches 37.8% with a corresponding energy efficiency of 6.4%. This is 1.9 and 1.8 times higher than without a packing, respectively. This is a very promising result, which shows us that the introduction of a packing can almost double the conversion and energy efficiency simultaneously, if the right input parameters are chosen.

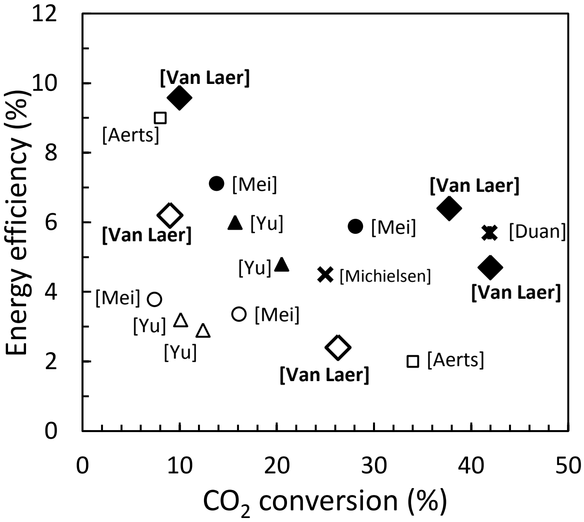

Figure 4-2 Comparison of CO_2 conversion and energy efficiency values from this work (Van Laer) with best available data in literature for CO_2 splitting in a PBPR. The filled and bold markers indicate a packing, while the empty markers stand for an empty reactor. For the packed reactors, the results of [Van Laer] were obtained with ZrO_2, [Mei] and [Michielsen] with $BaTiO_3$, [Yu] with $CaTiO_3$ and [Duan] with CaO beads.[38-42, 50]

In figure 4-2 the obtained results in this work are compared to the best available results for CO_2 conversion and energy efficiency in a (packed bed) DBD reactor presented in literature. Note that the number of papers to compare with is quite limited, because there are not so many papers available for pure CO_2 splitting (i.e. not mixed with e.g., a rare gas or CH_4) which report values for both conversion and energy efficiency. What immediately stands out is that a packed bed DBD reactor not only is capable of generating higher maximum conversions or energy efficiencies, but also provides better combined values of conversion and energy efficiency. In other words, the conversion and energy efficiency are both enhanced by the presence of the packing. Furthermore, it is clear that both the maximum obtainable conversion and energy efficiency are further increased in the present work compared to the best available data from literature, with the exception of the study of Duan et al. using a packed bed microreactor, which showed results in the same order.[42] Note that in chapter 6 we will computationally investigate the influence of the gap size. Our experimental results show that a variation of the packing bead diameter, flow rate and applied power can already lead to better results. In our opinion, the results with combined high conversion and high energy efficiency are the most promising. Indeed, it is not the search for the highest obtainable conversion or the highest possible energy efficiency that should be the focus of future research, but the combination of both. We believe that the results can be further improved by studying different packing materials with different dielectric constants, in combination with different packing geometries and even the presence of a catalyst on the surface.

Finally, to benchmark our results with best available technologies, we also compare them with studies for pure CO_2 splitting by other types of plasma, i.e. microwave plasma and gliding arc plasma. In the 1970s Fridman and colleagues showed that a microwave plasma reactor could be very promising for CO_2 splitting, by reporting energy efficiencies up to 80-90%.[24] However, these results were obtained at reduced pressure, between 0.02 and 0.05 atm, which is not practical for industrial implementation. Moreover, working at lower pressure also costs energy, which will significantly lower the total energy efficiency. To enable a better benchmark of our results, we should compare them with results from a microwave plasma at atmospheric pressure. Spencer et al. reported a maximum conversion of 45%, but this corresponded to a mere 5% energy efficiency.[57] The maximum energy efficiency of 21%, on the other hand, comes with a conversion of 10%. It is clear that with a microwave plasma higher energy efficiencies are feasible. However, to reach a conversion of at least 25% the energy efficiency will never exceed 7.5%, which is very much alike our results. An atmospheric pressure reverse vortex flow gliding arc discharge, as reported by Nunnally et al., can reach higher energy efficiencies, ranging from 18 to 43%.[58] However, the accompanied conversion is limited to 2-9%. The biggest advantage of a microwave and gliding arc reactor is their ability to cope with very high flow rates, reaching up to 16 L min^{-1} and 40 L min^{-1}, respectively. Their biggest disadvantage, however, is the fact that they are not as easily combined with catalysis as a packed bed DBD reactor. In this respect, we believe that a packed bed DBD reactor can be interesting towards future improvement, and future applications, certainly in combination with catalysis, for the selective production of value-added compounds.

4.4 Conclusion

We have demonstrated that a packing of ZrO_2 beads with a diameter of at least 1/3 of the gap size of the DBD reactor can significantly increase the conversion and energy efficiency of CO_2 splitting. In comparison with an empty reactor, the introduction of a packing can increase the conversion and energy efficiency up to almost a factor 2 simultaneously. The best combination of conversion and energy efficiency was reached with a bead size in the range of

1.60-1.80 at a flow rate of 20 ml min^{-1} and an input power of 60 W, yielding values of 37.8% conversion and 6.4% energy efficiency.

The results are very promising and clearly indicate that the introduction of a packing has beneficial effects on the conversion and energy efficiency of CO_2 splitting. We believe that the results can be further improved, by searching for the ideal packing geometry and the ideal dielectric constant of the packing material. Finally, it is worth to stress that a packed bed DBD reactor can also be realized with a catalytic packing, which is very promising for the selective conversion of greenhouse gases (CO_2 and CH_4) into value-added chemicals.

Chapter 5

Fluid Modelling of a Packed Bed Plasma Reactor

This chapter has been published as: K. Van Laer and A. Bogaerts, "Fluid Modelling of a Packed Bed Dielectric Barrier Discharge Plasma Reactor", *Plasma Sources Science and Technology* **25** (2016) 015002

5.1 Introduction

The beneficial effects of the introduction of a packing in a DBD reactor were clearly demonstrated in the previous chapter for the application of CO_2 splitting. However, the exact behaviour of the plasma, inducing the improved experimental results, is not at all clearly understood. As stated in chapter 2, it is difficult to achieve more insight using experimental diagnostics alone. Therefore a computational approach can be a very interesting tool towards a better understanding.

In principle, a PBPR should be studied in three dimensions to take into account the packing geometry as it is in real life. However, the duration of such 3D simulations is estimated to be well over a few months on today's modern computers, for just a couple of periods of the applied potential, at the conditions under study in our work (geometry, applied potential, frequency, gas mixture and pressure). Due to these computational limitations, a 2D model is needed to gain the first insights in the mechanism of a plasma discharge in a PBPR. It is of course key in such model to simplify the 3D geometry without compromising its authenticity. In this chapter, we focus on obtaining more insight into the formation and behaviour of a plasma in a PBPR at atmospheric pressure, as well as studying the influence of the applied potential on the discharge formation.

5.2 Modelling Details

The general fluid equations solved in this model are discussed in chapter 3. In this section we will discuss the pathway towards the best possible 2D representation, the plasma chemistry and the used boundary conditions.

5.2.1 Building the Geometry

Two different 2D axisymmetric geometries, based on a 3D unit cell of a close-packed PBPR are used to best represent the 3D problem (figure 5-1). The 3D unit cell contains two important geometrical properties, which need to be taken into account in the 2D adaptation. The contact points between the dielectric materials (i.e. beads, walls) are the first property. The contact points will strongly change the electric field distribution in the gas gap and will therefore have a big influence on plasma generation and distribution throughout the gap. In addition, these contact points also cause the voltage-driven electrode to be in direct contact with the grounded electrode, through a “channel of dielectric material”, lowering the electric field strength over the entire gap. We studied this phenomenon with simple electrostatic models (i.e. not including any plasma reactions) in 2D and 3D, and the results indicated that the influence of 2D vs. 3D was only minor, thus justifying the use of a 2D model. The second property is the existence of a so-called “channel of voids”. Indeed, just like the fact that all the dielectric materials are linked, all the voids in between the beads are also connected to each other, resulting in a direct channel from the dielectric layer on top of the voltage-driven electrode to the grounded electrode. This channel must be present because the plasma must be able to travel from one side of the discharge gap to the other. However, it is not possible to make a single axisymmetric 2D adaptation of the 3D unit cell with both the “channel of voids” present and all the packing beads in direct contact. Therefore, two different geometries are studied, each focusing on one of the properties. In both geometries, the rotational axis is located on the left side.

The first geometry shows two packing beads made of zirconia (dielectric constant, $\varepsilon = 25$) with diameters of 2.25 mm, on top of each other, making direct contact with each other and with the walls, which are 4.5 mm apart. We selected zirconia as the packing material, because of our experimental work described in chapter 4. In the next chapter, we will investigate the effect of different materials with different dielectric constants on the plasma behaviour in the PBPR. A 2.5 mm thick layer of alumina ($\varepsilon_r = 9$) is covering the voltage driven electrode. To overcome computational difficulties due to extreme mesh requirements, the contact points are slightly enlarged and rounded. This geometry will be called the “contact point model”.

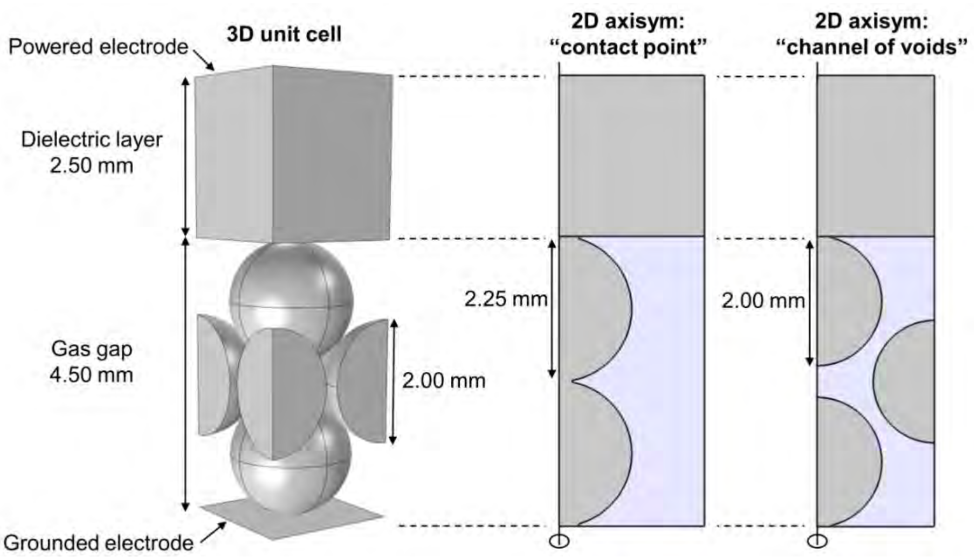

Figure 5-1 3D unit cell of the packed bed plasma reactor (PBPR) and its 2D representations used in the model.

The second geometry shows three packing beads, i.e., two beads on the left, with (the real) diameter of 2.00 mm and spaced apart so that they both are in contact with the opposite wall, leaving a gap of 0.5 mm in between. On the right side, another packing bead was added to create the “channel of voids”; therefore we will call this the “channel of voids model”. It must be realized that this packing bead after rotation around the axis will not be a sphere but a torus. Thus, both geometries are not a true copy of the real life geometry, but they can give us insights into the real life plasma behaviour.

As stated before, these models require a very fine mesh, due to the presence of the round edges of the packing beads and the sharp corners at the contact points. Triangular meshing is used across the whole geometry, except at the walls, where rectangular meshed boundary layers are added to better resolve the sheath formation. The distance between two mesh points in the gas gap is limited to 10 µm, and it is an order of magnitude smaller at the contact points. At the material surfaces, the distance between two mesh points is also limited to 1µm, in order to reach a good enough smoothness. Inside the dielectric material, the mesh is allowed to be coarser. As a result, the “contact point model” and the “channel of voids model” consist of 91202 and 73300 mesh elements, respectively. We performed a sensitivity study of the required mesh resolution, and found that a computation with less mesh points can lead to spike formation, whereas a calculation with more mesh points yields the same results but will only take longer.

5.2.2 Plasma Chemistry

Although this PBPR is mainly used for environmental applications, and thus in molecular gases, we apply the model in first instance to helium as the discharge gas, for two reasons. First of all, the reaction chemistry of this noble gas is quite simple, therefore limiting the calculation time. Second, it has the ability of forming a homogeneous instead of a filamentary discharge in a DBD reactor, and this is what we will be simulating by using a fluid model to describe the plasma. We focus here on the influence of a packing on the plasma formation and behaviour in a DBD reactor that would otherwise (without the packing) form a homogeneous discharge (i.e., using He as discharge gas). Since this is normally not the case for molecular gases, this limits the applicability of the obtained results. However, the insights that are gained will certainly be helpful for future research on PBPRs with more complex molecular gases. In chapter 8 we will take the first steps towards molecular gases by using dry air as discharge gas.

Table 5-1 Helium reaction set with rate coefficients, and references where these data are adopted from. T_e is the electron temperature (eV), T_g the gas temperature in eV and T_g' the gas temperature in K.

Nr.	Reaction	Rate coefficient	Ref
R1	$e + He \rightarrow He + e$	cross-section	59
R2	$e + He \rightarrow He^* + e$	cross-section	59
R3	$e + He^* \rightarrow He + e$	cross-section	60
R4	$e + He \rightarrow He^+ + 2e$	cross-section	59
R5	$e + He^* \rightarrow He^+ + 2e$	cross-section	59
R6	$e + He_2^* \rightarrow 2He + e$	3.8×10^{-9} cm^3 s^{-1}	61, 62
R7	$2e + He^+ \rightarrow He^* + e$	$6.0 \times 10^{-20} (T_e/T_g)^{-4.4}$ cm^6 s^{-1}	62
R8	$2e + He_2^+ \rightarrow He^* + He + e$	$4.0 \times 10^{-20} (T_e/T_g)^{-1}$ cm^6 s^{-1}	62
R9	$e + He_2^+ + He \rightarrow He^* + 2He$	$5.0 \times 10^{-27} (T_e/T_g)^{-1}$ cm^6 s^{-1}	62
R10	$2e + He_2^+ \rightarrow He_2^* + e$	$4.0 \times 10^{-20} (T_e/T_g)^{-1}$ cm^6 s^{-1}	62
R11	$e + He_2^+ + He \rightarrow He_2^* + He$	$5.0 \times 10^{-27} (T_e/T_g)^{-1}$ cm^6 s^{-1}	62
R12	$e + He_2^* \rightarrow He_2^+ + 2e$	$9.75 \times 10^{-10} T_e^{0.71} e^{-3.4/T_e}$ cm^3 s^{-1}	62
R13	$e + He^+ + He \rightarrow He^* + He$	$1.0 \times 10^{-26} (T_e/T_g)^{-2}$ cm^6 s^{-1}	62
R14	$e + He_2^+ \rightarrow He_2^*$	$5.0 \times 10^{-9} (T_e/T_g)^{-1}$ cm^3 s^{-1}	62
R15	$He^* + He^* \rightarrow He_2^+ + e$	$2.03 \times 10^{-9} (T_g/0.025)^{0.5}$ cm^3 s^{-1}	62
R16	$He^* + He^* \rightarrow He^+ + He + e$	$8.7 \times 10^{-10} (T_g/0.025)^{0.5}$ cm^3 s^{-1}	62
R17	$He^+ + 2He \rightarrow He_2^+ + He$	$1.4 \times 10^{-31} (T_g/0.025)^{-0.6}$ cm^6 s^{-1}	62
R18	$He^* + 2He \rightarrow He_2^* + He$	$8.1 \times 10^{-36} T_g' e^{-650/T_g'}$ cm^6 s^{-1}	62
R19	$He_2^* + He^* \rightarrow He^+ + 2He + e$	$2.03 \times 10^{-9} (T_g/0.025)^{0.5}$ cm^3 s^{-1}	62
R20	$He_2^* + He^* \rightarrow He_2^+ + He + e$	$8.7 \times 10^{-10} (T_g/0.025)^{0.5}$ cm^3 s^{-1}	62
R21	$He_2^* + He_2^* \rightarrow He^+ + 3He + e$	$2.03 \times 10^{-9} (T_g/0.025)^{0.5}$ cm^3 s^{-1}	62
R22	$He_2^* + He_2^* \rightarrow He_2^+ + 2He + e$	$8.7 \times 10^{-10} (T_g/0.025)^{0.5}$ cm^3 s^{-1}	62
R23	$He_2^* + He \rightarrow 3He$	4.9×10^{-16} cm^3 s^{-1}	61

The model considers six different species, i.e., electrons (e), neutral helium atoms (He), positive helium atomic and molecular ions (He^+, He_2^+), metastable helium atoms, He(2^1S) and He(2^3S) combined into one effective level He*, and helium dimers (He_2^*). The different species interact with each other by 23 elementary reactions (Table 5-1). The rates of the first five reactions (R1-R5) are obtained by Bolsig+, a software program that solves the Boltzmann equation for the electrons, using the input collision cross-sections from the LXcat database, to generate the electron impact reaction rates as a function of the mean electron energy.[59, 60] It also calculates the transport coefficients of the electrons as a function of mean energy. The reaction rate coefficients of the other 18 reactions (R6-R23), namely recombination reactions with electrons and heavy particle reactions between ions, atoms and excited species, are taken from literature, and are typically a function of electron temperature or gas temperature.[61, 62]

However, we assumed a constant gas temperature of 300 K. Indeed, our experiments revealed that the gas itself does not heat up in a PBPR with a gas flow as low as 20 mL min^{-1}. In the present model, we do not apply a gas flow. Since the model goes to steady state in only a few periods of applied potential, this is a correct representation of reality. However, since we do not have the inflow of "cool" gas, the gas might heat up if we would calculate it from the applied power, which would not reflect the reality of a gas flow. Therefore, we opted to keep the gas temperature constant. The mobilities $\mu_{i,j}$ of the ions are taken from literature, namely 1.0 × 10^{-3} m^2 V^{-1} s^{-1} for He$^+$ and 1.6 × 10^{-3} m^2 V^{-1} s^{-1} for He$_2^+$,[63] and the corresponding diffusion coefficients $D_{i,j}$ are obtained from the Einstein relation. Note that in this case j always stands for He, since we are not using a gas mixture, but pure He as discharge gas.

$$D_{i,j} = \mu_{i,j} k_B T$$

This yields values of 2.6 × 10^{-3} m^2 s^{-1} and 4.1 × 10^{-3} m^2 s^{-1} for He$^+$ and He$_2^+$, respectively. For the neutral species, the diffusion coefficients are calculated with the Chapman-Enskog equation.[64]

$$D_{i,j} = \frac{3k_B T \sqrt{\dfrac{4\pi k_B T}{2\mu_{ij}}}}{16 p \pi \sigma_{ij}^2 \Omega_D(\Psi)}$$

$$\text{with } \Omega_D = \frac{A}{\Psi^B} + \frac{C}{e^{\mathrm{D}\Psi}} + \frac{E}{e^{\mathrm{F}\Psi}} + \frac{G}{e^{\mathrm{H}\Psi}};\ \Psi = \frac{k_B T}{\varepsilon_{ij}};\ \sigma_{ij} = \frac{\sigma_i + \sigma_j}{2};\ \varepsilon_{ij} = \sqrt{\varepsilon_i \varepsilon_j}$$

In these equations k_B is the Boltzmann constant (1.38×10^{-23} J K^{-1}), T the gas temperature (K), p the total pressure (Pa), μ_{ij} the reduced mass (kg), σ_{ij} the characteristic length (m), $\Omega_D(\Psi)$ the dimensionless diffusion collision integral, Ψ the dimensionless temperature and ε_{ij} the depth of the Lennard-Jones potential for the He-He interaction (J). The parameters A-H were taken from literature.[65] The diffusion coefficients are calculated to be 1.68×10^{-4} m^2 s^{-1} for both the atomic neutral species, i.e. He and He*, and 1.45×10^{-4} m^2 s^{-1} for the molecular species He_2^*. An initial density of 10^{14} m^{-3} is assumed for both the electron and total ion density. This is quite high, and artificial. However, we have checked the effect of this assumption, and it was clear that these input values did not change the solution. They only help the model to start up easier, which saves calculation time in the beginning.

5.2.3 Boundary Conditions

The packing beads in each of the geometries are treated as solid objects with conservation of charge. On the surface, charge accumulation is possible by means of the following boundary conditions:

$$\boldsymbol{n} \cdot (\mathbf{D_1} - \mathbf{D_2}) = \rho_s$$

$$\frac{\partial \rho_s}{\partial t} = \boldsymbol{n} \cdot \mathbf{J_i} + \boldsymbol{n} \cdot \mathbf{J_e}$$

In these equations **n** stands for the normal vector, $\mathbf{D}_1$ and $\mathbf{D}_2$ are the displacement fields on both sides of the boundary, ρ_s is the surface charge (C m^{-2}), $\mathbf{n} \cdot \mathbf{J}_i$ and $\mathbf{n} \cdot \mathbf{J}_e$ are the normal components of the ion and electron current densities at the wall, respectively.

Finally, the different plasma species can also react at the walls. More specifically, the following surface reactions are taken into account: quenching of helium atomic and molecular metastables, and electron-ion recombination of He$^+$ and He_2^+ ions to ground state helium atoms, with a probability of 0.05 to send out a secondary electron with energy of 5 eV.[66] The boundary condition for the electric potential at an electrode is a predefined value, namely 0 V on the grounded electrode and V(t) on the powered electrode, where V(t) represents a radio frequency sine wave. The outer boundary on the right side of the geometries (figure 5-1) is treated with an insulation boundary condition, setting the normal fluxes of electrons and electron energy on this boundary to zero, and a zero charge boundary condition, defining the normal electric displacement equal to zero. The combination of these two boundary conditions implies periodicity, with a normal zero gradient of charged species across the boundary.

5.3 Results and Discussion

5.3.1 Contact point model

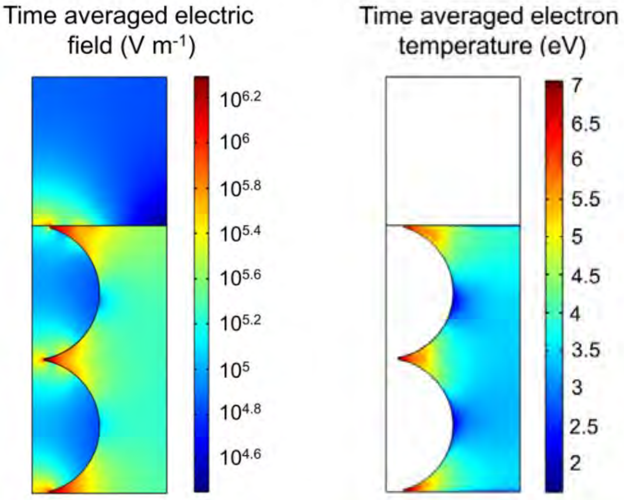

Figure 5-2 Time averaged electric field strength (V m^{-1}) and electron temperature (eV) over one period of applied potential, i.e. 4.0 kV peak-to-peak at a frequency of 23.5 kHz.

First we present the results for the "contact point model" with an applied sinusoidal voltage of 4.0 kV peak-to-peak at a frequency of 23.5 kHz. Figure 5-2 shows the time averaged electric field and electron temperature distributions over one period of applied potential. Due to the polarization of the packing beads as a result of the applied potential over these materials, the electric field at the contact points (both inside the materials and in the gas gap) will be enhanced. Hence, the electrons in this region will receive more energy than in the rest of the reactor. Therefore, when the breakdown voltage is reached, a discharge will be initiated at the contact points. When a low potential is applied, in our case 4.0 kV peak-to-peak, the discharge stays at this location, and behaves like a Townsend discharge: several low intensity current peaks per half cycle (equally spaced and decreasing in size; see figure 5-3 below), ion densities drastically exceeding the electron density, and an electric field that is weakly affected by the space charge.[67-69] The Townsend discharge is formed at two separate places in the reactor, namely at the contact point between the two dielectric beads, and at the contact point between the upper bead and the dielectric layer covering the powered electrode. At the contact point between the lower bead and the grounded electrode, no discharge will take place in spite of the considerable electric field, because of the presence of this electrode and thus, the lack of surface charge accumulation on its surface. Indeed, for a Townsend discharge the secondary electron yield from the surface is important to form a discharge.[70] The grounded metal electrode acts as a sink for charged species. If the grounded electrode would also be covered by dielectric material, a Townsend discharge would also be expected at the lower contact point.

The total current profile, i.e., the sum of displacement and conduction current, during one half cycle of applied potential (figure 5-3) shows a superposition of two current profiles of Townsend discharges (i.e. consecutive equally spaced peaks, decreasing in size), one with three peaks, and one with two peaks. Peaks 1, 2 and 4 originate from three consecutive Townsend discharges at the contact point between the beads, while peaks 3 and 5 are from two Townsend discharges at the contact point of the upper bead with the dielectric layer. A similar pattern applies to the other half cycle, except for the fact that the superposition is slightly different. Indeed, the two discharges between the upper bead and the dielectric layer happen earlier in the cycle, before the second and third discharge at the contact point between the beads, respectively. The current waveform is reproducible from the second cycle onwards. The first (and sometimes also the second) cycle generally shows a little difference, attributed to the start-up of the model in the beginning. The initial conditions will not have an influence on the reproducible part of the current waveform. They can only fasten the start-up (as mentioned before).

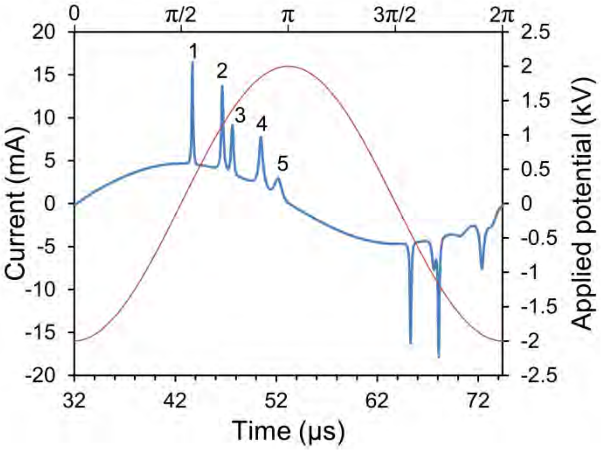

Figure 5-3 Total current profile during one cycle of applied potential of 4.0 kV peak-to-peak. The asymmetry between half-cycles is a direct result of the asymmetric nature of the used single layer DBD reactor.

The electron density distribution for the first breakdown at each of these places, in other words the electron density at the time of current peak 1 and 3, respectively, is shown in figure 5-4. These plots clearly show that the plasma is indeed formed locally, at different times during the half cycle. At 43.7 μs (left), a small plasma is formed at the contact point between the beads, while at 47.6 µs (right), the plasma is formed between the upper bead and the dielectric layer.

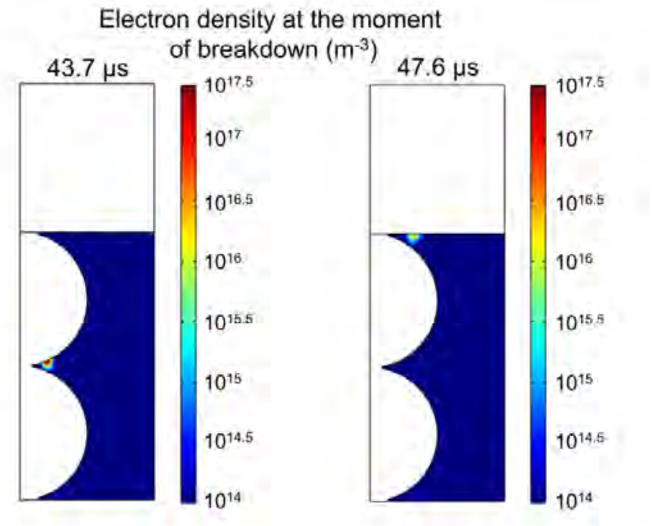

Figure 5-4 Electron density (m^{-3}) at the moment of gas breakdown at the two separate contact points, i.e., corresponding to peak 1 (left) and peak 3 (right) of figure 5-3 above, for an applied potential of 4.0 kV peak-to-peak.

To further demonstrate the occurrence of Townsend discharges, the time averaged electron density and total ion density distributions are compared in figure 5-5. It is obvious that the ion density is up to two orders of magnitude higher than the electron density, as expected for a Townsend discharge. The electrons have a much higher mobility, due to their lower mass, so they move towards the walls, thereby charging the dielectrics. To verify, the surface charge density was calculated at any moment in time in the reactor and showed that it was negative at every time step, proving that the missing electrons from the bulk are indeed charging the surface. The amount of electrons on the surface was comparable to the amount missing from the bulk within the order of magnitude. The reason why they are not perfectly the same, lies in the fact that some stabilization is used in the model that artificially increases the amount of electrons in places where there are very few. The impact of this stabilization on the results was tested by comparing the model with a similar model without this stabilization present, and thus total charge conservation. This last model runs less stable, and therefore takes more time, but in the end it showed the same results as the model with stabilization. Figure 5-5 also shows that the plasma never leaves the region at the contact points, and has a rather low time averaged density. Finally, it is clear that indeed no discharge is formed at the contact point between the lower bead and the grounded electrode, as explained above.

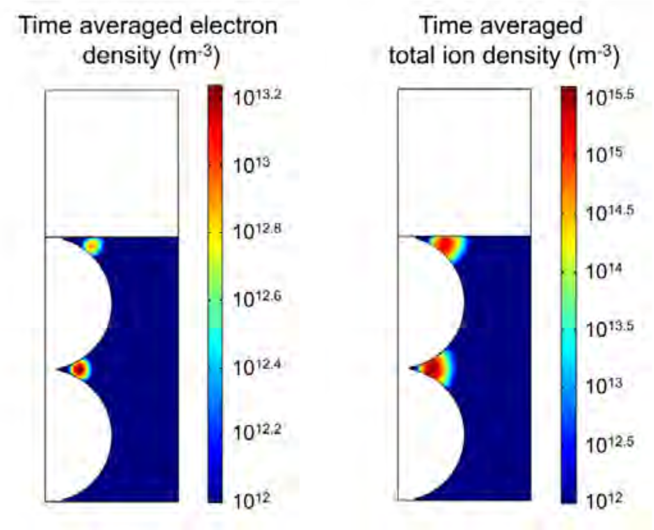

Figure 5-5 Time averaged electron density (m^{-3}) and total ion density (m^{-3}) for an applied potential of 4.0 kV peak-to-peak.

When a higher potential, for instance 7.5 kV peak-to-peak, is applied, the discharge will still be initiated at the contact points. However, since the potential difference over the full gap distance is now much larger, the discharge will quickly spread out over the surface of the packing beads towards the bulk and form a glow-like discharge, which is proven by the presence of a quasineutral plasma. The discharge can best be seen as a homogeneous discharge as expected in an empty reactor, but deformed by the presence of the packing material. Just like in the paper of Golubovskii et al. for a non-packed DBD reactor,[67] an ionization wave quickly travels towards the cathode when a discharge takes place (in a time frame of ns). This resembles the behaviour of a streamer. When it reaches the cathode, it creates a peak in the current, the spatial profile of the electric field changes and a glow-like discharge is formed that can last several μs. However, at the contact points, the discharge can quickly die out due to the small dimensions, which impede the formation of a quasineutral plasma zone.

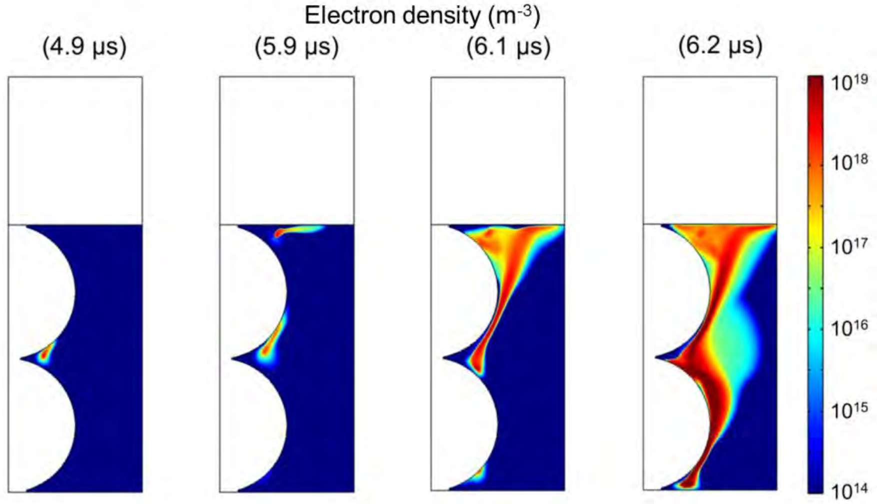

Figure 5-6 Instantaneous electron density (m^{-3}) at several consecutive moments in time after the moment of gas breakdown, indicating the course of events to form the final glow-like discharge, for an applied potential of 7.5 kV peak-to-peak

The course of events is illustrated in figure 5-6: the first discharge takes place at the contact point between the packing beads. Not much later, a second discharge is initiated at the contact point of the upper bead with the dielectric layer. Since the applied potential at this point is still increasing, a discharge can take place over the entire gap distance. However, because of the presence of the packing beads, and the accompanying electric field enhancement on the surfaces and at the contact points, the discharge will not be formed in the gap as expected for an empty reactor, but will be formed near the surface of the packing beads, from one contact point to the other. Figure 5-7 shows the time averaged electron and ion density distribution from the moment at which the full discharge over the surface is formed (after 6.2 µs, figure 5-6 right) until the end of the first half period, and illustrates the quasineutrality of the formed plasma discharge. The density of electrons tends to be a bit lower at the cathode surface (the dielectric layer) due to the presence of a cathode fall region. They also move faster through the bulk towards the nearby bead surfaces than the ions. Figure 5-7 also indicates that we are not dealing with a streamer discharge remnant, which would show a much higher ion density than electron density,[24] but an actual glow-like discharge that lasts for several µs.

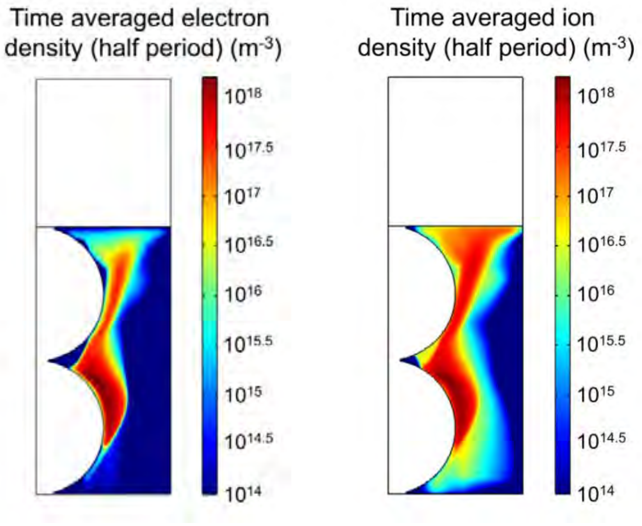

Figure 5-7 Time averaged electron density (m^{-3}) and total ion density (m^{-3}) from 6.2 µs until the end of the first half period, for an applied potential of 7.5 kV peak-to-peak.

5.3.2 Channel of Voids Model

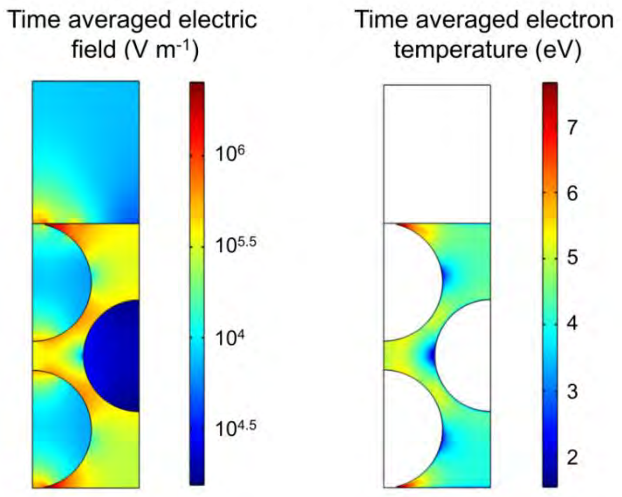

Figure 5-8 Time averaged electric field strength (V m^{-1}) and electron temperature (eV) over one period of applied potential of 4.0 kV peak-to-peak with a frequency of 23.5 kHz.

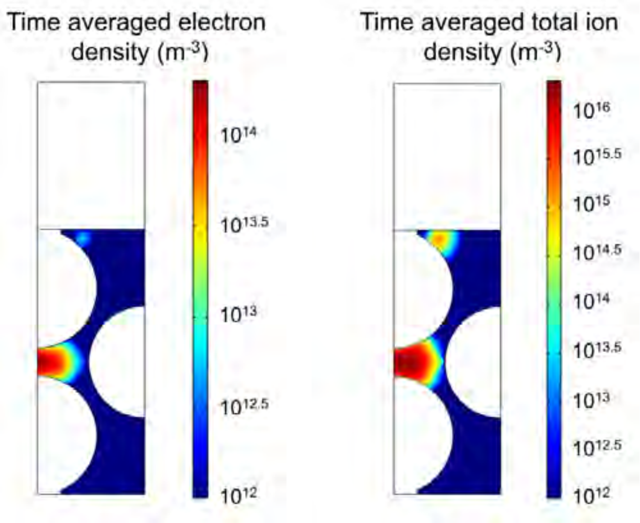

Figure 5-9 Time averaged electron density (m^{-3}) and total ion density (m^{-3}) for an applied voltage of 4.0 kV peak-to-peak.

At low applied potential of 4.0 kV peak-to-peak, the "channel of voids model" shows similar results as the "contact point model".

Again the electric field strength and electron temperature are strongly influenced by the presence of the packing beads and their polarisation, resulting in maxima near the contact points (figure 5-8). The values are slightly different because of the different geometry approximations, and the reality will probably be somewhere in between. Plasma initiation takes place between the two packing pellets on the left and at the contact point of the upper bead with the dielectric layer that covers the powered electrode, similar to the “contact point model”. Again the discharges stay in these regions and are Townsend-like, as demonstrated by the time averaged electron and ion density distributions, showing the absence of a quasineutral plasma (figure 5-9). The current profile over one half cycle of applied potential is not shown because it is almost identical to the current profile of the “contact point model” (figure 5-3).

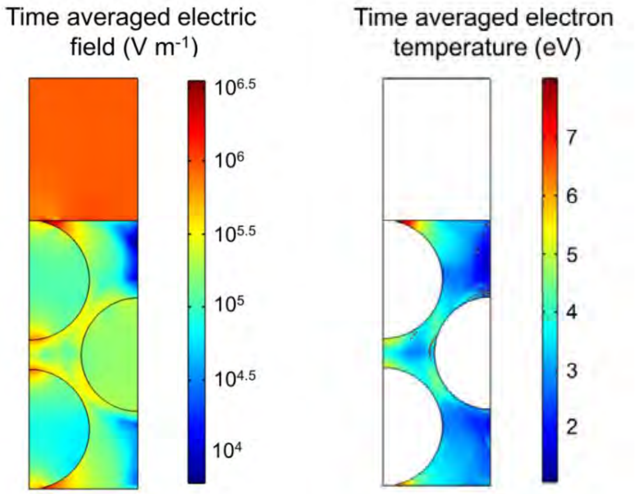

Figure 5-10 Time averaged electric field strength (V m^{-1}) and electron temperature (eV) over one period of applied potential of 7.5 kV peak-to-peak with a frequency of 23.5 kHz.

When the applied potential is increased to 7.5 kV peak-to-peak, the discharge behaviour changes drastically, with the third packing bead coming more into play. The electron temperature and electric field strength are still at maximum at the contact points, but typically show a lower value above and below the right packing bead (figure 5-10). This lower value is caused by the presence of a quasineutral plasma in these regions during most of the half cycle of the applied potential. Due to its high density, the resulting space charge strongly affects the external electric field. The discharge is no longer Townsend-like, but behaves more glow-like.

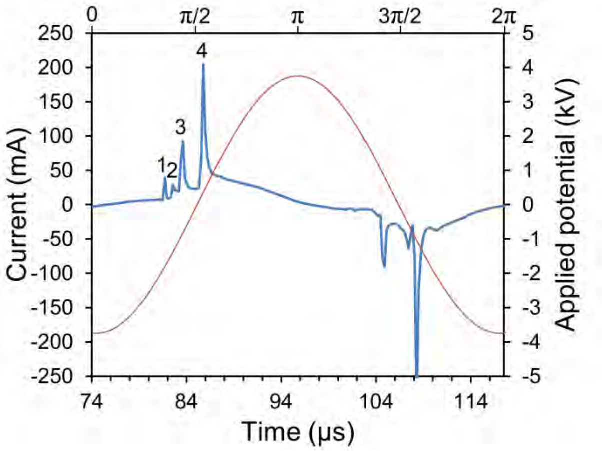

Figure 5-11 Total current profile during one cycle of the applied potential of 7.5 kV peak-to-peak.

The total current profile during one half cycle of the applied potential shows again a few consecutive peaks, as is the case at lower applied potential (cf. figure 5-3 above for the "contact point model", but the same result was also obtained with the present model), but at this higher applied potential, the peaks are much stronger (up to 200 mA, vs 10-15 mA at lower applied potential), and they are not spaced apart evenly (see figure 5-11). The course of events shows a lot of similarities with the "contact point model" at higher applied potential. The periodic current peaks are caused by the sequence of different discharges as shown in figure 5-12. The reason why they happen in this order is explained by the electric field strength. As the applied voltage increases, the electric field strength in the reactor is also enhanced. The local discharges take place separately and consecutively, in an order depending on the time at which the necessary electric field strength is reached to create a breakdown in the gas. At the first three peaks, consecutive local glow-like discharges are formed in different regions: first in the gap between the two beads on the left (peak 1), then between the upper left bead and the dielectric layer (peak 2), and finally a simultaneous discharge between the dielectric layer and the top of the right bead and between the bottom of the right bead and the grounded electrode (peak 3). Afterwards, a discharge is formed over the whole gap distance, with plasma travelling through the so-called "channel of voids" from one wall to the other, corresponding to the most intense peak 4. This behaviour can be observed from figure 5-12, from left to right. Again, for the second half cycle similar discharges take place, but the timing relative to each other can change. Nevertheless, the strongest current peak always represents the discharge over the whole gap distance.

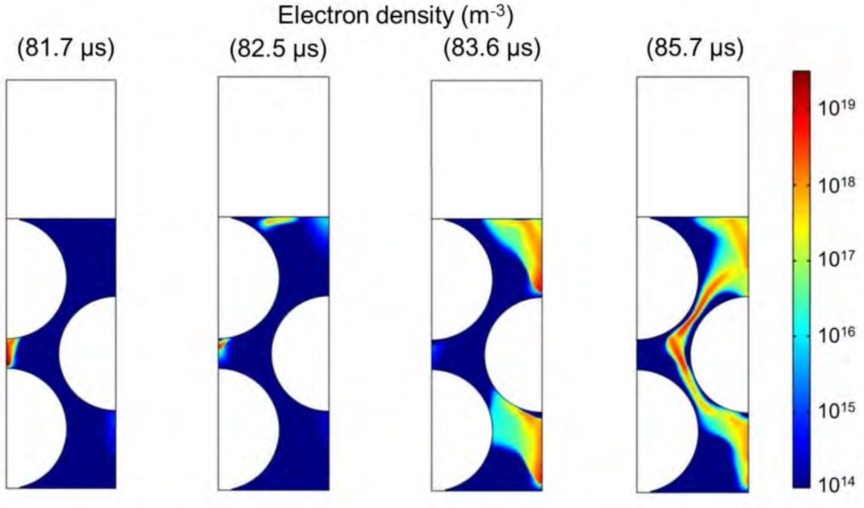

Figure 5-12 Electron density (m^{-3}) at four consecutive moments of gas breakdown for an applied potential of 7.5 kV peak-to-peak

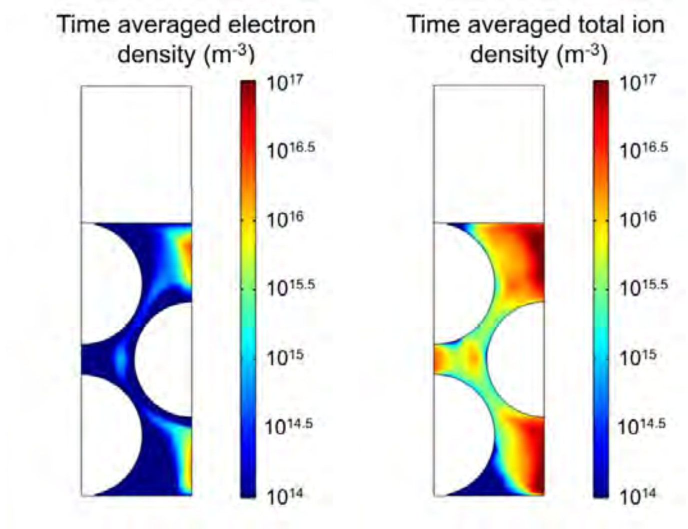

Figure 5-13 Time averaged electron density (m^{-3}) and total ion density (m^{-3}) for an applied potential of 7.5 kV peak-to-peak.

Above and below the packing bead on the right, the time averaged electron density and total ion density reach a similar maximum value, around 10^{17} m^{-3}, which we call quasineutral (figure 5-13). However, closer to the walls, the electron density decreases much more than the ion density, corresponding to the sheath formation. Indeed, an average electron temperature of 3 eV and electron density of 10^{16} m^{-3} lead to a Debye length of 0.13 mm (~1/15 of the total width of the geometry). The narrow gaps in a packed bed geometry therefore will clearly show this sheath formation.

The stronger current peaks, the more or less quasineutral plasma in the bulk and the resulting lower electric field strength in these regions all indicate that the discharge behaves more or less like a glow discharge. The fact that the plasma can travel through the so-called "channel of voids" shows that it is of key importance to include this phenomenon when studying packed bed DBD reactors. However, it is important to note that when the "channel of voids" would not be present, and in other words the dielectric beads would be overlapping, discharges would still occur in the resulting individual pores. According to Pechereau et al., these discharges are even able to continue through the dielectric material, hopping from one pore to the other.[71] Nevertheless, we believe that when we want to investigate a real 3D packed bed DBD reactor by means of a 2D model, the presence of a “channel of voids” cannot be neglected.

Validation of our computational results with experimental data is not straightforward, because of the difficulty of plasma diagnostics due to the presence of a packing, as mentioned in the introduction of this chapter. However, we can qualitatively compare our findings with experimental results reported by Kim et al. who used an intensified charge coupled device (ICCD) camera.[72, 73] The authors studied a parallel plate DBD reactor in air, filled with two different types of packing material, namely $BaTiO_3$ (ε = 10000) and a silver-doped high-silica Y zeolite (Ag/HSY zeolite, ε = 4-5) with air as the discharge gas. The latter packing material is the most interesting for us, because its dielectric constant is closer to the value considered in our work (i.e., corresponding to zirconia). The authors observed that at lower input potential the discharge stays local at the contact points, but at higher potential, it also appears further away across the surface of the zeolite, in a form which they call “surface streamers”. Tu et al. found some similar results using a $BaTiO_3$ packing in a parallel plate DBD reactor with argon as the discharge gas.[74] When the input power was increased, the discharge evolved from a local filamentary discharge between nearby bead surfaces to a more extensive surface discharge. Finally, also Ye et al. saw the presence of a so-called surface discharge on the air- and sand-millets in a parallel plate DBD reactor, while in an empty reactor only filamentary discharges occurred.[54] These experimental results strongly resemble our computational results. Especially the work by Kim et al. and Tu et al. matches exactly our findings on the influence of the applied potential on the plasma formation in a PBPR, namely that at lower applied potential, a local discharge takes place, while at higher applied potential, the discharge has the ability to travel further away or to be formed elsewhere.

Regarding the values of electron density and ion density, we can only compare with other models, such as the helium model of Golubovskii et al.[67] and Massines et al.[69], although they were not applied to a PBPR, since no experimental data is available. According to these papers, the density of the ions is typically up to two orders of magnitude higher than the electron density in a Townsend discharge, which is matched by our model (10^{15} versus 10^{13} m^{-3}). Furthermore, Golubovskii et al. found that the typical electron density at a current peak in a Townsend discharge is two orders of magnitude lower than for a glow discharge, which is also the case in our model (10^{17} versus 10^{19} m^{-3}). Finally, this model also tells us that the total current for a Townsend discharge is 1 to 2 orders of magnitude lower than the total current in a glow discharge. This all strengthens the idea that we are, indeed, dealing with Townsend and glow-like discharges, respectively.

5.4 Conclusion

We studied the behaviour of a PBPR by means of a fluid model. We applied two types of axisymmetric 2D models, i.e., a “contact point model” and a “channel of voids model”, to mimic as closely as possible the real 3D packed bed geometry, while avoiding excessively long calculation times. The results from the “contact point model” reveal that the plasma in a PBPR is initiated at the contact points, since this is the place with the highest electric field strength and thus the highest electron energy. When a low potential is applied, the plasma stays in this region, and shows the properties of a Townsend discharge. A higher applied potential will cause the discharge to further spread out into the bulk of the reactor towards the walls. The properties change to those of a glow discharge. The “channel of voids model" shows similar results. In this model, local Townsend discharges are also initiated at the position with high electric field strength, and they stay again in these regions at lower applied potential. When a higher potential is applied, glow-like discharges are formed, that can travel away from the contact points through the gaps between the contact points from one void to the other, ultimately covering the whole gas gap. It is therefore of uttermost importance to include this so-called "channel of voids" in a packed bed model, since the plasma will not stay localized when a higher potential is applied. These model results help us to obtain more insight in the plasma behaviour in a PBPR, which is difficult to obtain by plasma diagnostics.

Chapter 6

Effect of Gap Size and Dielectric Constant

This chapter has been published as: K. Van Laer and A. Bogaerts, "Influence of Gap Size and Dielectric Constant of the Packing on the Plasma Behaviour in a Packed Bed DBD Reactor: A Fluid Modelling Study", *Plasma Processes and Polymers* (2017) DOI: 10.1002/ppap.201600129

6.1 Introduction

In the previous chapter we studied the PBPR with two different axisymmetric 2D fluid models. These two complementary axisymmetric models (or geometries) each focussed on a specific characteristic feature of a PBPR. The first model considered a physical contact point between the beads, while the second model focussed on the connection between the void spaces. It was found that the discharge was always initiated at the position where the electric field and electron temperature are the highest, which is near the physical contact points. For studies of a few cycles of applied potential, the second model is better suited, because its geometry is closer to reality, with dielectric material blocking the open gas gap. At sufficiently high applied potential the discharge is able to spread across the gas gap, travelling through the "channels" that connect the voids.

In this chapter, we make use of the second model, i.e., the so-called "channel of voids" 2D axisymmetric model, to elucidate the pure dielectric effect of the packing beads in a packed bed DBD reactor, by investigating the influence of the dielectric constant of the packing material on the plasma behaviour in a helium discharge. In addition, we study the influence of the gas gap size on the dielectric packing effect, by comparing a normal mm-gap and a so-called microgap. As mentioned in chapter 4, Duan et al. studied a packed bed DBD microplasma, which yielded promising conversions and energy efficiencies for CO_2 splitting, in the same order, if not better than in a normal size reactor (chapter 4, figure 4-2).[42] The maximum achievable conversion in this microreactor setup was reported to be 41.9% for a packing of CaO, with an energy efficiency of 5.7%, while the highest conversion we reached in our study of a normal size packed bed DBD reactor was very comparable, namely 42% with a zirconia packing, but the corresponding energy efficiency was slightly lower, i.e., 4.7%. However, these results are not directly comparable since they use different packing materials. Moreover, the CO_2 capturing abilities of CaO can influence the results. In principle, a better comparison can only be made when the same packing material is used in both a microgap and mm-gap reactor. For γ-Al_2O_3, the maximum obtained CO_2 conversion reported for a microgap reactor is 16.3%, with an energy efficiency of 4.5%,[42] while in a mm-gap reactor, a comparable conversion of 16.0% could only be reached with a somewhat lower energy efficiency of 3.8%.[38]

A plasma is called a microplasma when it is confined to critical dimensions below approximately 1 mm.[75] The smaller space in a microreactor implies a stronger electric field and therefore a higher energy density. We will thus compare two different reactors, one large reactor with a gas gap of 4.5 mm and one microreactor with a gap of 0.5 mm. These reactors will be packed with different types of dielectric material, covering a wide range of dielectric constants, from 5 (glass, quartz) over 9 (alumina), 25 (zirconia) and 100 (titania), up to 1000 (barium titanate). The ratio of bead size over gap size will be kept constant in this study. In the next chapter we will investigate the influence of the bead size with constant gap size. Note that the actual size of the gas volume can be estimated to be close to 26% of the total volume, which would be the case if the packing fills the void space perfectly, as stated by the Kepler conjecture.

6.2 Modelling Details

The 2D axisymmetric fluid model is again developed with the built-in plasma module of the multiphysics software package COMSOL (version 5.0). For the general modelling equations we refer to chapter 3. The used plasma chemistry and boundary conditions are identical to the ones reported in chapter 5. We will therefore only discuss the building of the geometry in detail in this chapter, as it is the most defining part of the modelling process. Like in previous chapter, the discharge is operating at atmospheric pressure and the temperature is kept constant at 300 K.

6.2.1 Building the geometry

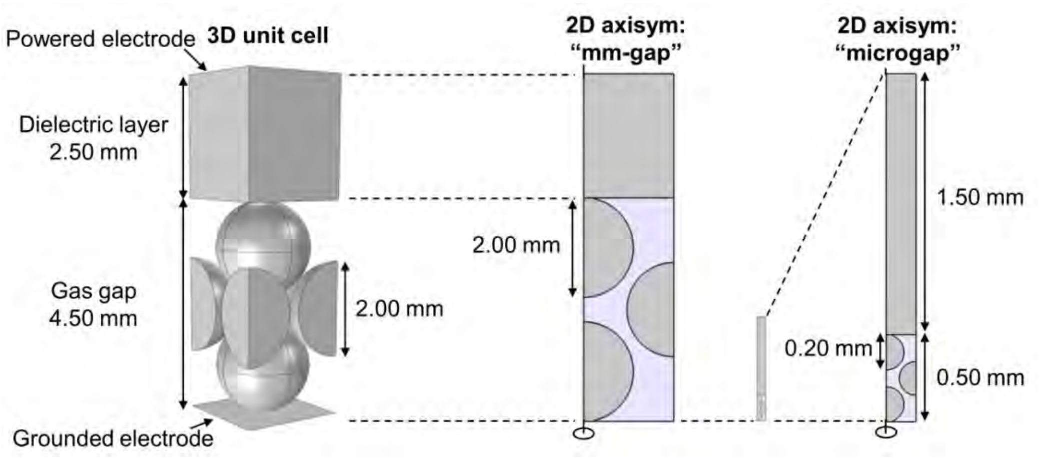

Figure 6-1 3D unit cell of the packed bed DBD reactor, and 2D axisymmetric geometry, used to mimic the packing effect, with dimensions indicated for both the mm-gap and the microgap reactor.

The investigated 2D axisymmetric geometry, both for the mm-gap and the microgap reactor, is again based on the same 3D unit cell as in chapter 5, here shown in figure 6-1. The stacking of the beads represents a face-centred cubic formation, but since the combination of the gap size and the bead diameter is not perfect, the top and bottom bead are a little bit closer to each other, creating some spacing between the four beads in the middle plane. As mentioned before, due to calculation time issues, the model cannot be solved in 3D. The 2D axisymmetric geometry uses several smart approximations to give the best possible representation of the real 3D geometry, with still a reasonable calculation time. In this chapter we opt to only use the "channel of voids" model. Indeed, it was illustrated in the previous chapter that the electric field enhancement obtained with a model considering no contact between the beads (like in the channel of voids model) was very similar to the results of a model with physical contact points (so-called “contact point” model). By using the channel of voids model, we lose the direct connection between the grounded and powered electrode through dielectric material. This connection has the ability to lower the electric field strength over the entire gap. However, as mentioned before, 2D and 3D electrostatic simulations (i.e. not including any plasma reactions) indicated that the influence of this connection is only minor. On the other hand, the connection of the void spaces between the beads was found to be crucial for a correct representation of the real geometry, and to account for this, the dielectric beads need to be separated from each other. Hence, this explains our choice of using the channel of voids model instead of the contact point model. The channel width in this 2D model is based on the diameter of the enclosed sphere that fits in the gap between three touching beads in the real 3D geometry. Note that in figure 6-1, the rotational axis is positioned on the left side of the geometry, so the beads on the right will actually have a torus-shape after rotation, which of course does not reflect the reality. However, we believe that the latter will have a minor effect on the plasma behaviour near the contact points and in the voids between the beads, and since we are limited to a 2D model, we believe that this geometry is the best possible approach.

6.3 Results and Discussion

6.3.1 Influence of the Gap Size

To illustrate the influence of the gap size on the discharge behaviour, the results for both a large gap of 4.5 mm (mm-gap) and a smaller gap of 0.5 mm (microgap) are compared for the same packing with ε = 25 and the same applied potential of 7.5 kV peak-to-peak. First, we take a look at the current profiles over one cycle of applied potential, as illustrated in figure 6-2. Note that to calculate the current, the size of the electrode surface has to be known. In the model this is the size of the circle formed by rotating the grounded electrode around the axis of symmetry. However, to make the modelling results representative for a full reactor and comparable with experiments, the current values are multiplied by a factor that represents the ratio between the real electrode surface and the modelled circle. The real electrode surface is calculated from the experimental cylindrical reactor geometry, found in chapter 4. Because it is a cylindrical DBD reactor, the top and bottom surface (or more specifically, the surface area of the outer and inner cylindrical electrodes) will not be exactly the same, and therefore the average is taken. The microgap reactor is assumed to be formed with the same dielectric (alumina) tube (i.e. the same inner diameter), but with an inner electrode with much larger diameter than for the mm-gap reactor, reaching a gap of 0.5 mm.

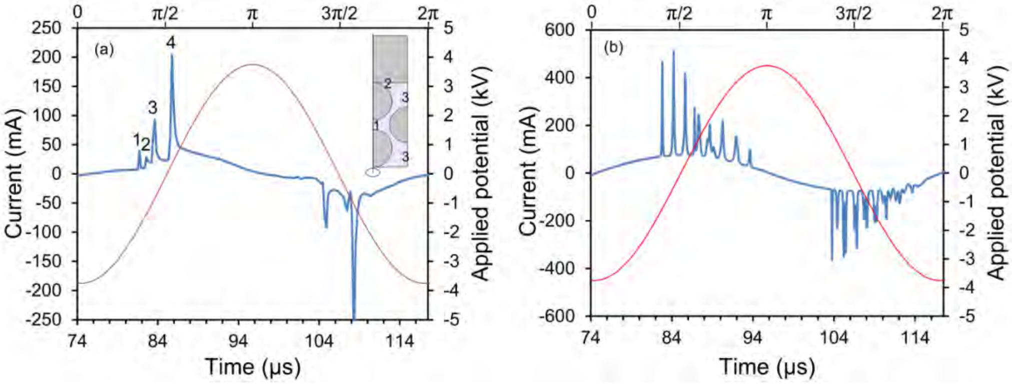

Figure 6-2 Current profiles of the mm-gap (a) and microgap (b) PBPRs with a zirconia packing, for one cycle of applied potential.

The discharge in the mm-gap reactor is characterised by a few current peaks per half cycle, shown by figure 6-2(a). The first three peaks are caused by local discharges, which are found in between the beads on the left (1), at the contact point of the top bead with the dielectric layer (2), and above and below the bead on the right (3), respectively (see the inset in this figure). The fourth and strongest current peak comes from a discharge spreading over the full height of the gas gap, travelling through the channels that connect the voids. The maximum values of electron density and total ion density are comparable here (see below); in other words, the plasma is more or less quasineutral. However, near the walls the electron density will be lower, due to sheath formation.

In the microgap reactor, the discharge behaviour is totally different. Figure 2(b) shows that the same applied potential yields much more current peaks per half cycle, and they are also up to a factor 4 higher than in the mm-gap reactor. These current peaks are coming from consecutive discharges taking place in the void spaces between the two beads on the left, and above and below the bead on the right. The discharge no longer travels through the gaps between the beads, but stays localised in the voids (see below).

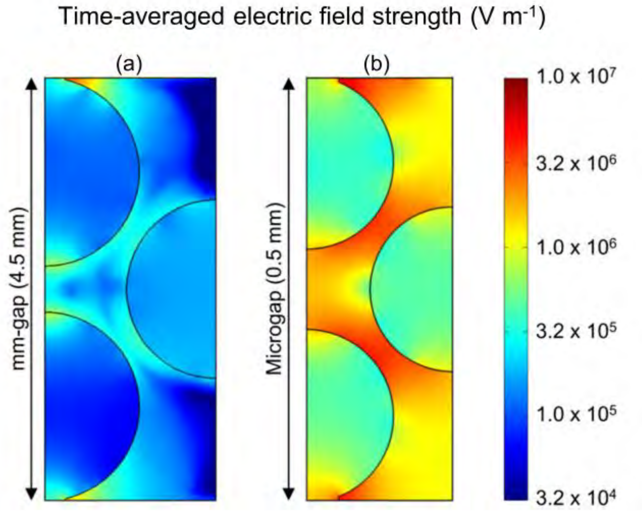

Figure 6-3 Time averaged electric field strength of the mm-gap (a) and microgap (b) reactors with a zirconia packing, for one cycle of applied potential.

The following time averaged 2D plots are constructed by averaging over 200 individual results per cycle of applied potential, i.e. an output every 2×10^{-7} s. This is sufficiently small since in helium, no short lived filamentary discharge behaviour is expected, that would negatively affect the averaging. From figure 6-3, it is clear that the time averaged electric field in the microgap reactor is much higher than in the mm-gap reactor, especially in the channels between the voids (i.e. up to 10^7 V m^{-1} in the microgap vs 6.5×10^6 V m^{-1} in the mm-gap reactor). As a result, the critical electric field strength to create a breakdown in the gas is more often reached in the microgap reactor, thus resulting in much more current peaks per half cycle of applied potential.

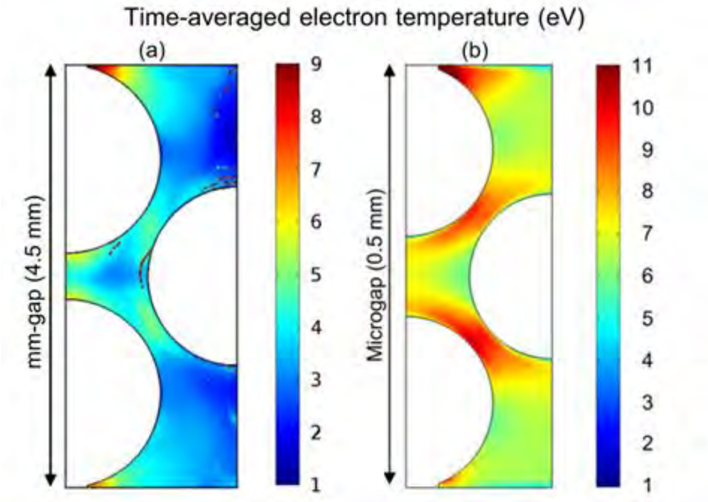

Figure 6-4 Time averaged electron temperature of the mm-gap (a) and microgap (b) reactors with a zirconia packing, for one cycle of applied potential.

The 2D electron temperature profile in figure 6-4 looks very similar to the electric field distribution. When the electric field is strong, the electrons are accelerated more, leading to an enhanced electron temperature. Therefore, the maximum values of electron temperature will also be found near the contact points and in the channels between the voids, where the beads are the closest to each other. In general, the electron temperature is again much higher in the microgap reactor, with values up to 11 eV at the contact points and in the channels between the voids, and in the order of 6 eV in the voids, while in the mm-gap reactor, the electron temperature is only around 3 eV in the voids, rising up to 6 eV in the channels between the voids, and up to 9 eV at the contact point between the upper beads and the dielectric layer. This difference directly arises from the higher electric field strengths in the microgap DBD reactor, shown in figure 6-3 above.

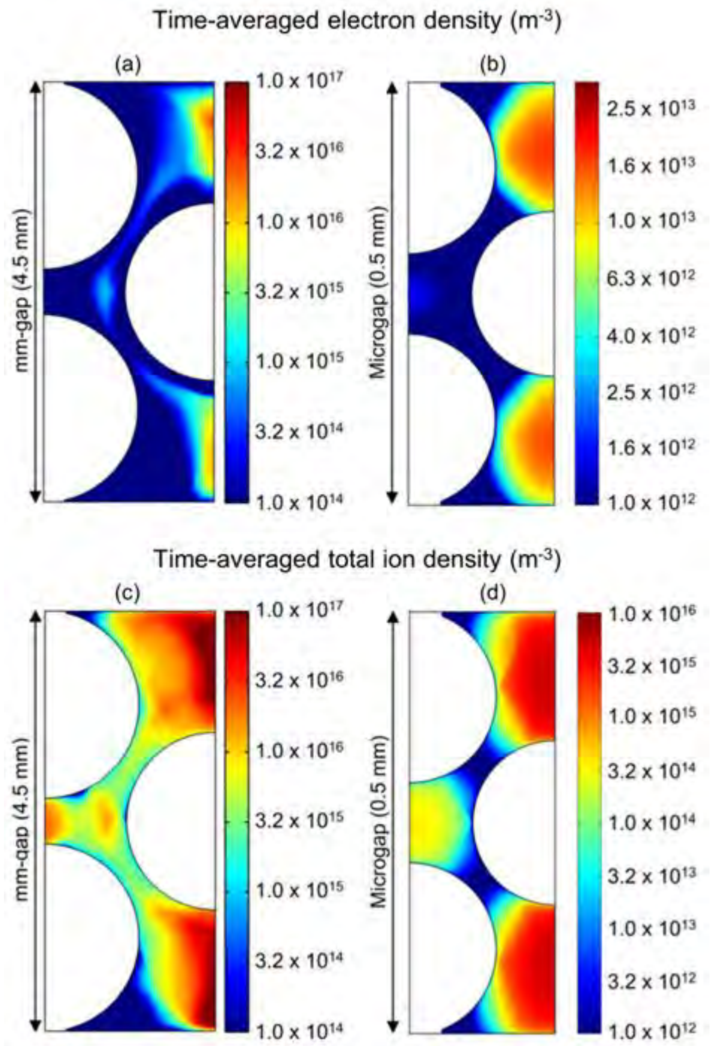

Figure 6-5 Time-averaged electron density (m^{-3}) and total ion density (m^{-3}) in the mm-gap (a,c) and microgap (b,d) reactors with a zirconia packing, for one cycle of applied potential. Note the difference in scale between the electron density and total ion density for the microgap reactor.

The time-averaged electron and total ion density profiles in figure 6-5 show that the maximum plasma density in the microgap reactor is spread out more evenly over the different void spaces, whereas for the larger reactor the most intense plasma is located in a thin area directly above and below the centre of the bead on the right. Close to the boundaries, a strong density gradient exists in both cases. In the microgap reactor, due to the small dimensions, the plasma loses its quasi-neutrality (note the difference in electron and total ion densities in both legends). The fast electrons will accumulate on the dielectric surfaces, while the slower ions can stay longer in the void spaces. Nevertheless, also the maximum ion density is one order of magnitude lower than in the mm-gap reactor for the same applied potential, again due to more losses at the walls as a result of the smaller dimensions.

Furthermore, the combination of the enhanced electric field strength in the channels between the voids, which implies faster travelling electrons, and the smaller channel width itself, leads to the fact that in the channels between the voids in the microgap reactor, electrons are more likely to be absorbed at the walls. Indeed, the beads are too close to each other, and do not allow a high density of highly energetic electrons to exist in the channel between the voids, without them hitting (and charging) the walls, and thus being removed from the gas gap. This explains why no plasma exists in the channels in this case (for a dielectric constant of 25), as is clear from figure 6-5(b,d). Our results can be linked to experimental observations by Ohsawa et al., who investigated the discharge characteristics of parallel electrodes with a disc of fused glass beads inside.[76] Their results showed that an increase in bead size implied a fewer number of current peaks with higher amplitude. Indeed, we also see less current peaks in the mm-gap reactor (with large beads) than in the microgap reactor. However, in our case the size of the gas gap and thickness of the dielectric layer do not stay constant, which explains why the amplitude will also increase for the microgap reactor. A thinner dielectric layer and smaller gap imply more power available, and therefore stronger current peaks.

Thus we can conclude that the discharge in the microgap and mm-gap packed bed DBD reactors is clearly different, with a higher electric field and electron temperature in the microgap reactor, leading to more current peaks per half-cycle, but also a lower plasma density and no quasi-neutral plasma in the voids between the beads, and even virtually no plasma formation in the channels between the voids, because of the smaller dimensions. However, also the dielectric constant of the packing has an influence on the discharge mechanism, which will be discussed below.

6.3.2 Influence of the Dielectric Constant

We performed calculations for five different packing materials, with dielectric constants ranging from 5 (glass, quartz) over 9 (alumina), 25 (zirconia) and 100 (titania), up to 1000 (barium titanate). The dielectric constant of the dielectric layer covering the powered electrode was kept constant at 9 (alumina). In figure 6-6 the time- and space-averaged electric field strength, electron temperature and electron density are plotted for both the microgap and the mm-gap as a function of dielectric constant. The electric field strength in the gas gap (figure 6-6(a)) increases with the dielectric constant, which is expected. The higher the dielectric constant of the material, the stronger is the polarization of the material, and thus the greater is the difference between opposite charges at the contact points between the packing and the dielectric layer, and between two packing beads. For the mm-gap reactor, the electric field strength increases gradually with rising dielectric constant until $\varepsilon = 100$, while a further increase in dielectric constant does not result in a further enhancement of the electric field. This phenomenon was first reported by Chen et al. based on an approximative equation describing the electric field in a spherical void developed by Takaki et al.[27, 44] The authors claimed that the enhancement of the electric field stagnates after a dielectric constant of around 100, in correlation with our results for the mm-gap reactor. Mei et al. found comparable results in their experimental study on the conversion of CO_2 in a DBD filled with either glass beads, $BaTiO_3$ beads or no beads at all.[37] At a constant applied power, the average electric field strength increased when the glass packing was replaced with $BaTiO_3$ beads. Note that the applied potential was not constant in their study, due to the use of a power-driven source.

In the microgap reactor, on the other hand, the electric field strength only rises as a function of dielectric constant between $\varepsilon = 5$ and $\varepsilon = 9$, while larger dielectric constants do not result in a further enhancement of the electric field. The increase in electric field strength from $\varepsilon = 5$ to $\varepsilon = 9$ can be explained as follows. When the dielectric constant of the packing material ($\varepsilon = 5$) is lower than the dielectric constant of the dielectric layer ($\varepsilon =9$), the strongest polarisation of material takes place near the contact point between the dielectric layer and the upper packing bead. Therefore, the electric field is mainly enhanced at this contact point, but it is only very slightly enhanced in the rest of the reactor, like in the channels where the beads are the closest to each other; see figure 6-7(a). As a result, the overall (space- and time-averaged) electric field will be much lower at $\varepsilon = 5$, compared to dielectric constants equal to or higher than the dielectric constant of the dielectric layer, where the polarization is also rather strong in the rest of the reactor. This lower electric field will even affect the mechanism of the discharge, which will be explained below.

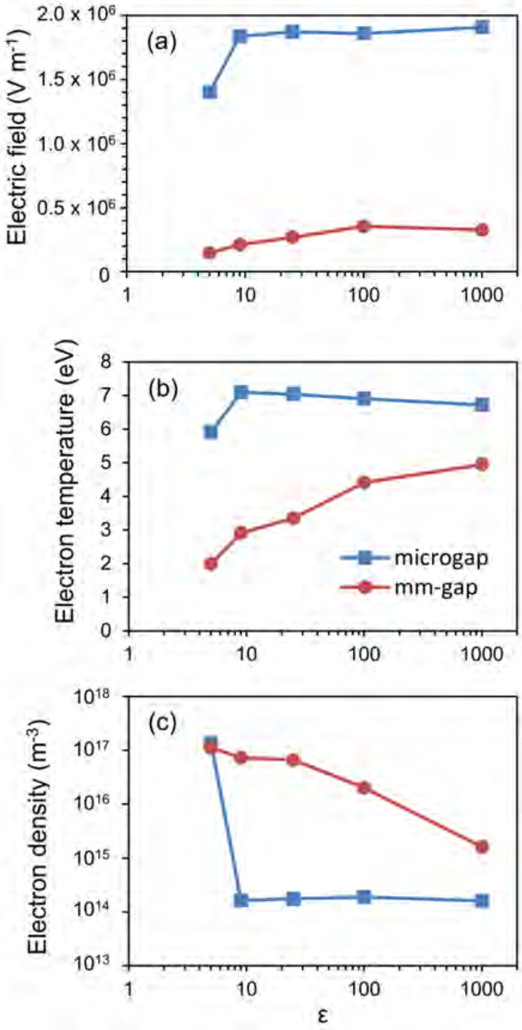

Figure 6-6 Influence of the dielectric constant on the space- and time-averaged electric field strength, electron temperature and electron density, for both the microgap (squares) and the mm-gap (circles) reactor.

Increasing the dielectric constant from ε = 9 to higher values again results in a more pronounced enhancement of the electric field at the top contact point than at the bottom contact point with the grounded electrode, which is shown in figure 6-7.

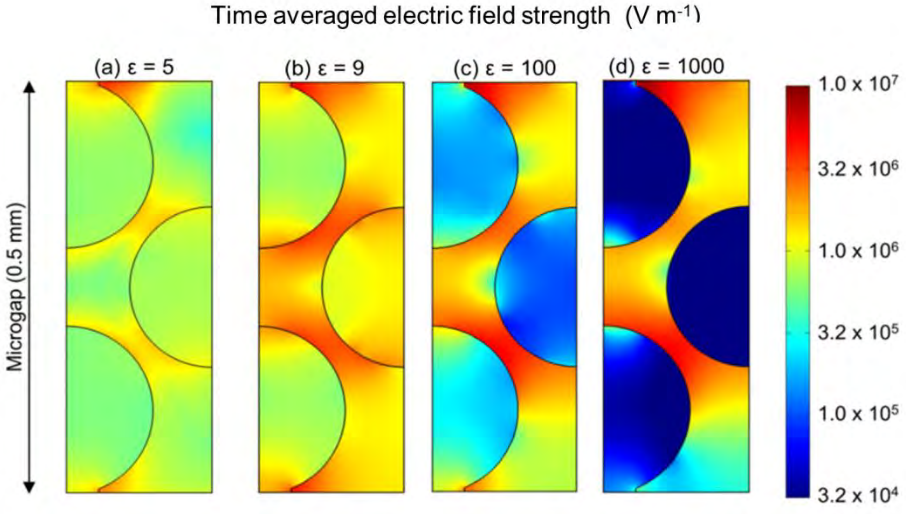

Figure 6-7 Time-averaged electric field strength in the microgap reactor for different packing materials: ε = 5 (a), 9 (b), 100 (c) and 1000 (d), for one cycle of applied potential. The electric field strength for ε = 25 was illustrated in figure 6-3 (b) above.

This can again be explained by means of the polarization, and is a direct result from the fact that we consider a DBD reactor with only one dielectric barrier. Indeed, the difference in charge will always be lower between a charged and uncharged surface (i.e. ground electrode) than between two oppositely charged surfaces. As the dielectric constant of the packing material increases, this effect becomes more pronounced (see figure 6-7(c,d)). Due to the small dimensions in the microgap reactor, the electric field in the two channels where the beads are closest will also be affected. The strong electric field at the top contact point, which is spread out quite far due to the small void spaces, will have a lowering effect on the electric field in the top channel. As a result, the electric field in the lower channel will be enhanced. However, the electric field enhancement near the grounded electrode is very limited (see figure 6-7(c,d)). Therefore, the overall (space- and time-averaged) electric field strength will remain more or less constant upon increasing dielectric constant.

The space- and time-averaged electric field strength in general is more than an order of magnitude higher in the microgap reactor than in the mm-gap reactor (see figure 6-6(a)), which is expected because the same potential difference is applied over a much smaller distance, so the delivered power per unit of distance is much higher in the microgap reactor. On the other hand, if we compare in both cases the value of the highest and the lowest electric field strength obtained, it is clear that the difference is larger in the mm-gap reactor. Indeed, the mm-gap reactor has an enhancement factor (i.e., ratio of highest and lowest electric field) of 2.4, i.e., 3.54×10^5 V m^{-1} (at $\varepsilon = 100$) vs. 1.48×10^5 V m^{-1} (at $\varepsilon = 5$), while the enhancement factor in the microgap reactor is only 1.4, i.e. 1.91×10^6 V m^{-1} (at $\varepsilon = 1000$) vs. 1.40×10^6 V m^{-1} (at $\varepsilon = 5$). In other words, our model predicts that the influence of changing the packing material on the electric field strength will be larger for the larger gap size. It would be nice if the effect of the dielectric constant on the electric field could also be measured experimentally in a mm-gap vs. microgap set up, to validate our model predictions.

The electron temperature in figure 6-6(b) follows the same trend as the electric field strength, with a few minor differences. For the mm-gap reactor, the electron temperature increases gradually upon rising dielectric constant, up to $\varepsilon = 1000$, while for the microgap reactor, the electron temperature decreases slightly above a dielectric constant of 9, instead of remaining more or less the same, like for the electric field strength. As discussed above, when the dielectric constant rises, the electric field strength is more enhanced at the top contact point than at the bottom contact point with the grounded electrode. The influence on the overall electric field strength is rather small, but the effect is much more pronounced on the electron temperature. Indeed, because the electrons cannot be accelerated to the same extent in the bottom part of the reactor, the overall electron temperature slightly decreases with increasing dielectric constant. For the mm-gap reactor this phenomenon also takes place, but because of the larger dimensions it does not have the same impact. Here, the enhancement in the top part of the reactor has a larger influence on the electron temperature than the reduced effect in the bottom part, which explains why the space- and time-averaged electron temperature gradually increases upon rising dielectric constant, even between $\varepsilon = 100$ and 1000, where the electric field strength has saturated.

The electron temperature is again lower in the mm-gap reactor than in the microgap reactor, due to the lower electric field strength, but because it keeps on rising with increasing dielectric constant, it is a factor 3 lower than in the microgap reactor for $\varepsilon = 5$, while it is only a factor 1.4 lower for $\varepsilon = 1000$. This suggests that the advantage of a microgap reactor, in terms of enhanced electric field and electron temperature, is more prominent for packing materials with smaller dielectric constants, but is obviously reduced for packing materials with larger dielectric constants. The trend in the mm-gap is consistent with the results found by Mei et al.[39] Again, it would be nice if more experiments could be performed for a microgap reactor, so that the calculated trends could be verified in more detail.

The electron density in figure 6-6(c) shows the opposite behaviour than the electric field strength, because it drops upon increasing dielectric constant. The stronger the electric field, the lower is the electron density and vice-versa. Indeed, a stronger electric field strength implies faster travelling electrons and thus more collisions with the walls, removing the electrons from the gas gap, and charging the surfaces. At $\varepsilon = 5$, the space- and time-averaged electron density is roughly the same for both the microgap and mm-gap reactor. For the mm-gap reactor, the electron density drops only slightly from $\varepsilon = 5$ to $\varepsilon = 25$ but then it drops a factor 40 from $\varepsilon = 25$ to $\varepsilon = 1000$. On the other hand, for the microgap reactor, a drop in electron density by 3 orders of magnitude is observed, when increasing the dielectric constant from 5 to 9, while for higher dielectric constants, the electron density stays more or less constant. At $\varepsilon = 1000$, the space-and time-averaged electron density in the microgap reactor is about one order of magnitude lower than in the mm-gap reactor.

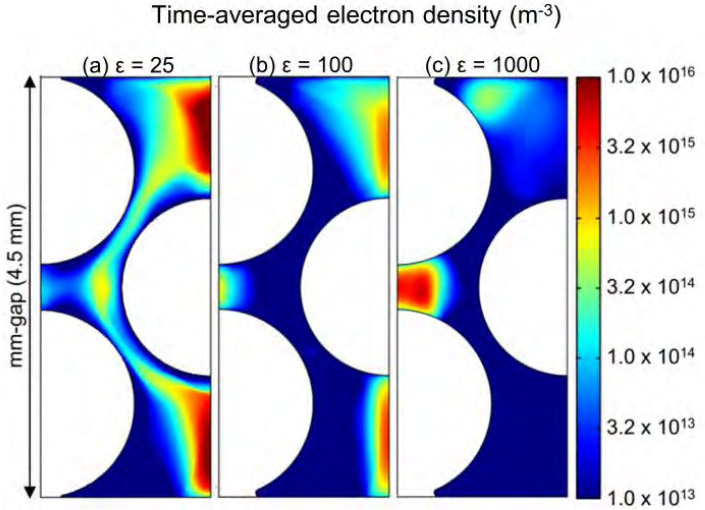

Figure 6-8 Time averaged electron density in the mm-gap reactor for three different packing materials: ε = 25 (a), 100 (b) and 1000 (c), for one cycle of applied potential.

The reason of the significant drop in electron density upon increasing dielectric constant, i.e., between ε = 25 and 1000 in the mm-gap reactor, and between ε = 5 and 9 in the microgap reactor, can be explained from the fact that the discharge behaviour changes significantly within this range of dielectric constants. Indeed, in the mm-gap reactor, when the dielectric constant rises from 25 to 100, the plasma cannot flow anymore through the channels between the voids, as is clear from figure 6-8. The discharges preferably take place above and below the right packing bead and in between the two packing beads on the left. The reason is that the electric field enhancement becomes too strong in the channels between the voids, accelerating the electrons so that they get more easily absorbed at the beads. The overall plasma volume will thus be lower, which results in a lower overall (space- and time-averaged) electron density, as shown in figure 6-6(c) above. Further increasing the dielectric constant to

1000 will shift the electric field enhancement to the top part of the reactor, very similar to what happens in the microgap reactor already at lower dielectric constants of ε = 25, as discussed before. As a result, no plasma will be formed anymore between the bead on the right and the grounded electrode (cf. figure 6-8), resulting in an even lower overall electron density.

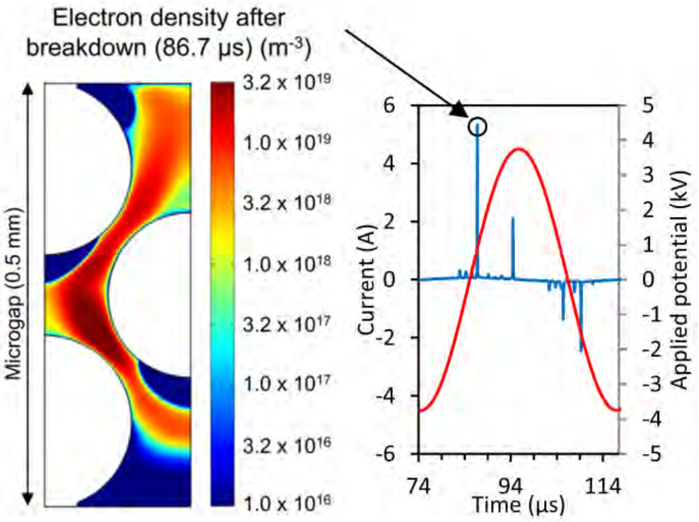

Figure 6-9 Electron density in the microgap reactor with glass beads (ε = 5), immediately after the breakdown at 86.7 μs.

For the microgap reactor, the strong drop in space- and time-averaged electron density from ε = 5 to ε = 9 can be explained because the plasma behaviour at ε = 5 is quite different from the behaviour at higher dielectric constants (cf. the behaviour for ε = 25 discussed before). When ε = 5, and thus lower than the value of the dielectric layer, the plasma gains the ability to flow through the channels between the voids, because the electric field strength will not be as strongly enhanced in the channels between the voids as at higher dielectric constants. Instead of the multiple current peaks as seen in figure 6-2(b), the current profile will now only contain two very strong current peaks per half cycle, arising from two consecutive discharges flowing through the channel of voids, as shown in figure 6-9. The full gas gap can be filled with plasma, resulting in a much higher overall electron density. At higher dielectric constants, even at ε = 9, this is not possible anymore, as discussed before, explaining the strong drop in space- and time-averaged electron density, illustrated in figure 6-6(c) above.

To summarize, upon increasing dielectric constant, the electric field strength is more enhanced at the contact points between dielectric materials or in places where these materials are close to each other. However, since we are studying a DBD reactor with only one dielectric barrier, the electric field enhancement and thus the ability to cause a breakdown will become lower near the grounded electrode, which is not covered by a dielectric layer, upon increasing dielectric constant of the packing. At low dielectric constant of the packing, when the polarization and thus the electric field enhancement is somewhat more limited, the discharge can more easily flow through the channels between the voids. However, at higher dielectric constants, the plasma loses this ability and ultimately shifts to the top part of the reactor, away from the grounded electrode. When the dimensions of the reactor are smaller, the influence of an increase in dielectric constant is much more pronounced, causing the plasma to change its behaviour much earlier, namely already between ε = 5 and 9.

6.3.3 Link with Experimental CO_2 Splitting

To answer the question whether a smaller packed bed DBD reactor will eventually be better for use in environmental applications like CO_2 splitting, we combine our calculated mean electron energy and electron density data at every mesh point and at every time step with a look-up table for the electron impact dissociation rate constant of CO_2 as a function of mean electron energy, in order to estimate the CO_2 dissociation rate. Figure 6-10 gives a visual representation of this look-up table. The dissociation rate constant is obtained from the cross section of electron impact excitation of CO_2 with a threshold of 7 eV, representing the most probable pathway for dissociation via an electronic excited state.[77-80] The look-up table as a function of mean electron energy is generated with Bolsig+, a software program solving the Boltzmann equation for the electrons, using the input collision cross sections from the Phelps database on LXcat.[57, 58] The space- and time-averaged electron impact dissociation rate calculated in this way is plotted in figure 6-11 as a function of the dielectric constant of the packing, for both the mm-gap and microgap reactor.

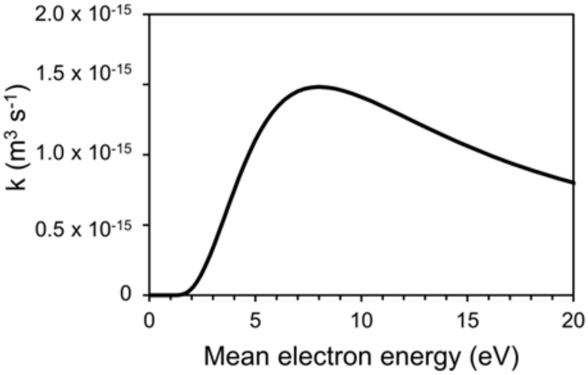

Figure 6-10 Reaction rate constant for the dissociation of CO_2 as a function of mean electron energy.

In the mm-gap reactor, a packing with higher dielectric constant will increase the electric field strength and electron temperature (see figure 6-6(a,b)) and therefore also the electron impact dissociation rate constant, resulting in a rise in the dissociation rate (see figure 6-11). However, above a dielectric constant of 25, the drop in electron density becomes significant (see figure 6-6(c)), and thus, in spite of the increasing rate constant, the CO_2 dissociation rate will slightly drop again. This result does not correlate to the results obtained by Mei et al., who reported an increase in CO_2 conversion when the glass ($\varepsilon = 5$) beads were replaced with $BaTiO_3$ ($\varepsilon = 1000$).[39] The drop in CO_2 dissociation rate in our case is caused by the severe drop in electron density. The conditions studied by Mei et al. are, however, not exactly the same, and it might be that at their conditions, the drop in electron density is not so severe. As no electron densities were reported by Mei et al., it is difficult to know the exact underlying reason. On the other hand, it might also be that our estimation of the CO_2 dissociation rate, as explained above, is too approximate, because it is calculated from discharge parameters for a helium plasma. Moreover, the discharge in our model is considered homogeneous, which is correct for a helium plasma, but in CO_2 it will be a combination of local surface and filamentary discharges. Therefore, we have to be careful with drawing conclusions from this simple estimation. Finally, the model only focuses on the differences in the dielectric constant, while in reality there will be more differences between the $BaTiO_3$ and glass beads, which might explain the higher CO_2 conversion when using the $BaTiO_3$ beads.

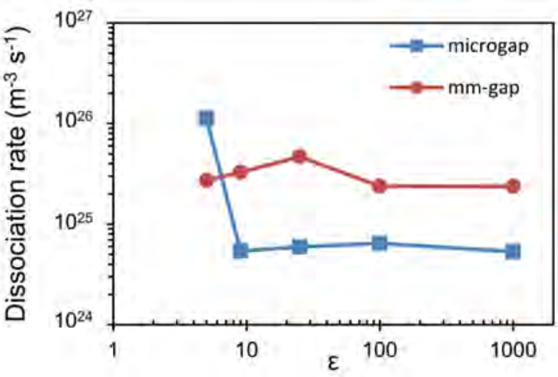

Figure 6-11 Influence of the dielectric constant on the space- and time-averaged electron impact dissociation rate of CO_2, for both the microgap and the mm-gap reactor.

The calculated CO_2 dissociation rate in the microgap reactor follows almost perfectly the trend of the calculated electron density; cf. figure 6-11 and figure 6-6(c). The higher electric field strength and electron temperature when increasing ε from 5 to 9 is too limited to compensate for the strong drop in overall electron density. The resulting dissociation rate therefore drops by a factor 20. Overall, this simplified calculation predicts that the microgap packed bed DBD reactor shows a higher dissociation rate than the mm-gap reactor, in case of glass packing beads (ε = 5). Indeed, at these conditions the electron density is still comparable to the mm-gap reactor, but the mean energy is much higher, giving rise to a higher dissociation rate. For packing materials with higher dielectric constant, the microgap packed bed DBD reactor seems to result in a much lower CO_2 dissociation rate than a mm-gap reactor, due to the significant drop in electron density.

To conclude, our calculations (with these specific input parameters) reveal that using a packing with higher dielectric constant only seems to make sense in a reactor with a large gap. However, our model predicts that even in a mm-gap reactor, after a certain value the beneficial effects of electric field enhancement will be countered by the drop in electron density. In a microgap reactor, the electron density seems to be the most important parameter in determining the CO_2 dissociation rate, so our calculations predict that in this case a packing with lower dielectric constant will be beneficial.

Currently, experimental work is being performed in our group to investigate the CO_2 dissociation in both a mm-gap and microgap reactor for different packing materials, and the first preliminary results seem to indicate similar trends. However, the different packing materials in the experiments do not only have different dielectric constants, but they might also have other characteristics, like the morphology, porosity, and chemical activity (acid-base properties), etc., which can also affect the outcome.[38, 42] Hence, this shows the added value of modelling, where the effect of one separate parameter, i.e., here the dielectric constant, can be investigated.

6.4 Conclusion

We studied the influence of the gap size and the dielectric constant of various packing materials on the plasma characteristics in a packed bed DBD reactor, by means of fluid modelling. A 2D axisymmetric model was developed for both a mm-gap and a microgap packed bed DBD reactor. The plasma behaviour is significantly different for a mm-gap reactor and a microgap reactor, when applying the same potential. Due to the small dimensions, the electric field strength is more enhanced in a microgap reactor, resulting in more current peaks per half cycle, because the electric field strength needed to cause a breakdown, is more often reached. On the other hand, the small dimensions and enhanced electric field in the microgap reactor will cause the plasma to lose its quasi-neutrality, because the electrons get easily lost at the walls and the surface of the packing beads. For the same reason, the ion density is also clearly lower in the microgap reactor than in the mm-gap reactor, and the plasma is not able to flow through the channels between the voids, except for very low dielectric constants.

In both the microgap and mm-gap reactor, using a packing with higher dielectric constant increases the electric field strength, but only up to a certain extent. For the mm-gap reactor the electric field increases up to $\varepsilon = 100$ after which it stagnates. For the microgap reactor, the electric field does not increase anymore above a dielectric constant of 9. Further increasing the dielectric constant will cause the electric field enhancement to take place only at the top part of the reactor, leaving a lower electric field strength near the bottom, where there is less polarisation between the lower bead and the grounded electrode. However, the overall (space- and time-averaged) electric field is not really affected by this behaviour, and stays more or less the same from $\varepsilon = 9$ to 1000.

The effect on the electron temperature is very similar. In the mm-gap reactor an enhanced electric field upon increasing dielectric constant of the packing results in a higher electron temperature. In the microgap reactor the electron temperature also increases but again only up till $\varepsilon = 9$. The slight decrease afterwards is attributed to the fact that the electric field enhancement mainly takes place at the top part of the reactor.

Finally, the electron density follows more or less the opposite trend as the electric field, with a significant drop between $\varepsilon = 5$ and 9 for the microgap reactor, and a similar drop between $\varepsilon = 25$ and 1000 for the mm-gap reactor, which is attributed to a change in discharge mechanism. For the mm-gap reactor, the plasma loses the ability to travel through the channels between the voids when ε rises from 25 to 1000, resulting in an overall lower electron density. The same behaviour takes place in the microgap reactor, but in this case, even at a dielectric constant of 9, the plasma cannot flow through the channels, and only when ε drops to 5, the plasma gains the ability to travel through the gaps, changing the discharge behaviour, and resulting in a much higher overall electron density than for the higher dielectric constants.

By coupling our calculated mean electron energy and electron density values with a look-up table for the reaction rate of electron impact CO_2 dissociation, we predict that for the mm-gap reactor the CO_2 dissociation rate tends to increase with rising dielectric constant of the packing beads, following the trend of the electric field and electron temperature, but above a certain dielectric constant (i.e., $\varepsilon = 25$ for a gap size of 4.5 mm), the beneficial effects of the electric field enhancement will be countered by the drop in electron density. For the microgap reactor, the electron density is obviously the dominant factor. Regardless of the higher electric field strength, the electron impact dissociation rate of CO_2 will drop upon rising dielectric constant of the packing beads from $\varepsilon = 5$ to $\varepsilon = 9$, because of the significant drop in electron density. Therefore, our calculations reveal that using a packing with higher dielectric constant, at these input parameters, only makes sense when the gap is large (in the order of millimetres). In a microgap (less than 1 mm) reactor, a packing with a low dielectric constant seems to give the best results.

Chapter 7

Effect of Bead Size and Dielectric Constant

This chapter is submitted for publication as: K. Van Laer and A. Bogaerts, “How Bead Size and Dielectric Constant Affect the Plasma Behaviour in a Packed Bed Plasma Reactor”, *Plasma Sources Science and Technology,* submitted

7.1 Introduction

In this chapter, we investigate the influence of the size of the packing beads and their dielectric constant on the discharge behaviour, with the gap distance this time kept constant. Indeed, experiments have demonstrated, as mentioned at the end of chapter 2 and demonstrated in chapter 4, that changing the packing size can drastically affect the performance of the application.[40-42] Let us briefly highlight the essentials again. Butterworth et al. studied CO_2 splitting in a PBPR with five different bead sizes for two different bead materials, namely Al_2O_3 and $BaTiO_3$, changing the gas composition from 90/10 Ar/CO_2 to pure CO_2.[40] They concluded that smaller packing beads can significantly increase the CO_2 conversion, given that the applied potential is sufficient to cause a discharge in the void spaces, because a smaller packing also leads to a higher breakdown voltage. However, this only applies when argon is used as carrier gas. With pure CO_2 the benefits of smaller packing beads are mitigated, and even reversed. Michielsen et al. confirmed that for pure CO_2 the largest beads perform the best.[41] However, the results strongly depend on the bead material, with the highest conversions and energy efficiencies being found with $BaTiO_3$. In chapter 4 we experimentally discovered that also the input power can be of great importance. The highest CO_2 conversions and energy efficiencies, in case or zirconia beads, were found using the lowest input power and the largest beads. However, at higher input power, smaller bead sizes had the best results. Lastly, Duan et al. revealed that for a microreactor the smallest packing beads with the highest dielectric constant lead to the highest CO_2 conversion, which in their study were CaO ($\varepsilon \sim 12$) beads. From these experimental studies, it is clear that there is no simple rule regarding the bead size that ensures the best results. As far as the dielectric constant of the beads is concerned, the higher values seem to lead to higher conversions and energy efficiencies in all these studies. However, from the data gathered by Michielsen et al. it is clear that also other material parameters play a role.[41] To aid in the understanding process, modelling is again an excellent tool to help explain the present and future experimental results.

7.2 Modelling Details

The solved equations, plasma chemistry and boundary conditions remain exactly the same as described in chapter 3 and chapter 5, respectively. The geometry, however, is changed, to accommodate for the changing number of packing beads, which is discussed in the following section. The operating pressure remains at 1 atm and the temperature is kept constant at 300 K.

7.2.1 Building the Geometry

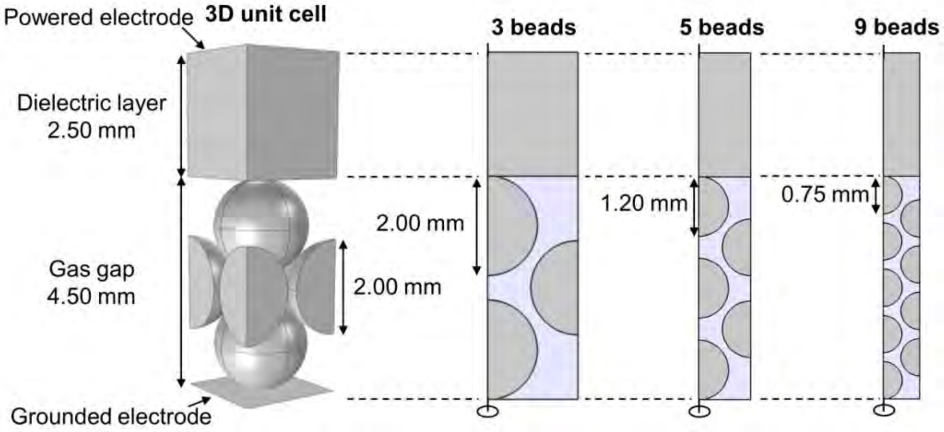

Figure 7-1 3D unit cell of a packed bed reactor, and 2D axisymmetric representations with either 3, 5 or 9 packing beads.

Regarding the geometry we again stick with the "channel of voids" model, following the reasoning in previous chapter. Three different reactor geometries are studied, containing either 3, 5 or 9 packing beads, with a respective diameter of 2.00 mm, 1.20 mm or 0.75 mm (figure 7-1). The gap size stays fixed at 4.50 mm. Only the powered electrode, at the top, is covered with dielectric material (alumina, ε = 9). The bottom electrode is grounded. The different packing beads in the reactor are not touching each other, to account for the void space which is present in the real 3D geometry, while using a 2D model for the sake of computation time. The closest distance between the packing beads is related to their diameter. More specifically, it is equal to the diameter of the sphere enclosed by three touching beads in the same plane, representing the smallest possible opening between the beads in a real 3D close-packed reactor, just like in previous chapter. The dielectric constant of the packing beads will be varied over the same values as in previous chapter, to match different possible packing materials, namely 5 (glass), 9 (alumina), 25 (zirconia), 100 (titania) and 1000 (ferroelectric materials like $BaTiO_3$).

7.3 Results and Discussion

7.3.1 Electric Field Enhancement

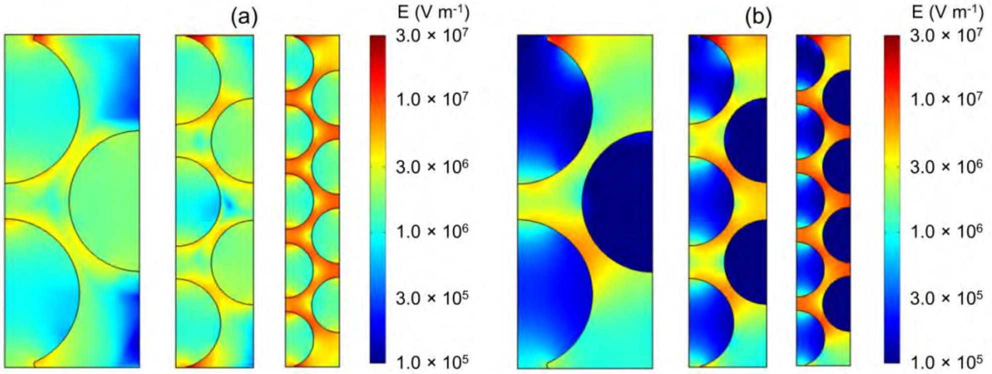

Figure 7-2 Time-averaged electric field strength for the geometry with 3, 5 and 9 beads, with a (a) zirconia packing (ε = 25) and (b) $BaTiO_3$ packing (ε = 1000)

In figure 7-2, we plot the time-averaged electric field strength over one cycle of applied potential (7.5 kV peak-to-peak) for the geometry with 3, 5 and 9 beads, with a zirconia packing (a) and a $BaTiO_3$ packing (b). It is clear that the electric field is enhanced near the contact points between the beads and the top dielectric or bottom electrode, and also in between the beads. As the packing beads get smaller, the enhancement clearly increases.

When comparing figure 7-2(a) and 7-2(b), we can see that, for a DBD reactor with single dielectric layer, at higher dielectric constant of the beads, the electric field enhancement shifts towards the dielectric layer covering the powered electrode, away from the uncovered grounded electrode. The same behaviour was observed in chapter 6. Furthermore, the overall enhancement is also larger for packing beads with a higher dielectric constant. The 2D electron temperature profiles follow the same trend, and are therefore not specifically depicted in this paper. Their space- and time-averaged values will be discussed in section 7.3.3.

7.3.2 Electron Density Profiles

We are most interested in the behaviour of the plasma in the PBPRs, i.e., whether it can spread throughout the gap or stays localized between two beads. This information can be deduced from the time-averaged electron density plots, depicted in figure 7-3.

Looking at the profiles of the 3 beads models (top row) as a function of increasing dielectric constant (from left to right), it is clear that for $\varepsilon = 5$ the electron density is maximum in the gaps between the beads, as if they only distort the plasma profile but do not influence the discharge behaviour. For $\varepsilon = 9$ and 25, the plasma can still pass through the gaps between the beads (the so-called “void channels”), but it shows a higher time-averaged electron density in the voids themselves. For $\varepsilon = 100$ and 1000 the plasma does not show significant electron density in the void channels, indicating that the plasma cannot pass through them anymore. The electron density stays localised in the voids, with lower values.

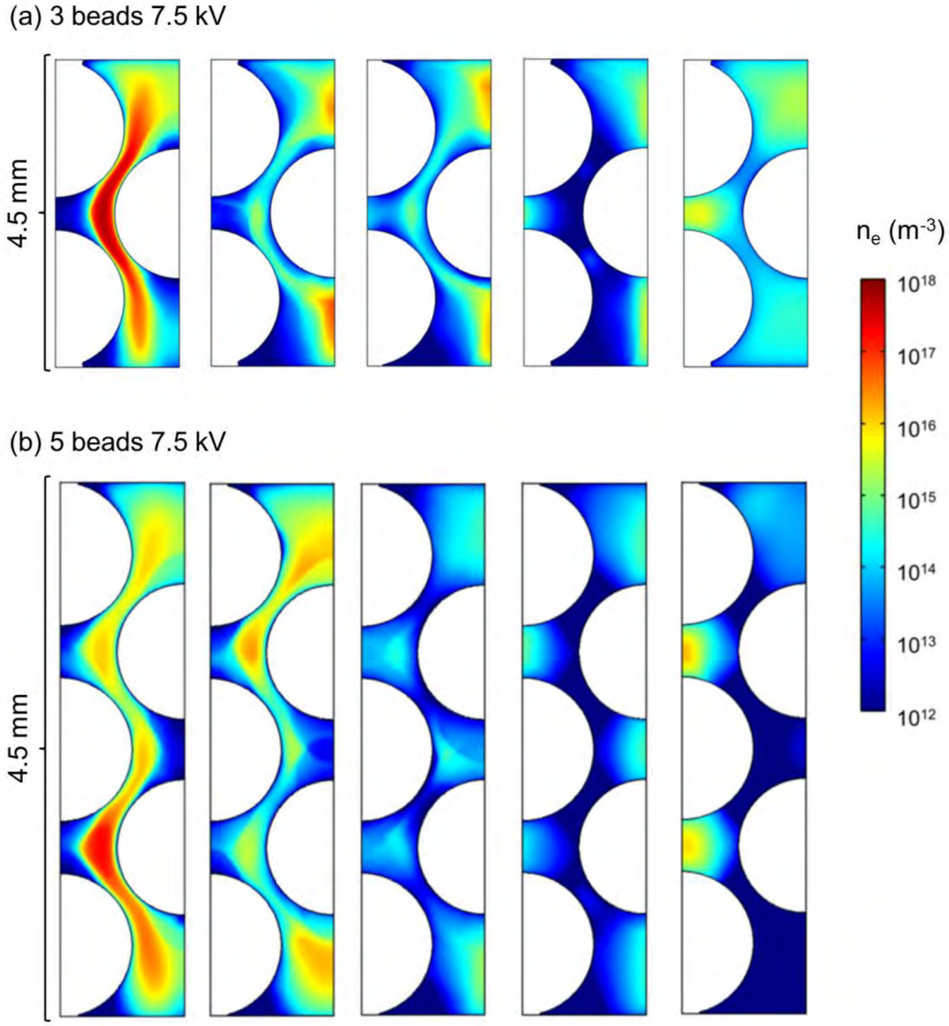
(a) 3 beads 7.5 kV
4.5 mm
(b) 5 beads 7.5 kV
4.5 mm
n_e (m^{-3})
10^{18}
10^{17}
10^{16}
10^{15}
10^{14}
10^{13}
10^{12}

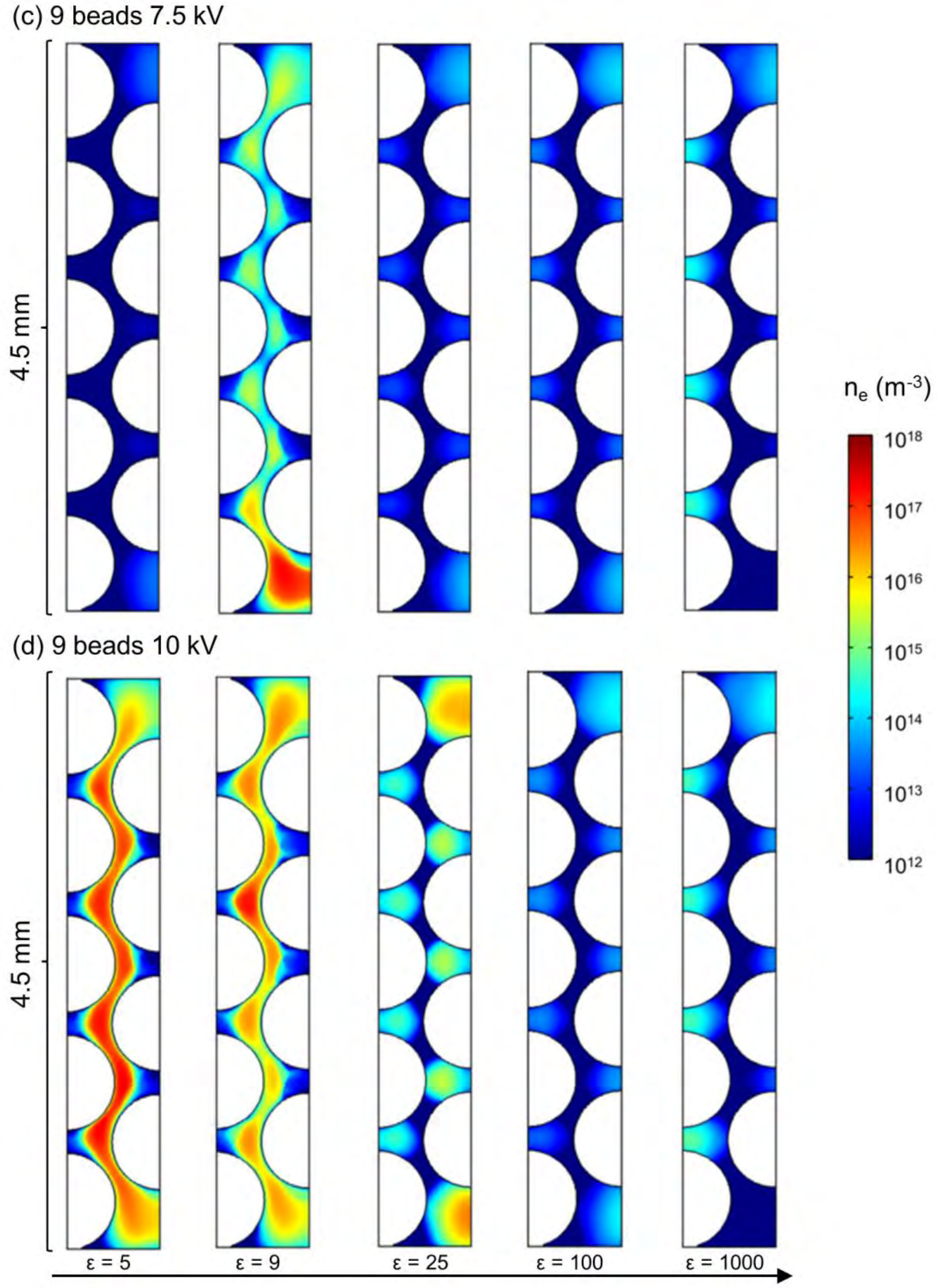

Figure 7-3: Time-averaged electron density profiles for the geometry with 3, 5 and 9 beads, with different dielectric constants. The result with 9 beads is also shown with a higher applied potential of 10 kV peak-to-peak. Note that the different geometries have the same actual gap size, but were enlarged inversely to the decrease in bead size, for the sake of visibility.

For the 5 beads models, the plasma can spread over the full gas gap up to ε = 25, although the maximum electron density clearly drops from 1.8×10^{17} at ε = 5 to 1.0×10^{14} m^{-3} at ε = 25. At ε = 100 and 1000, the electron density profiles show a clear density minimum in the region of the contact points, so the plasma is formed locally in the voids without an exchange of charged species between them, just as in the 3 beads models.

The 9 beads model packed with glass beads (ε = 5) and operated with an applied potential of 7.5 kV peak-to-peak, shows a very low overall electron density. As its electrical current profile will demonstrate below, no discharge is ignited in this setup. When the dielectric constant of the packing material is slightly higher, i.e. ε = 9, a discharge can be formed with significant electron density in the voids as well as in the void channels. At higher dielectric constants, the electron density drops significantly, and the plasma is limited to the voids. In other words, at ε = 25 and higher, the 9 beads model only shows localised, and quite weak, plasma formation at 7.5 kV peak-to-peak.

Because the 9 beads model did not ignite in the case of ε = 5 at the applied potential of 7.5 kV peak-to-peak and a frequency of 23.5 kHz, we also performed calculations at a higher applied potential of 10 kV peak-to-peak. At this higher applied potential, the plasma can clearly be ignited at the lowest dielectric constant, proven by the high electron density (~10^{17} m^{-3}). The discharge takes place again in the full gap, in line with the previous results for the 3 and 5 beads models and the lower dielectric constants. When the dielectric constant of the beads is increased to ε = 9, there is still significant electron density in the void channels, which is the indication of a full gap discharge. Further increasing the dielectric constant limits the electron density to the voids, indicating that from ε = 25 on, the discharge will again be localised.

7.3.3 Electric Current Profiles

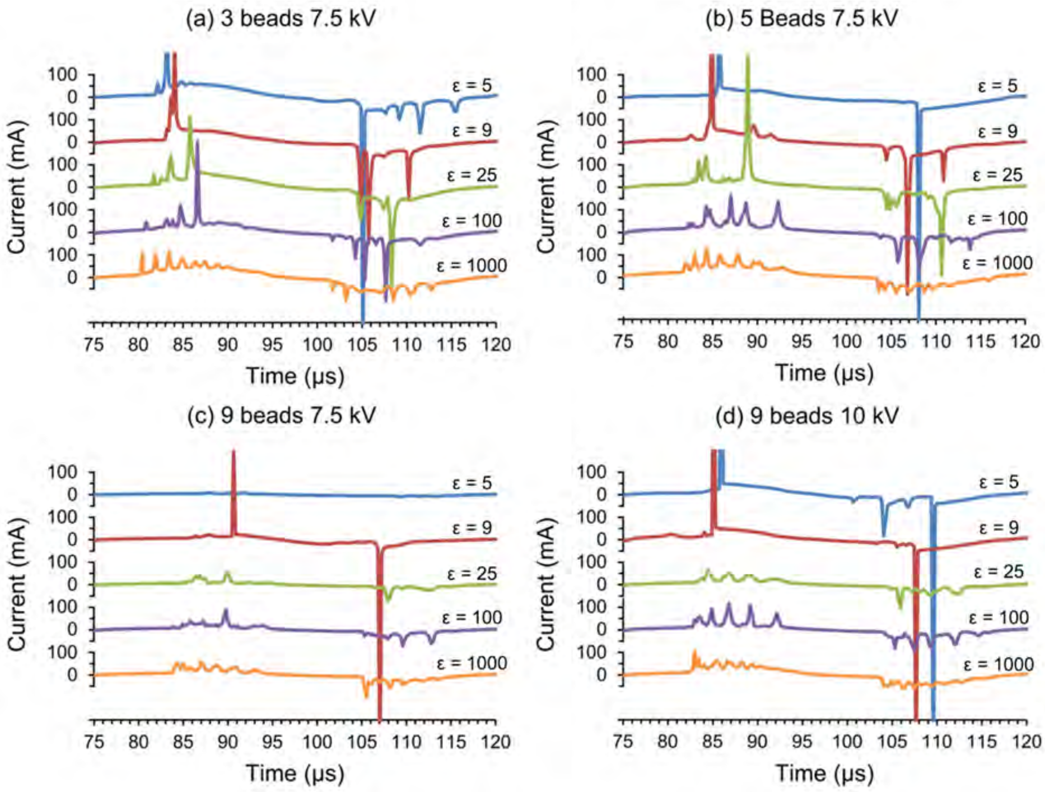

Figure 7-4 Current profiles calculated for the geometry with (a) 3 beads, (b) 5 beads and (c) 9 beads at 7.5 kV peak-to-peak applied potential, as well as (d) 9 beads with 10 kV peak-to-peak, for the different dielectric constants.

We can correlate the time-averaged electron density profiles with the calculated electric current profiles over a full cycle of the applied potential, as illustrated in figure 7-4. To calculate the current, the electrode surface area is needed. In the model this is the size of the circle formed by rotating the grounded electrode around the symmetry axis. However, to make the modelling results representative for a full size reactor, the current values are multiplied with a factor that comprises the ratio between the real electrode surface and the surface of the modelled disk. The value for the real electrode surface area is adopted from the cylindrical DBD reactor as described in chapter 3. Because it is a cylindrical reactor, the average between the inner and outer surface area is taken.

It is clear from figure 7-4 that the current profile can change significantly as a function of dielectric constant, as well as bead size. Furthermore, within one current profile, the positive and negative half cycle can be fairly different as well. This difference is attributed to the fact that the PBPRs under study only have a single dielectric layer, which inherently makes the reactors asymmetrical. The significant change with packing size and dielectric constant, however, is obviously due to a change in discharge behaviour.

From the current profiles, two different types of current peaks can be distinguished, attributed to two types of discharges. The very strong current peaks, with intensity of several 100s to 1000 mA, originate from a discharge that can flow through the void channel covering the full gas gap. The smaller current peaks of a few 10s to 200 mA (and 400 mA in one exceptional occasion) are caused by a series of local discharges, which do not have the ability to cover the full gas gap. Around a few 100 mA, there is an overlap between the two possible discharges, which makes it difficult to unambiguously attribute the current peak to one of both possibilities, without looking at the instantaneous density profiles. This is due to the sampling frequency of the calculation results. During the course of the calculation, the results are written away at a frequency of 1/200 of one cycle of the applied potential. In some cases this frequency is not enough to resolve the full height of the current peak, resulting in lower values of a few 100 mA, where higher values are expected. The calculation time of a single model is in the order of a few weeks. Increasing the sampling frequency will drastically increase the calculation time even further, making it impractical. Therefore we opted to use the above mentioned frequency as a best of both worlds: enough sampling points with a reasonable calculation time. We will now discuss the different current profiles in detail.

For the 3 beads models, strong current peaks are found at all dielectric constants except ε = 1000. At ε = 5, 9 and 25, the strongest current peak is attributed to a full gap discharge, while the other smaller current peaks are caused by local discharges. The order in which they occur can vary. Indeed, at ε = 25, the last current peak is caused by the full gap discharge, as was already described in chapter 5. At lower dielectric constants, the full gap discharge can occur earlier, with the possibility of a few local discharges afterwards.

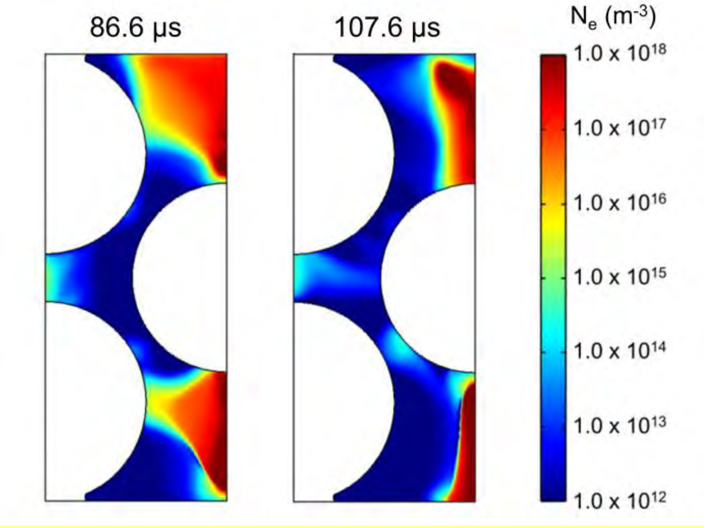

Figure 7-5 Instantaneous electron density profiles of the 3 beads model with ε = 100 packing beads for the largest current peak in the positive (86.6 μs) and negative (107.6 μs) half of the current profile.

The large current peaks at ε = 100 could be expected to also arise from a full gap discharge, but they are not. Looking at the instantaneous electron density profiles at the exact moment of the current peaks, shown in figure 7-5, we can conclude that they are the result of a local discharge taking place above and below the right packing bead in the geometry. This illustrates that the current profiles alone cannot unambiguously give information of a certain discharge behaviour, but the latter can only be done when also studying the plasma density profiles. Hence, this clearly demonstrates the added value of modelling, to obtain detailed insight in the underlying mechanisms. Since the sizes of the void spaces in the 3 beads model are large compared to the models with more packing beads, the generated electrons by the aforementioned discharge can accumulate to higher numbers before hitting a wall, giving rise to a stronger current peak.

At even higher dielectric constant (ε =1000), no discharge can take place anymore at the same time above and below the right packing bead. The electric field enhancement shifts away from the grounded electrode, as mentioned before, restricting the plasma generation to the top part of the reactor, resulting in a larger number of short-lived local discharges, and thus a larger number of smaller current peaks. This observation was also found experimentally by Ohsawa et al., who investigated the discharge characteristics in a parallel plate reactor packed with a disc of fused glass beads.[76] In their study the current profile of the discharge with the smallest packing beads (0.105 – 0.212 mm) showed much more, and smaller, current peaks (~ 0.2 mA) than the current profile with the largest beads (3 mm), which consisted of less but stronger current peaks (~ 10 mA).

The 5 beads model clearly follows the same trend. At ε = 5, 9 and 25, one strong current peak is found per half cycle, attributed to a full gap discharge, and with an increasing number of smaller current peaks upon rising dielectric constant. At ε = 100, no full gap discharge is taking place anymore, and all the smaller current peaks (< 200 mA) arise from local discharges. At ε = 1000, we observe the largest number of current peaks, but they are also the smallest (< 100 mA), again originating from localised discharges.

For the 9 beads model at 7.5 kV peak-to-peak and ε = 5, no discharge can be ignited (see above), explaining the absence of current peaks. Obviously the applied potential is not high enough to cause a breakdown anywhere in the reactor. Indeed, because the dielectric constant of the packing material (ε = 5) is rather low, the electric field enhancement in the reactor between the beads will also be small. However, already at slightly higher dielectric constant, the electric field enhancement will be larger, which explains why at $\varepsilon = 9$ a discharge can be formed. It is a full gap discharge, with one large current peak each half cycle. At $\varepsilon = 25$, no full gap discharge can be formed anymore, illustrated by the larger number of smaller current peaks, caused by local discharges. The smaller bead size in combination with the higher dielectric constant enhances the electric field near the contact points, so that the electrons are accelerated more towards the bead walls, and not being able to pass through the void channel anymore. Increasing the dielectric constant further does not change the plasma characteristics very much, as is obvious from the current profiles in figure 7-4.

When the applied potential is increased to 10 kV peak-to-peak, the plasma can clearly be ignited at the lowest dielectric constant, enforcing the statement that the size of the packing beads as well as their dielectric constant both have an influence on the breakdown voltage (see below). The discharge takes place again over the full gap, as expected for this low dielectric constants. At $\varepsilon = 9$ it is still a full gap discharge, but in contrast to the results at the lower applied potential, a few minor current peaks pop up before the large current peak. At $\varepsilon = 25$ and higher, the intensity of the current peaks drops, while the number of peaks rises, indicative for the current profile of localised plasma formation.

The fact that a lower dielectric constant requires a higher breakdown voltage corresponds well with experiments performed by Butterworth et al., who reported that the use of $BaTiO_3$ ($\varepsilon = 1000$ and higher) as packing material could lead to plasma formation at an applied potential of 10 kV peak-to-peak, while the minimum required potential for alumina packing ($\varepsilon = 9$) was 16 kV peak-to-peak.[42]

7.3.4 Summarizing Results

Figure 7-6 summarizes the influence of the dielectric constant on the three key plasma parameters, namely the electric field strength, electron temperature and electron density. The values are averaged in time over one cycle of the applied potential, and in space, over the entire reactor geometry.

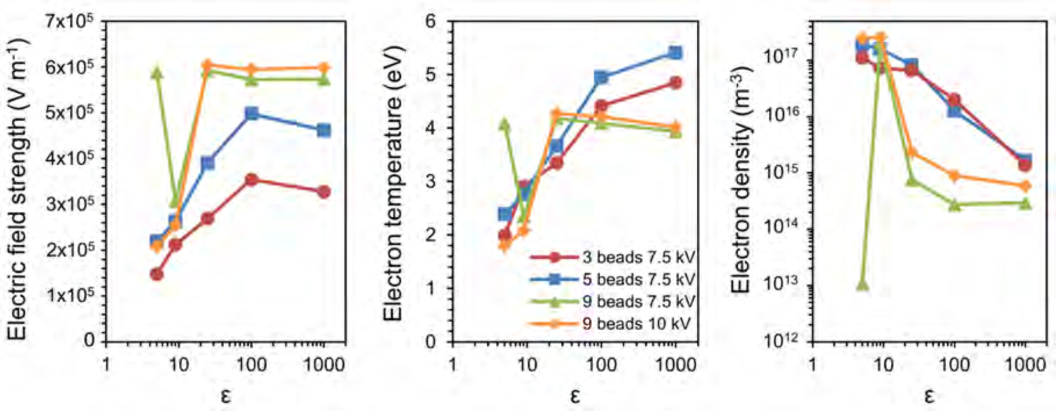

Figure 7-6 Influence of the dielectric constant on the space- and time-averaged electric field strength, electron temperature and electron density, for the geometry with 3 beads, 5 beads and 9 beads (both at 7.5 and 10 kV peak-to-peak).

As illustrated in figure 7-2 above, the electric field strength increases with increasing dielectric constant of the packing beads. Indeed, a higher dielectric constant will lead to stronger polarization of the dielectric material and therefore a greater difference between close-by opposite charges in the vicinity of the contact points between the dielectric objects. The enhancement of the electric field strength was experimentally proven by Mei et al., showing a clear increase when switching from a glass to a $BaTiO_3$ packing of similar size.[42] However, at a certain dielectric constant, the enhancement stagnates, as appears from figure 7-6. In literature, this phenomenon was first reported by Chen et al., based on calculations with the spherical void model of Takaki et al.[27, 44] In their study the electric field enhancement stagnated around a dielectric constant of 100. Our 3 beads and 5 beads model follow the same trend, with a maximum electric field enhancement at ε = 100. When the packing beads are smaller (i.e. in the 9 beads model), the saturation in electric field enhancement happens already at ε = 25. Furthermore, a smaller packing also implies a higher overall electric field strength. The maximum electric field strength is indeed almost a factor 2 higher for the 9 beads model (0.75 mm diameter) compared to the 3 beads model (2.00 mm diameter). Note that the results for the 9 beads model operated at 7.5 kV peak-to-peak with a glass packing (ε = 5) show an exceptionally high electric field (and a very low electron density; see below), since this set-up does not exhibit plasma formation, as mentioned before. The applied potential is indeed too low to cause a discharge, and therefore the electric field is always high, because it is never distorted or lowered by the presence of plasma.

The electron temperature roughly follows the same trend as the electric field strength, with an increase in overall value upon rising dielectric constant. The saturation observed for the electric field in the geometry with 3 and 5 beads is also partially reflected in the electron temperature, although the value still rises above ε = 100. For the 9 beads model, the stagnation appears at exactly the same dielectric constant, namely ε = 25. On the other hand, the effect of bead size is clearly different for the electron temperature and the electric field strength. Decreasing the bead diameter from 2.00 mm (3 beads) to 1.20 mm (5 beads) increases the electron temperature, especially at higher dielectric constants, just like for the electric field strength. Smaller packing beads with diameter of 0.75 mm, however, do not lead to a further increase in overall electron temperature as they do with the electric field strength. This is probably related to the low electron density in the 9 beads model for ε = 25 or above (see below).

The time- and space-averaged electron density clearly drops upon rising dielectric constant of the packing, as could also be deduced from figure 7-3 above. For the 3 and 5 beads model, the electron density decreases only slightly between ε = 5 and 25, but afterwards it drops by several orders of magnitude. For the 9 beads models, the electron density drops two orders of magnitude above ε = 9, but afterwards it only slightly decreases between ε = 25 and 1000. This drop can be explained as follows. As the electric field strength increases, the electrons can move faster, which will increase their loss rate at the walls, resulting in a lower overall electron density. Reducing the size of the packing beads has the same effect on this loss rate. Indeed, the walls are closer to each other, so the electrons will hit the walls faster, again leading to lower electron densities. Note that the first data point (ε = 5) of the 9 beads model with 7.5 kV applied potential peak-to-peak is very low, since no plasma is formed.

When comparing the results for the different bead sizes, we can conclude that at low dielectric constants, the electric field strength, electron temperature and density in case of 3 beads, 5 beads and 9 beads are all close to each other. This can be explained by the type of discharge taking place. As shown in figure 3 above, at low dielectric constant, the plasma does not exist locally, but can flow through the void channels over the full gap of the reactor. This so-called full gap discharge takes place regardless of the size of the packing beads, as long as the dielectric constant is low enough (i.e. up to 25, depending on the bead size), and it is not heavily affected by the presence of the packing beads.. On the other hand, at higher dielectric constants, the discharges become localised, and they are fully defined by the packing, so the plasma parameters will be very different for different bead sizes.

To summarise, when the dielectric constant increases, the electric field is more enhanced, leading to more energetic electrons, i.e. a higher electron temperature, resulting in more electron dissipation at the walls, and thus a lower electron density. Decreasing the size of the packing beads leads to a higher electric field strength, but as a consequence, also to a lower electron density.

These model predictions are very useful for a better insight in the experimental work with PBPRs to help clarify the experimentally observed trends in e.g. CO_2 conversion and energy efficiency as a function of bead size and dielectric constant. It is important to remember that the combination of both an enhanced electric field with a sufficient electron density would be necessary to improve the experimental performance. This is quite challenging because a higher electric field strength is usually accompanied by a lower electron density (figure 7-6). Michielsen et al. found the best CO_2 conversions and efficiencies with a $BaTiO_3$ packing with the largest bead size.[41] $BaTiO_3$ has the highest dielectric constant and thus the most enhanced electric field compared to the other tested materials, although the electron density is lower. On the other hand, the best performing bead size was the largest, meaning that the electric field strength will not be enhanced even further, but in return, the electron density will remain relatively high. In other words, large beads with a high dielectric constant seem to give the best combination between enhancement of the electric field strength and reasonable electron density, in good agreement with our model predictions (see figure 7-6). Exactly the same explanation can be given for the results of Butterworth et al. with 100% CO_2, where $BaTiO_3$ provided the best results when the bead size was the largest.[40] In our own experimental results presented in chapter 4, the highest CO_2 conversions were also found with the largest packing beads, provided that the input power is not too high (60 W). However, at the highest input power (100 W), the smaller beads perform better. This can also be explained based on our modelling results. One would expect that at higher input power, the largest beads perform better, because the electron density will still be high enough, as the loss rates at the bead surfaces are expected to decrease upon larger beads. However, in this case, the breakdown voltage plays a role, because in the reactor packed with smaller beads at lower input power, the breakdown voltage is less often met (see figure 7-3), resulting in a lower discharge rate and conversion compared to a reactor with larger beads (and thus a lower breakdown voltage). At higher input power, the breakdown voltage is more often met in the smaller beads reactor, resulting in a significantly higher conversion, while the change for the larger beads can be less significant. Finally, Duan et al. reported that the highest dielectric constant (only $\varepsilon \sim 12$) resulted in the best performance, as expected. However, in their study, the smallest beads (0.18 – 0.25 mm) performed better. The explanation lies in the fact that the diameter of the largest beads (0.25 – 0.42 mm) was around half the size of the gas gap (0.6 mm). A lot of open space exists in the gas gap when the bead size can exceed half the height of the gas gap. The number of contact points, where the electric field strength will be enhanced, is thus much lower, lowering the overall electric field enhancement significantly, and therefore resulting in lower CO_2 conversions. In this case, the ideal size of the packing beads is therefore not simply the largest one, but the largest without disturbing the ability to form a close packed system.

7.4 Conclusion

We studied the effect of bead size and dielectric constant on the plasma behaviour in a packed bed DBD reactor by means of a fluid model. Our calculations illustrate that the plasma behaviour can change significantly when changing these parameters. At low dielectric constant of the packing beads, the plasma is always a so-called "full gap" discharge, irrespective of the bead size, i.e., the plasma is spread out over the full gas gap, showing significant density in the voids as well as in the connecting void channels. The electric current profile shows one (or two) strong current peaks per half cycle, attributed to the full gap discharge, the electron density is relatively high, while the electric field strength and electron temperature are rather low.

When the dielectric constant increases, the electric field enhancement at the contact points (or the position of smallest void channel) is so high that the electrons are accelerated to the walls of the beads, rather than having the ability to flow through the void channel. The plasma can no longer extend from one void to a neighbouring void and it becomes localised. The current profile will change from one large peak per half cycle to a lot of smaller peaks, each arising from an individual local discharge somewhere in the reactor. The time-averaged electric field strength is higher, as mentioned above, leading to a higher electron temperature, but a lower electron density, because the electrons get lost more easily at the walls. At larger bead sizes, the shift from full gap discharge to localised discharges will occur at a higher dielectric constant, which is logical, because of the larger voids in between the larger beads. Finally, smaller bead sizes or a lower dielectric constant of the beads will require a higher breakdown voltage, which corresponds well with experimental results. These model predictions help to clarify the experimentally observed trends, providing us with a better insight in the experimental work with PBPRs.

Chapter 8

Streamer Movement Through the Packing

8.1 Introduction

In the previous three chapters we studied helium plasma in a packed bed DBD reactor geometry to get a better idea about the way it is formed and how it behaves with a packing present in the reactor. Furthermore, we studied the influence of the gap size, the bead size and the dielectric constant of the packing material. However, the environmental applications of interest, in particular the splitting of CO_2, are operated with molecular gases, which in general lack the ability to form a homogeneous discharge across the gas gap, but rather show a combination of streamer and surface discharges.[48, 56] In the present chapter we therefore want to make the first step in studying more complex molecular gases. We are interested in the behaviour of the inevitably formed streamer when it hits the packing material in the PBPR. For this study we switch from helium to dry air, and not directly to CO_2 in which we are most interested, because of two reasons. The first reason is that dry air, which is a mixture of N_2 and O_2, still has a relatively small reaction set. Furthermore, to correctly simulate the propagation of the streamer, photoionization needs to be included. For dry air this process is well described in literature, which is the second reason why we focus on dry air.[81, 82]

Streamer propagation has been extensively studied in the past.[24, 47, 48, 83-87] A few of these studies can be linked to plasma formation in a PBPR, as they discuss the influence of objects in the path of the streamer. Babaeva et al. performed a few studies on the interaction of plasma filaments with objects blocking its path, such as dust particles.[47, 84, 85] Kruszelnicki et al. studied the interaction of a negative electrical discharge with a 2D packed bed configuration of quartz rods, which shows similarities to what we want to model.[48]

The goal in this chapter is to discover how an existing streamer behaves when it reaches packing beads, blocking its pathway towards the electrode. In order to do so, we had to adjust the previous model.

8.2 Modelling Details

The model in this chapter is based on the model described and used in previous chapters. It again solves the same equations as described in chapter 3. However, to correctly describe the propagation of a streamer, photoionization needs to be included. For this purpose, we introduce three Helmholtz differential equations. The approach is discussed below. Furthermore, the reactor geometry is also slightly adjusted to fit our needs. Because we are interested in the behaviour of a single streamer, we do not need to model multiple cycles of applied potential, which is very time-consuming. Instead, a few tens of nanoseconds is enough to cover the average lifetime of a plasma streamer in a DBD reactor. The streamer is artificially initiated just beneath the dielectric layer covering the powered electrode, by artificially increasing the density of electrons locally. The top electrode does no longer cycle through a sine wave of applied potential, as in previous chapters. Instead, in this short time span, we apply a constant voltage of -10 kV, forcing the (negative) streamer downwards. The packing beads are made of glass ($\varepsilon = 5$).

8.2.1 Building the Geometry

The geometry used in this chapter is based on the base case geometry of our previous PBPR research (see chapter 5), although there are some differences. First of all, because we want to model the streamer interfering with the packing, we removed the top packing bead, to give the streamer enough room to fully develop before hitting the surface of the packing bead. Second, we switched the position of the packing beads, placing the middle bead on the side of the symmetry axis, and the bottom bead on the other side. This way we can make use of the symmetry axis, because now the streamer can be initiated directly above the middle bead on the symmetry axis. Furthermore, we increased the width of the reactor to include the full diameter of the bottom bead, as well as some extra space at the right of it, to allow the streamer to develop in whichever way desired. This geometry is show in figure 8-1.

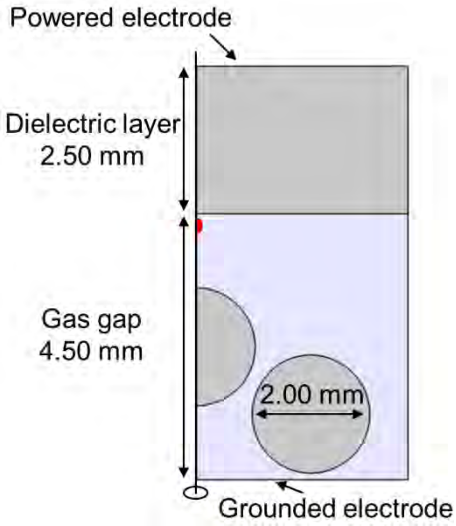

Figure 8-1 2D axisymmetric reactor geometry used in this model. The red dot indicates the location of initial enhanced electron density.

8.2.2 Description of Photoionization

To correctly calculate the propagation of the streamer, we need to include extra equations to account for photoionization. In N_2-O_2 mixtures, photoionization occurs when O_2 molecules absorb photons, which are emitted as a result of the quenching of highly excited N_2 molecules from the singlet states $b^1\Pi$, $b'^1\Sigma_u^+$ and $c'_4{}^1\Sigma_u^+$ (in the following equations lumped together as state "u").[88] Classically, the rate of this process would be calculated using an integral radiation transfer model, such as the model of Zheleznyak et al.[89]

$$S_{ph}(r) = \iiint_{V'} \frac{I(r)g(r)}{4\pi r^2} dV'$$

This expression shows that the photoionization rate $S_{ph}(r)$ as a function of the position vector r, equals the volume integral of the product of the rate of emission of photons, I(r), with g(r), which is a function of the photon absorption rate by O_2. However, this method is computationally quite expensive. In 2007, Luque et al. proposed a novel approach, allowing to effectively replace the classical integral model by a set of Helmholtz differential equations, significantly simplifying the solution process.[82] The photoionization rate can then be represented as the sum of a number of solutions of Helmholtz equations:

$$S_{ph}(r) = \sum_j S_{ph}^j(r)$$

with terms:

$$S_{ph}^j(r) = \iiint_{V'} \frac{I(r) A_j p_{O_2}^2 e^{-\lambda_j p_{O_2} r}}{4\pi r} dV'$$

In these equations, j stands for the total number of Helmholtz equations (see below), p_{O_2} stands for the partial pressure of O_2 in the gas mixture and A_j and λ_j are fitting parameters, defined against the integral model of Zhelznyak. The Helmholtz equations themselves, which represent the actual problem of radiation transport in a gas, are then defined as follows:

$$\nabla^2 S_{ph}^j(r) - \left(\lambda_j p_{O_2}\right)^2 S_{ph}^j(r) = -A_j p_{O_2}^2 I(r)$$

The aforementioned I(r), the emission rate of photons, is given by:

$$I(r) = \frac{p_q}{p + p_q} \xi \nu_u n_e S_i(r)$$

In this expression, $p_q/(p+p_q)$ accounts for the probability of quenching, i.e. the nonradiative deexcitation of the excited stated of N_2 after collision with another molecule, in which p is the gas pressure and p_q the quenching pressure of the excited states (here indicated as lumped state “u”), ξ stands for the photoionization efficiency, v_u is the electron impact excitation frequency for states u, n_e is the electron number density and $S_i(r)$ the electron impact ionization rate.

From comparison between the expression of $S_{ph}(r)$ by Zheleznyak et al. and by Luque et al., it is clear that:

$$\frac{g(r)}{p_{O_2}} = (p_{O_2} r) \sum_j A_j e^{-\lambda_j p_{O_2} r}$$

To retrieve the fitting parameters A_j and λ_j, the function $g(r)/p_{O_2}$ is fitted against a number of exponents (j) multiplied by $p_{O_2}r$. This number of exponents can change depending on the pressure range of the fit. For atmospheric pressures, a minimum of 3 is required. This number thus defines the number of Helmholtz equations to be solved (see above). The values for the fitting parameters, A_j and λ_j, are taken from the paper of Bourdon et al., in which this three exponential fit is performed, resulting in the fitting parameters shown in table 8-1.[81] The summation of the solutions of the three Helmholtz differential equations, using these three pairs of parameters, gives the total reaction rate for photoionization of O_2, which is included in the model, as explained in next section.

Table 8-1 Fitting parameters of the three exponential fit, by Bourdon et al.[81]

j	A_j (cm^{-2} $Torr^{-2}$)	λ_j (cm^{-1} $Torr^{-1}$)
1	1.986×10^{-4}	0.0553
2	0.0051	0.1460
3	0.4886	0.89

8.2.3 Plasma Chemistry

In this chapter we consider dry air as discharge gas, i.e., a mixture of 80% N_2 and 20% O_2. The plasma chemistry set contains 15 different species, namely molecular N_2 and O_2, atomic N and O, N_2^+,

O_2^+ and O^+ ions, four N_2 electronically excited states (N_2 ($A^3\Sigma$), N_2 ($B^3\Pi$), N_2 ($C^3\Pi$) and N_2 (a'$^1\Sigma$), for simplicity denoted below as N_2A, N_2B, N_2C and N_2a1, respectively), one excited state of atomic O (O^1D), as well as NO, O_3 and the electrons. These species react with each other in 41 different reactions, shown in table 8-2. The set was put together by Poggie et al., who reduced a full air plasma chemistry set, containing 46 species and 395 reactions, to this set, by means of a sensitivity analysis.[90] As can be seen in table 8-2, no vibrational excitation by electron impact was included, since its energy fraction load is very small when electric fields are high, which is the case in a PBPR.

Table 8-2 Dry air reaction set used in the model, with rate coefficients, and references where the data is adopted from. The electron impact reactions are described by energy dependent cross sections. T_e' is the electron temperature in K and T_g' the gas temperature in K. Reactions R25 and R30 stand for radiative decay, described by an Einstein transition probability, instead of a rate coefficient. In R39 and R40, M stands for any third body.

Nr.	Reaction	Rate coefficient	Ref
R1	$e + N_2 \rightarrow e + N_2$	cross-section	91
R2	$e + O_2 \rightarrow e + O_2$	cross-section	91
R3	$e + N_2 \rightarrow N_2^+ + 2e$	cross-section	91
R4	$e + O_2 \rightarrow O_2^+ + 2e$	cross-section	91
R5	$e + N_2 \rightarrow e + N_2A$	cross-section	91
R6	$e + N_2 \rightarrow e + N_2B$	cross-section	91
R7	$e + N_2 \rightarrow e + N_2C$	cross-section	91
R8	$e + N_2 \rightarrow e + N_2a1$	cross-section	91
R9	$e + N_2 \rightarrow e + N + N$	cross-section	91
R10	$e + O_2 \rightarrow e + O + O$	cross-section	91
R11	$e + O_2 \rightarrow e + O + O^1D$	cross-section	91
R12	$N + O_2 \rightarrow NO + O$	$1.10 \times 10^{-20}\ T_g'\ e^{-3150/Tg}\ m^3\ s^{-1}$	90
R13	$N + NO \rightarrow N_2 + O$	$1.05 \times 10^{-18}\ (T_g')^{-0.5}\ m^3\ s^{-1}$	90
R14	$O + O_3 \rightarrow O_2 + O_2$	$2.00 \times 10^{-17}\ e^{-2300/Tg'}\ m^3\ s^{-1}$	90
R15	$O + O + N_2 \rightarrow O_2 + N_2$	$2.76 \times 10^{-46}\ e^{-720/Tg'}\ m^6\ s^{-1}$	90
R16	$O + O + O_2 \rightarrow O_2 + O_2$	$2.45 \times 10^{-43}\ T_g'^{-0.63}\ m^6\ s^{-1}$	90
R17	$O + O_2 + N_2 \rightarrow O_3 + N_2$	$5.58 \times 10^{-41}\ T_g'^{-2}\ m^6\ s^{-1}$	90
R18	$O + O_2 + O_2 \rightarrow O_3 + O_2$	$8.61 \times 10^{-43}\ T_g'^{-1.25}\ m^6\ s^{-1}$	90
R19	$N_2A + O_2 \rightarrow N_2 + O + O$	$1.70 \times 10^{-18}\ m^3\ s^{-1}$	90

R20	$N_2A + O_2 \rightarrow N_2 + O_2$	7.50×10^{-19} m^3 s^{-1}	90
R21	$N_2A + O \rightarrow N_2 + O^1D$	3.00×10^{-17} m^3 s^{-1}	90
R22	$N_2A + N_2A \rightarrow N_2 + N_2B$	7.70×10^{-17} m^3 s^{-1}	90
R23	$N_2A + N_2A \rightarrow N_2 + N_2C$	1.60×10^{-16} m^3 s^{-1}	90
R24	$N_2B + N_2 \rightarrow N_2A + N_2$	3.00×10^{-17} m^3 s^{-1}	90
R25	$N_2B \rightarrow N_2A + hv$	1.50×10^{5} s^{-1}	90
R26	$N_2B + O_2 \rightarrow N_2 + O + O$	3.00×10^{-16} m^3 s^{-1}	90
R27	$N_2a1 + N_2 \rightarrow N_2 + N_2$	2.00×10^{-19} m^3 s^{-1}	90
R28	$N_2a1 + O_2 \rightarrow N_2 + O + O^1D$	2.81×10^{-17} m^3 s^{-1}	90
R29	$N_2C + N_2 \rightarrow N_2B + N_2$	1.00×10^{-17} m^3 s^{-1}	90
R30	$N_2C \rightarrow N_2B + hv$	3.00×10^{7} s^{-1}	90
R31	$N_2C + O_2 \rightarrow N_2A + O + O$	3.01×10^{-16} m^3 s^{-1}	90
R32	$O^1D + N_2 \rightarrow O + N_2$	2.57×10^{-17} m^3 s^{-1}	90
R33	$O^1D + O_2 \rightarrow O + O_2$	4.00×10^{-17} m^3 s^{-1}	90
R34	$N_2^+ + O_2 \rightarrow N_2 + O_2^+$	6.00×10^{-17} m^3 s^{-1}	90
R35	$e + N_2^+ \rightarrow N + N$	$8.31 \times 10^{-12} (T_e')^{-0.5}$ m^3 s^{-1}	90
R36	$e + O_2^+ \rightarrow O + O$	$5.99 \times 10^{-11} (T_e')^{-1}$ m^3 s^{-1}	90
R37	$e + e + N_2^+ \rightarrow N_2 + e$	$1.40 \times 10^{-20} (T_e')^{-4.5}$ m^6 s^{-1}	90
R38	$e + e + O_2^+ \rightarrow O_2 + e$	$1.40 \times 10^{-20} (T_e')^{-4.5}$ m^6 s^{-1}	90
R39	$e + N_2^+ + M \rightarrow N_2 + M$	$3.21 \times 10^{-35} (T_e')^{-1.5}$ m^6 s^{-1}	90
R40	$e + O_2^+ + M \rightarrow O_2 + M$	$3.21 \times 10^{-35} (T_e')^{-1.5}$ m^6 s^{-1}	90
R41	$O_2 + hv \rightarrow e + O_2^+$	S_{ph}	81, 82

The rates of the first eleven reactions (R1-R11) are obtained by Bolsig+, a software program that solves the Boltzmann equation for the electrons, using the collision cross-sections from the LXcat database, to generate the electron impact reaction rates as a function of the mean electron energy.[60, 91] It also calculates the transport coefficients of the electrons as a function of mean energy. The reaction rate coefficients of the other reactions (except R41), namely the chemical reactions between neutral species, electron-ion recombination reactions and radiative decay from the excited species (R25, R30), are taken from literature.[90] Some of these expressions contain the electron temperature or gas temperature. The reaction rate of the last reaction, i.e., photoionization (R41), is calculated from the Helmholtz differential equations, as explained in previous section. Finally, the transport coefficients of all the different species, i.e. the mobilities and diffusion coefficients, are adopted from literature.[92, 93]

8.2.4 Boundary Conditions of the Model

The boundary conditions applied in the dry air model, are very similar to the ones described in chapter 5 for the helium model. Only the surface reactions are different, because of the difference in discharge gas. The surface reactions included are the quenching of excited species (i.e., N_2A, N_2B, N_2C, N_2a1 and O^1D) and the neutralization of the ions (N_2^+, O_2^+ and O^+) to their respective ground state molecule or atom. Upon neutralization, the ions have a probability of 0.05 to emit a secondary electron with an energy of 5 eV.

8.3 Results and Discussion

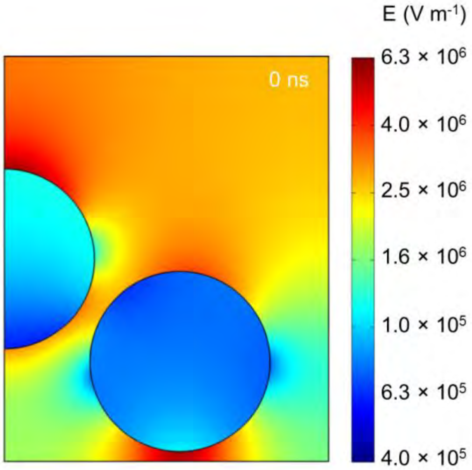

Figure 8-2 Electric field distribution at the beginning of the simulation (0 ns).

At the beginning of the simulation, when plasma is not yet formed, we can clearly observe the influence of the dielectric beads on the electric field, which is induced by the applied potential. Indeed, as is clear from figure 8-2, the electric field strength is enhanced at the poles (top and bottom in this configuration), while electric field minima are formed in the middle, left and right of the beads, due to polarization of the dielectric beads. Where the beads are closest to each other, opposite charges are close, increasing the electric field at these positions. This electric field distribution will have its influence on the propagation of the streamer, as presented below.

In figure 8-3 the evolution of the electron density is shown, over a simulated time of 16 ns. In the beginning only a slight maximum density (barely visible at the colour scale of the figure) can be found right at the top of the gas gap beneath the powered electrode (i.e., cathode) covering the dielectric layer (not shown), which arises from the artificially enhanced initial electron density. In the next frame the electrons are moving downward. A slight increase in electron density can also be seen above the upper packing bead. This increase is caused by the enhanced electric field strength (see figure 8-2), which increases the ionization rate at the surface of the upper bead. In the next two frames (3 and 4 ns), the streamer reaches the surface of the upper dielectric bead. What happens next is a so-called positive restrike. It is a positive streamer that is launched from the dielectric bead surface upward to the cathode. In the next frames (5 – 11 ns) we can see how the positive streamer reaches the dielectric material covering the cathode, after which the discharge spreads out horizontally over the dielectric surface, as a result of the so-called surface ionization wave.[94] The space charge that accumulates at the dielectric material covering the cathode locally lowers the electric field strength. This results in lateral strong electric field differences at the surface of the dielectric material, between the plasma region and the neutral gas region directly next to it. This difference initiates a surface ionization wave, which slowly expands the surface discharge over the dielectric layer (6-11 ns).

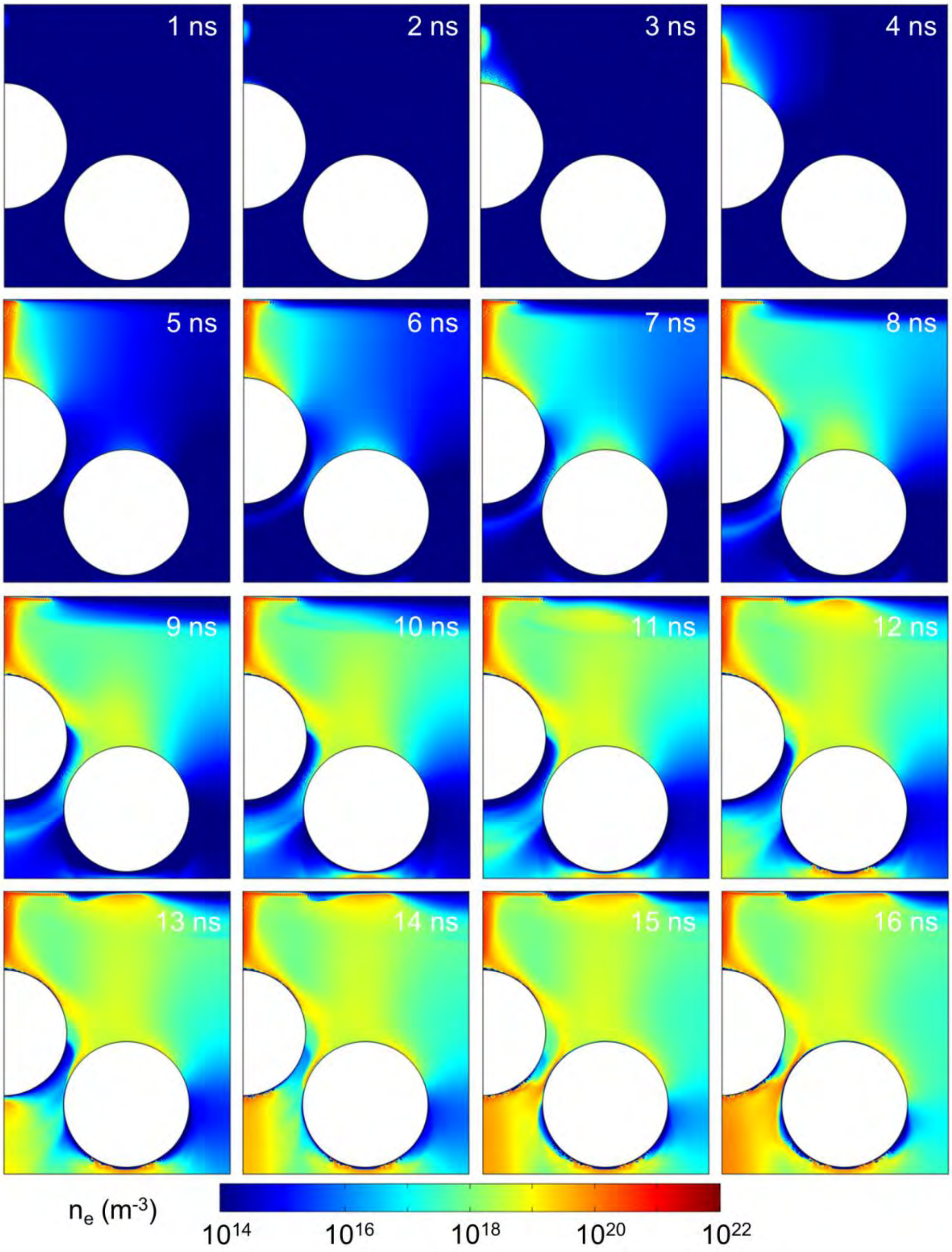

Figure 8-3 Evolution of the electron density distribution over 16 ns.

On the other side, the incoming electrons charge the bead surface, again resulting in a lowering of the local electric field, increasing the difference between the top of the bead and the bead surface in its direct vicinity. This also results in a surface ionization wave on the bead surface. The streamer has now converted to what is called a standing filamentary microdischarge.[48, 94] The filament shows the typical structure of a DBD microdischarge, namely a relatively narrow column of plasma between dielectric materials, with on either surface wider “feet” of plasma (see figure 8-3; 10 ns).

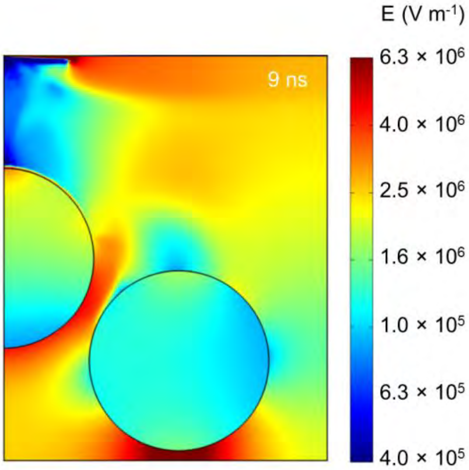

Figure 8-4 Electric field distribution after 9 ns.

As mentioned before, without the influence of plasma, the electric field is enhanced at the top of the packing beads. This also counts for the lower dielectric bead on the right. As a result, the ionization rate is slightly enhanced locally at the top of this bead. With seed electrons coming from photoionization, some discharge can be formed on the surface of this lower dielectric bead. From 7 to 9 ns, the surface discharge on the top dielectric bead on the left can link with this local discharge on top of the right lower bead, further spreading the plasma from the left bead to the top surface of the right bead. The plasma density directly above the lower bead will now also increase in the direction of the upper dielectric layer, due to drift of the ions.

At around 12 ns this results in increased space charge in the dielectric layer directly above the lower packing bead.

Due to the presence of conductive plasma in the upper region of the reactor, the largest potential difference is now found in the lower region of the reactor. As a result, the electric field strength after 8-9 ns is much stronger in the bottom part of the reactor, as is obvious from figure 8-4. Between the lower grounded electrode and the right bead, the electric field strength becomes high enough to cause a discharge, resulting in the visual plasma density in this region after 10 ns (see figure 8-3). The increased electric field strength, however, also causes an ionization wave to be sent out from the bottom surface of the left bead. Between 8 and 12 ns it propagates away from the bead surface towards the grounded electrode. When it hits the electrode, a positive restrike is again formed, going upwards towards the bottom surface of the left packing bead, much like the behaviour of the initial streamer. When it reaches the bottom surface of the left bead, at around 14 ns, a surface ionization wave is again formed on the bottom of the left bead. In between the two packing beads, where the electric field is enhanced in a packed bed reactor, the surface ionization wave can now jump towards the adjacent bead surface, and propagate further over its surface. The resulting discharge between the two packing beads can now also be seen as a local filamentary microdischarge, comparable to the earlier formed filament, but over a smaller distance (see 16 ns in figure 8-3). The transition from the typical filamentary discharge in a non-packed DBD reactor to a combination of local microdischarges and surface discharges as a result of the introduced packing material, was also reported by Tu et al. in a TiO_2 packed reactor.[95-96] Furthermore, the phenomenon of filamentary microdischarges was also experimentally observed and reported by Tu et al. in their $BaTiO_3$ filled PBPR and by Kruszelnicki et al. in their parallel plate, glass rod filled setup, with camera images.[48, 74]

8.4 Conclusion

In this chapter the discharge gas was changed to dry air to study the behaviour of a streamer, typical for plasmas created in molecular gases, when it finds a dielectric packing in its path towards the opposite electrode. For these calculations, photoionization equations were added to correctly simulate the streamer propagation. We study dry air and not directly CO_2 because it has a simple chemistry, and the photoionization is well described, using Helmholtz equations.[81, 82]

When the streamer hits the first packing bead, a positive restrike is launched in the opposite direction. When it hits the dielectric layer, a standing filamentary microdischarge is formed, with surface ionization waves broadening the footprint on the dielectric surface on either side. Since the ionization rate is enhanced atop the second packing bead, due to polarization of the dielectric material, plasma can also be formed there, connecting with the surface discharge atop the first bead. The plasma now redistributes the largest potential difference to the bottom of the reactor, i.e. the other side of the packing beads. If the electric field is high enough, like between the grounded electrode and the closest packing bead, plasma can be formed directly. For the bead that is positioned farther from the grounded electrode, an ionization wave is launched from the packing bead away from the surface. When it hits the grounded electrode a positive restrike again occurs towards the bottom of the packing bead, similar to the earlier streamer at the top part of the reactor. This positive streamer again initiates the formation of a surface ionization wave, as soon as it reaches the bottom of the left bead. This surface ionization wave can connect with the surface of the right bead, forming another local filamentary microdischarge. The plasma formation in a PBPR in dry air therefore clearly shows filamentary as well as surface discharge behaviour, which is indeed reported in literature.[48, 74, 95, 96]

Chapter 9

Conclusion and Future Prospects

In this thesis we studied a packed bed DBD reactor. By means of experiments we improved the conversion and energy efficiency of the application we are most interested in, CO_2 splitting. However, to be industrially relevant, the values must be increased much further to compete with classical techniques, such as dry reforming, as well as novel competitors, such as electrolysis. The advantage of a plasma reactor is that it can be switched on and off in a time-frame of seconds, and thus it does not need a start-up period, like for instance classical thermal techniques. It is therefore much more compatible with renewable energy sources, such as wind, water or solar energy, which can generate excessive amounts of energy during peak moments. At these times, the plasma reactor can be switched on to consume the surplus of energy. In this case, the effective energy efficiency is a little less important than the ability to instantly switch on and off. A second advantage of the studied plasma technique is that when the used packing is coated with a catalyst, and the right gas mixture is used, future research can lead to results which push the plasma processes in the reactor towards the formation of desired value added chemicals. However, before possible industrial implementation, much more research is needed.

To aid in this quest for understanding, a computational study was executed, since experimental plasma diagnostics are not straightforward with a packing present in the reactor. Because modelling an entire PBPR in 3D, operating in CO_2, is currently beyond our computational limits, we had to make some approximations in our computational study, to make the model solvable in a reasonable timeframe. This means that we had to start with helium as discharge gas, because of its much simpler chemistry set. Furthermore, helium has the ability to form a homogeneous discharge, which fits the used fluid description. In an empty DBD reactor, the discharge gas we are interested in, namely CO_2, will show filamentary discharge behaviour. However, it was suggested from experiments that when a packing is added, the plasma behaviour significantly changes, showing for instance also surface discharges. To get a first impression of the plasma behaviour, the use of helium was acceptable.

The use of helium alone was not enough to limit the calculation time of a 3D model of the PBPR; therefore, we had to approach the 3D geometry by two complementary axisymmetric 2D representations, i.e., a “contact point” model and a so-called “channels of voids” model. The latter was believed to best describe the actual 3D geometry. Based on this representation we studied the influence of various parameters on the discharge initiation and propagation, namely the applied potential, the gap size, the dielectric constant of the packing and the bead size.

Finally, we changed the discharge gas to a molecular gas, namely dry air. The reason of selecting dry air instead of CO_2 was that the photoionization mechanism is well described in literature for dry air. Because dry air also has the ability to form a filamentary discharge, we focussed on the behaviour of a plasma streamer when it interacts with a packing that is blocking its pathway towards the electrode. To correctly calculate the propagation of a streamer, photoionization had to be included in the model.

It is clear that all of the steps taken above do lead to a better understanding of the plasma behaviour in a PBPR. However, there is still a long way to go towards fully modelling a PBPR with CO_2 as discharge gas, as it is used in experiments. Only by continuing to take small steps we will keep moving the boundary of limitations, increasing our understanding. These steps will in the future cover a switch to CO_2 as discharge gas, the ability to change the bead morphology, such as its surface roughness, or even the addition of a catalytic coating on the bead surface. With our increased understanding, we then continue to help optimize the PBPR to, ultimately, make it suitable for industrial implementation.

Summary

Climate change is happening and is caused by human activity! Throughout Earth's history, the planet has been warming and cooling over and over, but never before the change in temperature occurred so quickly. The rise of the atmospheric CO_2 concentration caused by the burning of fossil fuels, to the highest level in three million years, can be seen as the major contributor. If we wish to mitigate the rise of sea level and minimize the amounts of extreme weather events, it is high time that we start acting. The research performed in this thesis very much fits in this context, because it contributes to increasing our knowledge about packed bed plasma reactors (PBPRs) which are being investigated to be used in environmental applications in general, and for the splitting of greenhouse gas CO_2 in particular.

The aim of this PhD thesis is to get a better understanding of the plasma characteristics in a PBPR, in order to help explain the improved experimental results of CO_2 splitting in a packed reactor versus a non-packed reactor in terms of conversion and energy efficiency.

After the introduction, state-of-the-art and the experimental and modelling description in **chapter 1, 2 and 3,** we present in detail our performed research. First, we carried out experiments with an in-house cylindrical DBD reactor, to get a better understanding of the experimental work involved by studying a PBPR (**chapter 4**). By changing the input power, flow rate and bead size of the ZrO_2 packing, the conversion and energy efficiency of CO_2 splitting were optimised, resulting in a maximum obtainable conversion of 42.0 %, and a maximum energy efficiency of 9.6 %. However, it is the ability of simultaneously increasing both the conversion and energy efficiency by a factor 2 compared to the obtainable values in a non-packed reactor, that make a PBPR a promising tool for CO_2 conversion.

Based on the experimental reactor we built a simplified model to computationally study the plasma behaviour in a PBPR (**chapter 5**). In this process we had to make approximations to keep the calculation time reasonable (i.e. maximum a few weeks for a single calculation). Therefore, two complementary axisymmetric 2D geometries were used to mimic the intrinsic 3D problem. Also, we used helium as discharge gas, because of its simple chemistry set and its ability to form a homogeneous discharge, which fits the used fluid description. The results show that a packing enhances the electric field strength at the contact points of the dielectric material due to polarization of the beads by the applied potential. As a result, these contact points prove to be of direct importance for the initiation of the plasma. At low applied potential, the plasma exists locally, but when the applied potential is increased, it gains the ability to propagate through the channel of voids.

In the following chapters the base "channel of voids" model is adjusted to investigate the influence of gap size and/or dielectric constant (**chapter 6**), and bead size and/or dielectric constant (**chapter 7**). When the gap size is reduced to <1 mm, which we call a microreactor, the electric field is much more enhanced. However, the electron density will be significantly lower, which strongly reduces the electron impact reaction rates. Reducing the bead size has a comparable effect. Furthermore, a small packing also requires a higher breakdown voltage.

Changing the dielectric constant of the packing can significantly change the discharge behaviour. While at low dielectric constant the plasma has the ability to propagate through the void channels, at higher dielectric constant the plasma becomes localised in the voids. The value of dielectric constant at which this happens, is lower for smaller beads and/or a smaller gap. The current profile of the discharges is closely related: when the plasma exist over the full gap, the current profile shows fewer strong current peaks, compared to the current profile of localised plasma, which contains a lot more smaller current peaks.

Finally, in **chapter 8** we changed the discharge gas to dry air, in order to study the behaviour of a streamer, typical for plasmas created in molecular gases, when it finds a dielectric packing on its path towards the opposite electrode. For these calculations, photoionization equations needed to be added to correctly simulate the streamer propagation. We study dry air and not directly CO_2 because it has a relatively simple chemistry and the photoionization is well described, using Helmholtz equations. After the initial streamer, a positive restrike turns the discharge into a standing filamentary microdischarge between two dielectric materials. The surface ionization wave that broadens the footprint of the filament on a dielectric surface can jump to the next packing bead, resulting in another local filamentary microdischarge, at the place of enhanced electric field, namely the contact points. The plasma formation in a PBPR in dry air therefore clearly shows filamentary as well as surface discharge behaviour.

The performed studies do increase our knowledge of the plasma behaviour in a PBPR. However, there is still a long way to go before a PBPR can be fully modelled with CO_2 as discharge gas, as it is used in experiments. Our work paves the road for future research, where a switch to CO_2 as discharge gas, the description of a more detailed bead morphology or even the addition of a catalytic coating on the bead surface, are on the menu. Further increasing our understanding can help to optimize the PBPR to, ultimately, make it suitable for industrial implementation.

Samenvatting

Het klimaat verandert, en menselijke activiteit is de oorzaak! De aarde heeft in het verleden altijd een cyclus van opwarmen en afkoelen doorlopen, maar nooit is de verandering in temperatuur zo snel gegaan. De grootste oorzaak hiervan is de gestegen CO_2 concentratie in de atmosfeer tot het hoogste niveau in drie miljoen jaar tijd. Als we het stijgend zeeniveau en de extreme weersgebeurtenissen de kop in willen drukken, is het de hoogste tijd om in actie te schieten. Dit doctoraatsonderzoek past in dit plaatje doordat het bijdraagt aan het vergroten van de kennis over gepakte bed plasma reactoren (PBPRs) dewelke vandaag de dag actief worden onderzocht voor milieutoepassingen in het algemeen, en de splitsing van broeikasgas CO_2 in het bijzonder.

In dit doctoraatsonderzoek wensen we onze kennis van het plasmagedrag in een PBPR uit te breiden. Met onze vergaarde kennis kunnen we dan de verbeterde experimentele resultaten van een gepakte versus een niet-gepakte reactor voor CO_2 splitsing in termen van conversie en energie-efficiëntie, helpen verklaren.

Na de introductie, state-of-the-art en beschrijving van het model en de experimentele opstelling in **hoofdstuk 1, 2 en 3** wordt het uitgevoerde onderzoek in dit doctoraat besproken. Eerst hebben we experimenten uitgevoerd met de in onze groep beschikbare cylindrische DBD reactor, voornamelijk om voeling te krijgen met de manier van werken bij het vergaren van experimentele resultaten in een PBPR **(hoofdstuk 4)**. Door het opgelegde vermogen, de gasstroomsnelheid en de grootte van de pakking aan te passen, zijn we in staat de conversie te optimaliseren naar een maximum van 42.0%, en een maximale energie-efficiëntie van 9.6%. Het is echter de gezamelijke verbetering van de conversie en energie-efficientie met een factor 2 ten opzichte van de waarden in een lege reactor, wat een PBPR tot een veelbelovende techniek maakt.

Gebaseerd op de experimentele reactor geometrie, hebben we een vereenvoudigd model opgesteld om het plasmagedrag in een PBPR computationeel te bestuderen **(hoofdstuk 5)**. Hierbij moesten we verschillende benaderingen uitvoeren, om de rekentijd te beperken (d.w.z. maximum een paar weken per berekening). Hiertoe werden twee complementaire modellen ontwikkeld, om het intrinsieke 3D probleem te modelleren. Als ontladingsgas wordt helium gebruikt, vanwege zijn eenvoudige chemie en het feit dat dit gas een homogene ontlading kan vormen, wat past bij onze fluid beschrijving. De resultaten tonen ons dat de pakking lokaal het elektrisch veld versterkt aan de contactpunten tussen het diëlektrische materiaal, door polarisatie van deze bolletjes door het aangelegde potentiaalverschil. Hierdoor spelen de contactpunten een belangrijke rol bij de initiatie van het plasma. Bij een laag aangelegd potentiaalverschil blijft het plasma gelokaliseerd, terwijl bij hogere potentiaal het zich gaat verplaatsen door de smalle verbindingskanalen tussen de verschillende open ruimten.

In de volgende hoofdstukken hebben we het basismodel met "verbindingskanalen" aangepast, om de invloed van de afstand tussen de elektroden en/of de diëlektrische constante van de pakking **(hoofdstuk 6)**, en de grootte van de bolletjes en/of hun diëlektrische constante **(hoofdstuk7)** te onderzoeken. In een reactor met een open ruimte tussen de elektroden kleiner dan 1 mm, een zogenaamde microreactor, wordt het elektrisch veld meer versterkt dan wanneer deze afstand groter is. De elektronendichtheid is echter wel vele malen lager, wat een negatieve invloed heeft op de reactiesnelheden van de elektronen. Een kleiner pakking heeft een vergelijkbaar effect. Bovendien leidt dit tot een hogere benodigde spanning om tot ontlading te komen.

Het veranderen van de diëlektrische constante van de pakking heeft een behoorlijke impact op het plasmagedrag. Bij lagere diëlektrische constante kan het plasma zich door de verbindingskanalen bewegen, terwijl bij hogere waarden het plasma gelokaliseerd blijft in de open ruimten. De exacte waarde waarbij deze overgang gebeurt is lager voor kleinere pakkingsbolletjes dan voor grote. Het veranderen van gedrag is ook in de stroomprofielen terug te vinden: wanneer het plasma doorheen de verbindingskanalen gevormd wordt, vertoont het stroomprofiel enkele sterke stroompieken, terwijl het stroomprofiel van gelokaliseerd plasma uit meer maar kleinere pieken bestaat.

In **hoofdstuk 8** werd tenslotte het ontladingsgas veranderd naar droge lucht om het gedrag van één enkel plasmafilament, typisch voor plasmas van moleculaire gassen, te bestuderen, wanneer het op zijn pad richting elektrode een pakking tegenkomt. Hiertoe dienden extra vergelijkingen aan het model toegevoegd te worden die de photo-ionisatie beschrijven. We bestudeerden droge lucht en niet CO_2 omdat voor dit mengsel van N_2 en O_2 het photo-ionisatieproces in droge lucht goed beschreven, namelijk met behulp van Helmholtz vergelijkingen. Bovendien heeft het ook nog een relatief eenvoudige chemie. Na de propagatie van de initiële streamer tot aan de diëlektrische pakking, zorgt de hieropvolgende positieve streamer in de tegenovergestelde richting ervoor dat de ontlading verandert in een staande filamentaire micro-ontlading. Aan het aangrenzende diëlektrische oppervlak verbreden oppervlakte ontladingen de footprint van de streamer. Wanneer deze in de nabijheid komen van het tweede pakkingsbolletje, kunnen ze overspringen, met het vormen van een nieuwe lokale filamentaire micro-ontlading als gevolg. Het gevormde plasma in een PBPR met droge lucht als ontladingsgas toont duidelijk zowel filamentair als oppervlakte ontladingsgedrag.

De studies uitgevoerd in dit werk vergroten onze kennis van het plasmagedrag in een PBPR. Er dient echter nog een lange weg afgelegd te worden vooraleer we in staat zijn een volledige PBPR te modelleren met CO_2 als ontladingsgas, zoals deze gebruikt wordt in experimenten. Ons werk plaveit echter de weg voor toekomstig onderzoek, waarbij een overgang naar CO_2 als ontladingsgas, het inbrengen van een meer complexe pakkingsmorfologie en het toevoegen van een katalytische coating rond de pakking zeker op het menu staan. Onze toenemende kennis laat ons toe om de PBPR verder te optimaliseren, om hem ultiem geschikt te maken voor industriële implementatie.

Bibliography

[1] J. Cook, D. Nuccitelli, S.A. Green, M. Richardson, B. Winkler, R. Painting, R. Way, P. Jacobs and A. Skuce, *Environ. Res. Lett.* **8** (2013) 024024

[2] Core Writing Team, R.K. Pachauri and L.A. Meyer, *Climate Change 2014: Synthesis Report. Contribution of Working Groups I, II and III to the Fifth Assessment Report of the Intergovernmental Panel on Climate Change*, IPCC, Geneva, Switzerland (2014)

[3] S.G. Philander, *Encyclopedia of Global Warming and Climate Change*, Sage Publications, Los Angeles USA (2008)

[4] R. Kunzig, *Climate Milestone: Earth's CO_2 Level Passes 400 ppm,* National Geographic News, (2013)

[5] H. Riebeek, *Global Warming,* NASA (2010)
link: http://earthobservatory.nasa.gov/Features/GlobalWarming/

[6] John F. B. Mitchell, *Reviews of Geophysics*, **27** (1989) 115-139

[7] Climate Science Narratives, *It's Water Vapor , Not the CO_2*, ACS
link:
https://www.acs.org/content/acs/en/climatescience/climatesciencenarratives/its-water-vapor-not-the-co2.html

[8] M. McGee, *Present Global CO_2 level*, Vancouver Island, Canada (2017)
link: www.co2.earth

[9] M. Brander and G. Davis, *Greenhouse Gases, CO_2, CO_2e, and Carbon: What Do All These Terms Mean?*, ecometrica (2012)

[10] Greenhouse Gas Emissions Topic, *Overview of Greenhouse Gases*, EPA
link: https://www.epa.gov/ghgemissions/overview-greenhouse-gases

[11] Climate Change Indicators Topic, *Greenhouse Gases*, EPA

link: https://www.epa.gov/climate-indicators/greenhouse-gases

[12] T.J. Blasing, *Recent Greenhouse Gas Concentrations*, CDIAC (2016)
link: http://cdiac.ornl.gov/pns/current_ghg.html

[13] *UN Climate Change Newsroom*, United Nations Framework Convention on Climate Change
link: http://unfccc.int

[14] ToxTown, *Volatile Organic Compounds*, U.S. National Library of Medicine, Bethesda, U.S.A.

[15] F.I. Khan and A.Kr. Ghoshal, *Journal of Loss Prevention in the Process Industries* **13** (2000) 527–545

[16] D.A. Gurnett and A. Bhattacharjee, *Introduction to Plasma Physics*, Cambridge University Press (2005)

[17] S. Siemens, *Poggendorff's Ann. Phys. Chem.* **102**, (1857) 66

[18] U. Kogelschatz, *Fundamentals And Applications Of Dielectric-Barrier Discharges*, coronalab.net (2000)

[19] U. Kogelschatz, *Plasma Chem. Plasma Process.* **23** (2003) 1

[20] K.G. Donohoe, *PhD Thesis*, California Institute of Technology, Pasadena, U.S.A. (1976)

[21] S. Okazaki, M. Kogoma, M. Uehara and Y. Kimura, *J. Phys. D: Appl. Phys.* **26** (1993) 889-892

[22] F. Massines, A. Rabehi, P. Decomps, R.B. Gadri, P. Ségur and C. Mayoux, *J. Appl. Phys.* **83** (1998) 2950-2957

[23] St. Kolev and A. Bogaerts, *Plasma Sources Sci. Technol.* **24** (2015) 015025

[24] A. Fridman¸*Plasma Chemistry*, Cambridge University Press, UK (2008)

[25] G. Trenchev, St Kolev and A. Bogaerts, *Plasma Sources Sci. Technol.* **25** (2016) 035014

[26] H. Chen, H. Lee, S. Chen, Y. Chao and M. Chang, *Appl. Cat. B Environ.* **85** (2008) 1-9

[27] H. L. Chen, H. M. Lee, S. H. Chen and M. B. Chang, *Ind. Eng. Chem. Res.* **47** (2008) 2122–2130

[28] T. Nozaki, N. Muto, S. Kado and K. Okazaki, *Cat. Today* **89** (2004) 57-65

[29] C.-L. Chang and T.-S. Lin, *Plasma Chem. Plasma Process.* **25** (2005) 227-243

[30] H.-X. Ding, A.-M. Zhu, X.-F. Yang, C.-H. Li and Y. Xu, J. *Phys. D: Appl. Phys* **38** (2005) 4160-4167

[31] K. Takaki, S. Takahashi, S. Mukaigawa, T. Fujiwara, K. Sugawara and T. Sugawara, *IJPEST* **3** (2009) 28-34.

[32] A. Ogata, H. Einaga, H. Kabashima, S. Futamura, S. Kushiyama and H.-H. Kim, *Appl. Cat. B: Environ.* **46** (2003) 87-95

[33] X. Tu, H. J. Gallon, M. V. Twigg, P. A. Gorry and J. C.Whitehead, *J. Phys. D: Appl. Phys.* **44** (2011) 274007

[34] Nozaki T and Okazaki K, *Catal. Today* **211** (2013) 29

[35] Wang Q, Cheng Y and Jin Y, *Catal. Today* **148** (2009) 275

[36] Zhang A-J, Zhu A-M, Guo J, Xu Y and Shi C, *Chem Eng. J.* **156** (2010) 601

[37] Gómez-Ramírez A, Rico V J, Cotrino J, González-Elipe A R and Lambert R M, *ACS Catalysis* **4** (2014) 402

[38] Q. Yu, M. Kong, T. Liu, J. Fei and X. Zheng, *Plasma Chem. Plasma Process.* **32** (2012) 153-163

[39] D. Mei, X. Zhu, Y. He, J. D. Yan and X. Tu, *Plasma Sources Sci. Technol.* **24** (2015) 015011

[40] T. Butterworth, R. Elder and R. Allen, *Chem. Eng. J.* **293** (2016) 55-67

[41] I. Michielsen, Y. Uytdenhouwen, J. Pype, B. Michielsen, V. Meynen and A. Bogaerts, *Chem. Eng. J.*, in press (2017) DOI: 10.1016/j.cej.2017.05.177

[42] X. Duan, Z. Hu, Y. Li and B. Wang, *AIChE J.* **61** (2015) 898

[43] J.S. Chang, K.G. Kostov, K. Urashima, T. Yamamoto, Y. Okayasu, T. Kato, T. Iwaizumi and K. Yoshimura, *IEEE T. Ind. Appl.* **36** (2000) 1251

[44] K. Takaki, J.S. Chang, K.G. Kostov, *IEEE T. Dielect. El. In.* **11** (2004) 481

[45] W.S. Kang, J.M. Park, Y. Kim and S.H. Hong, *IEEE Trans. Plasma Sci.* **31** (2003) 504

[46] H. Russ, M. Neiger and J.E. Lang, *IEEE Trans. Plasma Sci.* **27** (1999) 38

[47] N.Y. Babaeva and M.J. Kushner, *Plasma Sources Sci. Technol.* **18** (2009) 035009

[48] J. Kruszelnicki, K.W. Engeling, J.E. Foster, Z. Xiong and M.J. Kushner, *J. Phys. D: Appl. Phys.* **50** (2017) 025203

[49] Y. Zhang, H. Wang, W. Jiang and A. Bogaerts, *New J. Phys.* **17** (2015) 083056

[50] R. Aerts, W. Somers, A. Bogaerts, *ChemSusChem* **8** (2015) 702-716

[51] N. Pinhão, A. Moura, J. B. Branco and J. Neves, *Int. J. Hydrogen Energy* **41** (2016) 9245–9255

[52] O. Schenk, *Pardiso Solver Project*
link: http://www.pardiso-project.org

[53] COMSOL Multiphysics Software
link: https://www.comsol.com

[54] F.K. Brehmer, *Shining light on transient CO_2 plasma*, Technische Universiteit Eindhoven (2015)

[55] M.A. Lindon, E.E. Scime, *Front. Phys.*, **2** (2014) 00055

[56] Q. Ye, T. Zhang, F. Lu, J. Li, Z. He, F. Lin, *J. Phys. D: Appl. Phys.* 2008, **41**, 025207

[57] L.F. Spencer, A.D. Gallimore, *Plasma Sources Sci. Technol.* **22** (2013) 015019

[58] T. Nunnally, K. Gutsol, A. Rabinovich, A. Fridman, A. Gutsol and A. Kemoun, *J. Phys. D: Appl. Phys.* **44** (2011) 274009

[59] Phelps Database, www.lxcat.net, retrieved on February 8, 2014

[60] G.J.M. Hagelaar and L.C. Pitchford, *Plasma Sources Sci. Technol.* **14** (2005) 722

[61] T. Martens, A. Bogaerts, W.J.M. Brok and J. van Dijk, *Anal. Bioanal. Chem.* **388** (2007) 1583-1594

[62] Q. Wang, D.J. Economou and V.M. Donnelly, *J. Appl. Phys.* **100** (2006) 023301

[63] P.L. Patterson, *Phys. Rev. A* **2** (1970) 1154

[64] B.E. Poling, J.M. Prausnitz and J.P. O'Connell, *The Properties of Gases and Liquids: Fifth Edition*, McGraw-Hill, New York, 11.5 (2001)

[65] M.M. Hafez, K. Oshima and D. Kwak, *Computational Fluid Dynamics Review 2010*, World Scientific Publishing, Singapore, 361 (2010)

[66] D. Petrovic, T. Martens, J. van Dijk, W.J.M. Brok and A. Bogaerts, *J. Phys.: Conf. Ser.*, **133** (2008) 012023

[67] Y.B. Golubovskii, V.A. Maiorov, J. Behnke and J.F. Benhke, *J. Phys. D: Appl. Phys.*, **36** (2003) 39

[68] V. Mikhailenko, *J. Korean Vac. Soc.* **21** (2012) 130-135

[69] F. Massines, N. Gherardi, N. Naudé and P. Ségur, *Plasma Phys. Control. Fusion* **47** (2005) B577

[70] M. Bogaczyk, R. Wild, L. Stollenwerk and H.-E. Wagner, *J. Phys. D: Appl. Phys.* **45** (2012) 465202

[71] F. Pechereau, J. Jánsky and A. Bourdon, *Plasma Sources Sci. Technol.* **21** (2012) 055011

[72] H.H. Kim, A. Ogata and Y.-H. Song, *IEEE Trans. Plasma Sci.* **39** (2011) 2220

[73] H.H. Kim and A. Ogata, Int. J. Plasma *Environ. Sci. Technol.* **6** (2012) 43

[74] X. Tu, H.J. Gallon and J.C. Whitehead, *IEEE Trans. Plasma Sci.* **39** (2011) 2172

[75] B. Wang, W. Yan, W. Ge, X. Duan, *Chem. Eng. J.* **234** (2013) 354-360

[76] A. Ohsawa, R. Morrow and A.B. Murphy, *J. Phys. D: Appl. Phys.* **33** (2000) 1487-1492

[77] L.D. Pietanza, G. Colonna, G. D'Ammando, A. Laricchiuta and M. Capitelli, *Plasma Sources Sci. Technol.* **24** (2015) 042002

[78] L.D. Pietanza, G. Colonna, G. D'Ammando, A. Laricchiuta and M. Capitelli, *Phys. Plasmas* **23** (2016) 013515

[79] L.D. Pietanza, G. Colonna, G. D'Ammando, A. Laricchiuta and M. Capitelli, *Chem. Phys.* **468** (2016) 44-52

[80] A. Bogaerts, W. Wang, A. Berthelot and V. Guerra, *Plasma Sources Sci. Technol.* **25** (2016) 055016

[81] A. Bourdon, V.P. Pasko, N.Y. Liu, S. Célestin, P. Ségur and E. Marode, *Plasma Sources Sci. Technol.* **16** (2007) 656–678

[82] A. Luque, U. Ebert, C. Montijn and W. Hundsdorfer, *Appl.Phys. Lett.* **90** (2007) 081501

[83] G. Steinle, D. Neundorf, W. Hiller and M. Pietralla, *J. Phys. D: Appl. Phys.* **32** (1999) 1350-1356

[84] U. Ebert, W. van Saarloos and C. Caroli, *Physial Review E*, **55** (1997) 1530-1549

[85] L. Papageorghiou, E. Panousis, J.F. Loiseau, N. Spyrou and B. Held, *J. Phys. D: Appl. Phys.* **42** (2009) 105201

[86] N.Y. Babaeva, A.N. Bohj and M.J. Kushner, *Plasma Sources Sci. Technol.* **15** (2006) 591-602

[87] N.Y. Babaeva and M.J. Kushner, *Plasma Sources Sci. Technol.* **20** (2011) 035009

[88] G.V. Naidis, *Plasma Sources Sci. Technol.* **15** (2006) 253-255

[89] M.B. Zheleznyak, A.K. Mnatsakanyan and S.V. Sizykh, *High Temp.* **20** (1982) 357-362

[90] J. Poggie I. Adamovich, N. Bisek and M. Nishihara, *Plasma Sources Sci. Technol.* **22** (2013) 015001

[91] Siglo Database, www.lxcat.net, retrieved on July 19, 2016

[92] P. Rajasekaran, P. Mertmann, N. Bibinov, D. Wandke, W. Viöl and P. Awakowicz, *Plasma Process. Polym.* **7** (2010) 665-675

[93] D. Nelson, M. Benhenni, O. Eichwald and M. Yousfi, *J. Appl. Phys.* **94** (2003) 96-103

[94] N.Y. Babaeva and M.J. Kushner, *Plasma Sources Sci. Technol.* **23** (2014) 065047

[95] E.C. Neyts, K. Ostrikov, M.K. Sunkara and A. Bogaerts, *Chem. Rev.* **115** (2015) 13408-13446

[96] X. Tu, H.J. Gallon and J.C. Whitehead, *J. Phys. D: Appl. Phys.* **44** (2011)

List of Publications

1. **K. Van Laer** and A. Bogaerts 'Improving the Conversion and Energy Efficiency of Carbon Dioxide Splitting in a Zirconia-Packed Dielectric Barrier Discharge Reactor' *Energy Technology* **3** (2015) 1038

2. A. Bogaerts, T. Kozak, **K. Van Laer** and R. Snoeckx 'Plasma-Based Conversion of CO_2: Current Status and Future Challenges' *Faraday Discussions* **183** (2015) 217

3. **K. Van Laer** and A. Bogaerts 'Fluid Modelling of a Packed Bed Dielectric Barrier Discharge Plasma Reactor' *Plasma Sources Science and Technology* **25** (2016) 015002

4. Y.-R. Zhang, **K. Van Laer**, E.C. Neyts and A. Bogaerts 'Can Plasma Be Formed in Catalyst Pores? A Modelling Investigation' *Applied Catalysis B: Environmental* **185** (2016) 56

5. A. Bogaerts, R. Snoeckx, A. Berthelot, S. Heijkers, W. Wang, S. Sun, **K. Van Laer**, M. Ramakers, I. Michielsen, Y. Uytdenhouwen, V. Meynen and P. Cool 'Plasma Based CO_2 Conversion: a Combined Modelling and Experimental Study' *Proceedings of the Hakone Conference*, Brno, Czech Republic (2016)

6. **K. Van Laer** and A. Bogaerts 'Influence of Gap Size and Dielectric Constant of the Packing Material on the Plasma Behaviour in a Packed Bed DBD Reactor: a Fluid Modelling Study' *Plasma Processes and Polymers* (2017) DOI: 10.1002/ppap.201600129

7. **K. Van Laer** and A. Bogaerts 'How Bead Size and Dielectric Constant Affect the Plasma Behaviour in a Packed Bed Plasma Reactor' *Plasma Sources Science and Technology* under review

List of Conference Contributions

1. K. Van Laer and A. Bogaerts 'Modelling of a DBD Plasma Reactor for CO_2 Splitting: Comparison With and Without Dielectric Packing', Poster Presntation, 12th International Conference on Carbon Dioxide Utilization (ICCDU XII), Washington D.C., U.S.A., June 2013

2. K. Van Laer, 'Fluid Modelling in COMSOL', Oral Presentation, 1st RAPID Workshop, Antwerp, Belgium, June 2014

3. K. Van Laer and A. Bogaerts 'Modelling of a Packed Bed Dielectric Barrier Discharge Plasma Reactor', Oral Presentation, 22nd International Symposium on Plasma Chemistry (ISPC 22), Antwerp, Belgium, July 2015

4. K. Van Laer and A. Bogaerts 'Modelling of a Packed Bed Dielectric Barrier Discharge Plasma Reactor', Oral Presentation, 68th Annual Gaseous Electronics Conference (GEC 68), Honolulu, U.S.A., October 2015

5. K. Van Laer and A. Bogaerts 'Influence of the Gap Size and Dielectric Constant of the Packing on the Plasma Discharge in a Packed Bed Dielectric Barrier Discharge Reactor: a Fluid Modelling Study', Oral Presentation, 69th Annual Gaseous Electronics Conference (GEC 69), Bochum, Germany, October 2016